UNIVERSITY OF OKLAHOMA

GRADUATE COLLEGE

POLYDIMETHYLSILOXANE (PDMS)/CARBON NANOFIBER NANOCOMPOSITE WITH PIEZORESISTIVE SENSING FUNCTIONS

A THESIS

SUBMITTED TO THE GRADUATE FACULTY

in partial fulfillment of the requirements for the

Degree of

MASTER OF SCIENCE

By

SHOIEB AHMED CHOWDHURY
Norman, Oklahoma
2017

POLYDIMETHYLSILOXANE (PDMS)/CARBON NANOFIBER NANOCOMPOSITE WITH PIEZORESISTIVE SENSING FUNCTIONS

A THESIS APPROVED FOR THE
SCHOOL OF AEROSPACE AND MECHANICAL ENGINEERING

BY

Dr. Yingtao Liu, Chair

Dr. Mrinal Saha, Co-Chair

Dr. Cengiz Altan

I want to dedicate this thesis to all the scientists who came before me in this world and to their scientific endeavors. It is for their contributions and sacrifices; we have a solid foundation to build upon and can practice science free from the burden of ignorance.

Acknowledgements

At first, I want to express how thankful and honored I am to have the opportunity to learn and work with my advisor, my mentor Dr. Yingtao Liu. For the last two years, I had a wonderful journey and it is due to his support I have been able to develop myself both personally and professionally. Also, I would like to express my gratitude to Dr. Mrinal C. Saha who has always guided me to overcome all the challenges in academic life and provided immense technical support throughout my study. In addition, a special thanks to Dr. Cengiz Altan who was the director of Aerospace and Mechanical Engineering during my time here and all the other professors for their support. Finally, all the staffs here at AME and my lab mates such as Mark Olima, Wenyuan Luo, Jingyu Wang with whom I have shared my two years and who were always helpful and supportive at all circumstances.

Above all, to my respected parents, beloved wife, and the special friends here at Norman, I would like to say thank you all. It is for you it was a really memorable experience.

Table of Contents

List of Tables

List of Figures

Abstract

Flexible material that can be deployed for sensing a wide range of pressure and strain is an active research area due to potential applications in engineering and biomedical devices. Current load sensing materials such as metals, semiconductor, and piezo ceramics have limitations in certain applications, due to their heavy density and small maximum measurable strain. In order to overcome those issues, this thesis delves into an alternative material class based on polydimethyl siloxane (PDMS) and carbon nanofiber (CNF) nanocomposites. Although silica and carbon nanoparticles have been traditionally used to reinforce mechanical properties in PDMS matrix nanocomposites, this study focuses on novel sensing systems with high sensitivity and wide load ranges.

A series of nanocomposites with different CNF and silica concentrations were synthesized and characterized to understand their thermal, electrical, and sensing capabilities. The thermal properties, such as thermal stability and thermal diffusivity, of the developed nanocomposites were studied using thermogravimetirc and laser flash techniques, respectively. The electrical volume conductivity of each type of nanocomposite was measured using the four-probe method to eliminate the effects of contact electrical resistance during measurement. Scanning electron microscopy (SEM) was used at different length scales which showed uniform dispersion. Experimental results showed that both CNFs and silica were able to impact on the overall properties of the synthesized PDMS/CNF nanocomposites.

The pressure sensing functions were achieved by correlating the piezoresistance variations of the materials to the applied load on the sensing area. Due to the conductive network formed by carbon nanofibers (CNFs) and the tunneling effect between neighboring CNFs, the experimental results showed a clear correlation between piezoresistance and the loading conditions. The proposed nanocomposite based sensor materials were experimentally characterized under both quasi-static and cyclic tensile and compressive loading conditions. The optimal nanocomposite formulation was identified by choosing materials with the highest sensing gauge factors under the required load ranges. The ideal material were employed to sense strain as high as 30% and pressures up to 50, 100, and 150 psi, which was a significant improvement compared to current off-the-shelf similar sensors. The sensing capability and sensitivity of the identified nanocomposites were further optimized using advanced optimization algorithms and finite element analysis method. Three different shapes including cylinder, conical, and truncated pyramid shaped sensing units were designed, fabricated, and characterized. Cyclic compression tests verified that the optimized sensor units enhanced the sensing capability by obtaining higher gauge factors. Finally, optimized sensing units were assembly in array forms for the continuous monitoring of pressure in a large area. The prototypes of sensor arrays successfully demonstrated their sensing capability under both static and cyclic pressure conditions in the desired pressure range.

Chapter 1 Introduction

Elastomers with high and reversible deformability have significant industrial applications. However, most elastomers have low initial moduli and durability. Additional reinforcing phase is required to enhance their properties for practical use. Poly dimethylsiloxane (PDMS) is a non-conductive elastomer that has attracted special attention for more than a decade due to its flexibility and ease of fabrication. In general, silica particles are most commonly used materials for property enhancement in elastomers [1]. Traditional reinforcing particles have diameters in the range of microns. Recently, nano-scale materials have been reported to provide much better mechanical properties, such as the maximum strength and modulus, due to size effect[2]. This can be attributed to the fact that as diameter gets smaller, the size, density and probability of defects, such as cracks, reduces significantly and can actually approach the theoretical cohesive strength [2]. Extensive efforts have been carried out to develop nanoparticles reinforced polymer matrix composites due to their superior mechanical properties as well as multifunctional capabilities, including high thermal and electrical conductivity, flame and moisture barrier properties.

In the last decade the development of polymer-based nanocomposites provides another approach to enhance critical material properties and even beneficial functionalities, such as load sensing. By dispersing nanoparticles and ‘smart’ materials in a polymer matrix, high-performance lightweight nanocomposites can be developed and tailored to different applications. Thus, interests in smart polymers and nanocomposites with beneficial sensing functions have increased significantly over the last decades. Various types of carbon-based nanoparticles, such as carbon nanofiber

(CNF) [3], carbon nanotube [4], and graphene [5] have been incorporated within polymer materials. In particular, CNFs have excellent electrical, thermal, and mechanical characteristics, as well as their simple incorporation and dispersion within polymers at low fabrication cost [6, 7]. Therefore, the development of CNF-reinforced nanocomposites has become an interesting research field for both material science and mechanical engineering and can be an excellent alternative for CNTs and graphene to develop large nanocomposites structures.

1.1 Effect of Nanomaterials on Thermal, Electrical, and Mechanical Properties of Composites

Enhanced thermal properties due to inclusion of CNFs in polymers have been reported in literature [8, 9]. The dispersion quality of CNFs in polymer matrix and the purity of CNFs are able to significantly impact the thermal properties of fabricated nanocomposites[8, 9] .Hossain et al. recently reported the effects of dispersion conditions on both thermal and mechanical properties of CNF-reinforced polyester nanocomposites. At low CNF loading of 0.2 wt%, the decomposition temperature increased about 10°C and the glass transition temperature increased about 5°C. Roy et al. compared pristine and amine-modified CNFs on thermal properties of PDMS matrix nanocomposites [10]. Due to the depolymerization of PDMS in presence of amine functionalities, pristine CNF reinforced PDMS nanocomposite showed higher decomposition temperature compared to amine-modified CNF-reinforced nanocomposites. More complicated theories, such as the role of tube-end transport and Kapitza contact resistances, have been reported in literature [11].

Due to the outstanding electrical conductivity of intrinsic CNFs, incorporating limited amount of CNFs to polymers can significantly tailor the electrical conductivity of synthesized nanocomposites. Since, virtually all of the electrical conductivity in CNF/polymer nanocomposites is through the network of CNFs, both good dispersion and high length to diameter ratio contribute to better conductivity in nanocomposites. Two parameters are always discussed to evaluate electrical conductivity: percolation threshold and volume conductivity. Percolation threshold is the lowest CNF concentration to form a conducting network in polymers. Volume conductivity is used to evaluate how sufficient conductivity can be achieved at high fiber fraction. Reducing percolation threshold at low CNF loading and achieving sufficient electrical conductivity at high CNF loading are the two main goals for this type of research. In 2000, Goravev et al. [12] reported their fundamental discovery of the electrical conductivity of CNF-based nanocomposites. Complex time and voltage-dependent changes in the electrical resistivity were reported because the CNF networks readjusted under the influence of electrical current flow. Finegan and Tibbetts [13] reported extensive conductivity measurements for CNF/polypropylene and nylon composites. They found a percolation threshold of 3 vol% and were able to reach the electrical resistivity value as low as 0.15 Ω-cm with about 20 vol% CNF loading. Xu et al. [14] were able to fabricate conducting CNF/vinyl ester nanocomposites, investigating a variety of mixing techniques including high-speed mechanical and shear mixing. Although percolation thresholds of 2–3 wt% were obtained, resistivity values below about 10 Ω-cm were not achieved even at high weight fraction, probably due to imperfect fiber dispersion. In 2012, Roy and Bhowmick reported the preparation and electrical property characterization of CNF reinforced PDMS matrix nanocomposites [15]. Low percolation threshold was attained using amine-functionalized CNF-based nanocomposites. Using the same nanofiber loading, nanocomposites using functionalized CNFs were nearly 10 times more conductive than those using intrinsic CNFs.

Improving the mechanical properties of polymers and composites by uniformly dispersing CNFs in host polymer materials can be achieved. In general, the tensile strength and tensile modulus of CNFs are estimated to be at least two orders of magnitude higher than that of polymers. Therefore, CNFs are promising mechanical reinforcement fillers for polymers. Besides the intrinsic properties of CNFs, the mechanical performance of CNFs reinforced polymers depends on many other factors, such as nanofiber dispersion, orientation, and adhesion between polymers and CNFs. Tensile properties of CNFs based nanocomposites depend on the surface treatment and fabrication process. Only marginal improvements in tensile properties were achieved when as-grown CNFs were dispersed into polymers. It has been reported that most of the CNF/polypropylene nanocomposites showed a linear increase in tensile strength with increasing CNF concentration up to 5 vol%, and little improvement was observed beyond that [3]. Moreover, at high filler loading, the poor dispersion of CNFs deteriorated mechanical properties slightly. For example, Sandler et al. reported a linear increase in tensile modulus and yield stress by increasing CNF concentrations in poly(ether ether ketone) (PEEK) [16]. However, adding 10 wt% CNFs to PEEK reduced the strain at break from 22% to 18%. Similar results were reported by Shui and

Chung [17]. Poly(ether sulfone) (PES) filled with 5 vol% and 7 vol% carbon filaments showed 19% and 31% drop of the strain at break.

1.2 Concept of Load Sensing Based on Smart Materials

Materials that have versatile chemical or physical properties especially the intelligence or responsiveness of materials is always of strong interest to the sensing community. The introduction of smart materials can provide multifunctional properties in structures. Several capabilities, such as sensing, healing, adaptation, actuation, and energy harvesting, can be potentially integrated within polymers and composites [18, 19]. In-situ load monitoring and interactive prediction of failure onset continue to be critical challenges to be overcome to assure the wide-spread use of advanced structures and materials in mission critical systems. Therefore, there is a heightened need to monitor real-time structural load, and detect potential structural damage initiation and propagation in engineering structures [20, 21]. Due to the superior electrical properties, the potential stress and strain sensing functions of CNF based nanocomposites can be useful for real time load and can be employed as load or strain sensors.

Flexible materials capable of converting external stimuli such as pressure, strain, temperature, gas flow etc. into electrical signal are drawing significant interest and research activities in recent years due to promising widespread applications including skin-like wearable electronics, prosthetics, robotic manipulation, and structural health monitoring [22, 23]. In regards to developing pressure sensing techniques, there are a number of methods depending on the physical property that changes under pressure such as piezoresistive[24, 25], capacitive [26, 27], piezoelectric [28], and triboelectric modes. Among these both piezoresistance and capacitance based pressure sensors are being more increasingly popular. With the advancement in semiconductor materials, silicon based tactile or pressure sensors are available commercially in array and contact form. However, this technology has a few major drawbacks including the brittle and rigid nature of semiconductors which does not allow it to withstand large deformation rendering not useful for flexible applications. The same goes to commercially available metal strain gauges which can hardly measure 10% strain with low gauge factor. As a result, the improvement of the existing technology of flexible pressure sensors largely depend on the selection of materials with sensing properties, innovative microstructures and array configurations that can maximize the sensitivity in terms of change in output electrical signal with applied pressure, good reliability and reversibility for a large number of loading unloading cycles, and fast response time. In most of the cases, PDMS fits the bill for improvement on those limitations due to its selective mechanical properties in terms of flexibility, mechanical strength and ability to conform to curve surfaces. In the case of capacitive pressure sensors, two conducting electrodes are separated by insulating layer (dielectric layer) of flexible polymer and depending on amount of applied pressure, the distance between two electrodes (thickness of the dielectric layer) changes which results in changes in the capacitance. Nanofillers with good electrical properties, such as CNF can be incorporated into PDMS and be used as the electrodes. In the case of piezoresistive pressure and strain sensor, piezoresistivity stems from the variation in inter filler distance or variation in contact resistance when external mechanical load is applied. As a result, microstructure design can become a crucial design parameter where the sensitivity can be substantially improved compared to the bulk structure that depends on the bulk material property only. This concept is inspired from the tactile sensing capability of epidermal layers of human skins. Available techniques of improving the microstructure design include cleanroom technology like photolithography, screen printing, and other bottom up methods such as micro molding. Combinations of these techniques can be employed to scale them up for large area deployment and higher range of working pressure. However, all these methods are highly expensive in terms of both time and cost. Hence, alternative simpler fabrication method for such large area application is an impactful area of study.

1.3 Outline of the Research for This Thesis

Bearing all these motivations on mind, PDMS and CNF based nanocomposite for flexible load and strain sensing applications have been selected as the research study for this thesis. In chapter two, novel classes of PDMS/ CNF nanocomposites were fabricated by varying the constituent materials (polymer, silica, CNF) contents in order to tailor desired thermal and electrical properties. The goal of manufacturing a number of different nanocomposites is to investigate and identify the optimum material formulation for the mentioned application. Low cost, in house, solvent-assisted ultrasonication method was used to synthesize the nanocomposites. After preparing different types of materials, it is imperative to characterize them in terms of their material properties which are the focus of chapter three. Thermal properties of the fabricated materials were characterized for thermal stability using thermogravimetric analysis (TGA), dynamical mechanical analysis (DMA), and thermal diffusivity using lased based Hyperflash method respectively. Following that, the morphology of fabricated nanocomposites was investigated using scanning electron microscope (SEM) which revealed important information such as uniform dispersion of CNFs within polymer matrix. Electrical properties such as volume conductivity and resistivity were measured by four probe method to quantify percolation threshold which will provide guidance for minimum CNF concentration required.

In order to select the best material formulation that fits the best the desired properties, all the classes of materials were studied for their sensing functions in chapter four. Nanocomposites with good electrical conductivity were experimentally characterized under both tensile and compressive loading condition to explore the bulk material piezoresistive response. Tensile loading experiments were also performed in-situ under SEM to categorically proof the concept of piezoresistance which is a very unique feature of this study. Parameters such as gauge factor and sensitivity of piezoresistance, electrical conductivity, and ability to withstand mechanical loads were used to identify the best material formula. Once the optimum material was identified, different geometric shapes were considered to improve upon the bulk material sensing response. Three different geometric shapes such as cylinder, conical, and truncated pyramid shape sensing units were characterized to show the improvement in sensitivity. Furthermore, finite element method (FEM) and goal driven optimization technique was used to optimize the physical dimensions of each sensing units that would maximize the sensing functions in the pressure range 50 psi, 100 psi, and 150 psi maximum pressure. The detail of the process is explained in chapter five. Finally, sensing units were connected in array forms in an easy-to–build manner to produce a prototype of such sensor and as a proof of concept of large area deployment which could sense a wide range of externally applied mechanical pressure. In chapter six two sensor array prototypes were discussed about which could perform pressure sensing under both distributed and differential pressure load.

Chapter 2 Materials Formulation and Fabrication Methodology

One of the major complications in working with nancomposite materials is the complexity and economic feasibility of the fabrication process. Establishing a manufacturing procedure that can be performed in laboratory setup, with good reproducibility was the first and one of the primary tasks of this research. Polymers and monomers that constitute PDMS formula are available in liquid form. However, CNFs have to mix with them uniformly to achieve the desired goal of good electrical conductivity. Considering the viscosity of PDMS, additional low viscosity based ultra-sonication route technique was used for fabrication. In this chapter, all the materials formula for the PDMS/nanocomposites, details of manufacturing procedure, and outcome product of the fabrication procedure will be discussed to have more confidence and better insight.

2.1 Chemical Formula of PDMS

PDMS is a polymer that belongs to polymeric group commonly referred as Silicone which is made up of repeating units of Siloxane. The chemical formula for PDMS is $Si(CH_3)_3O[Si(CH_3)_2O]_nSi(CH_3)_3$, where n is the number of repeating units[29]. The value of index ‘n’ has significant influence on the final state of PDMS that can vary from liquid to semi-solid. Commercially available off-the-shelf PDMS usually comes in two parts consisting of monomer and curing agent. However, the broader goal of the research was to develop a flexible material than can withstand and self-sense a wide range of strain and pressure. Thus, it is important to tailor the material formulation that will provide desired mechanical response, electrical properties, and enhance pressure sensing capabilities not offered by off-the-shelf materials. Weight ratio of monomers, copolymer, reinforcing silica, and conductive fillers (carbon nanofiber in this case) were varied to fabricate various neat or nanocomposites of PDMS.

2.2 Materials

Vinyl-terminated polydimethylsiloxane (DMS-V31), methylhydrosiloxane-dimethylsiloxane copolymer (HMS-301), hexamethyldisilazane treated silica filler (SIS6962.0), and high temperature platinum catalyst (SIP6832.2) constitute the PDMS formulation and were purchased from Gelest Inc. DMS-V31 has moderate viscosity about 1000 cSt and molecular weight about 28,000 g/mol and HMS-301 has a low viscosity about 25-30 cSt and molecular weight about 1900-2000 g/mol. SIS6962.0 has average particle size of about 2 nm and specific gravity of about 2.2. Tetrahydrofuran (THF ACS stabilized) was obtained from Macron Fine Chemicals to be used as solvent. PYROGRAPH PR-24XT-LHT carbon nanofibers were used as conductive nanomaterials and were received from Applied Science Inc. The average diameter of CNF is about 100 nm. This specific type CNF was chosen due to high electrical conductivity of the fibers as per manufacturing data sheet[30].Initially a total of twelve different neat or nanocomposites of PDMS was fabricated. Three carbon nanofiber concentrations (3, 5, and 8wt %) were used to obtain desired electrical conductivity. Table 2.1 summarizes the formulations and weight ratio of the constituents that were used for initial study.

Table 2.1: Constituent formulations for different PDMS.

Formulation	Material	Weight %
PDMS 0	CNF	0
	DMS-V31	96.2
	Silica	0
	HMS-301	3.8
PDMS 1	CNF	3
	DMS-V31	93.26
	Silica	0
	HMS-301	3.74
PDMS 2	CNF	5
	DMS-V31	91.33
	Silica	0
	HMS-301	3.67
PDMS 3	CNF	8
	DMS-V31	88.45
	Silica	0
	HMS-301	3.55
PDMS 4	CNF	0
	DMS-V31	87.5
	Silica	8.75
	HMS-301	3.68
PDMS 5	CNF	3
	DMS-V31	85.10
	Silica	8.50
	HMS-301	3.4
PDMS 6	CNF	5
	DMS-V31	83.33
	Silica	8.33
	HMS-301	3.33
PDMS 7	CNF	8
	DMS-V31	80.70
	Silica	8.07
	HMS-301	3.23
PDMS 8	CNF	0
	DMS-V31	80.75
	Silica	16.08
	HMS-301	3.17
PDMS 9	CNF	3
	DMS-V31	78.22
	Silica	15.65
	HMS-301	3.13

PDMS 10	CNF	5
	DMS-V31	76.62
	Silica	15.32
	HMS-301	3.06
PDMS 11	CNF	8
	DMS-V31	74.19
	Silica	14.89
	HMS-301	2.97

2.3 Manufacturing Procedure

Low viscosity solution based ultra-sonication technique was used to disperse conductive carbon nanofibers into PDMS monomers[31, 32]. Pre-calculated amount of CNFs were placed in a glass beaker containing Tetrahydrofuran (THF) solvent and 50g of THF was used for each gram of CNFs. The prepared solution was subsequently dispersed using a high intensity ultrasonic probe (Sonic Vibracell with Ti horn) with low amplitude (20% - 22% of total power (depending on CNF and Silica content) to avoid breakage of CNFs and excessive heat generation during mixing. Sonication was performed using a pulse mode (55 second on and 5 second off) for 4 hours in an ice bath and the temperature of the bath was kept under 4^{o}C. In a separate container, DMSV31 and Silica of different weight ratios (10:0, 10:1, and 10:2) were mixed using a mechanical mixture at 1500 rpm for 15 minutes. Then the DMS-V31 and Silica mixture was added into the CNF dispersed THF solution and sonicated for 2 more hours for further mixing and dispersion. Total sonication energy for CNF dispersion in THF was about 90 kJ while 45 kJ was used to further mixing with the polymer. Upon the uniform mixing of CNFs and PDMS polymer, excess THF was evaporated by keeping the solution in a silica oil bath for 8-10 hours (depending on the silica and CNFs content) at 60^{o}C**.** This specific temperature was chosen due to the fact that the THF has boiling temperature of 66^{o}C. To expedite the solvent removal process, the solution was continuously stirred using a magnetic stirrer at 350 rpm. The residual THF in the mixture was less than 5% by weight. Afterwards, the resultant viscous solution was placed in a vacuum oven at low vacuum regime (0.1 MPa) for 8-10 hours to extract any trapped air and residual THF in the mixture. After this stage, the THF content was found to be less than 0.5% by weight. Following that, the copolymer HMS-301 and the catalyst were manually mixed using a stainless steel spatula for about 10 minutes. The mixture was again degassed using the vacuum oven at room temperature for additional 30 minutes and to remove traces of trapped air/gas and THF.

Two types of molds were used; rectangular window frame mold of dimension 140mm x 125 mm x 1.3 mm for mechanical testing (Figure 2.1:a) and slotted mold of dimension 75mm x 15 mm x 2.5 mm for piezo resistance testing (Figure 2.1:b). Frame mold or slotted mold was placed on top of an aluminum flat mold wrapped with vacuum bagging tape for ease of spreading materials when pressure is applied for curing. The PDMS-CNF mixture was then poured to fill the mold cavity and covered with a second flat mold before placing into a Carver press. Both top and bottom platens of Carver press were preheated to 80^{o}C prior placing the specimen mold set inside the press. For curing, the mold was placed between heated platens of the Carver press and a pressure of 1100 Psi was applied while curing at 80^{o}C for 3 hours.

(a)

(b)

Figure 2.1: Showing molds used for fabrication (a) window frame mold for PDMS film (b) slotted mold for beam sample.

After curing process was completed, the mold in use was removed and sample was extracted for post-curing at 150^{o}C for 2 hours in an oven. Figure 2.2 shows photograph of the Carver press while sample is in curing process inside the press. Spatial variation of thickness was recorded for uniformity of the sample. Figure 2.3 shows typical thickness variation along its length across different width directions. As seen from the Figure, the thickness is fairly uniform and the maximum variation is less than 8% which indicates good repeatability of the manufacturing procedure. In order to illustrate the detailed manufacturing process, the schematic of material fabrication procedure is shown in Figure 2.4.

Figure 2.2: Photograph of the sample fabrication inside preheated carver press.

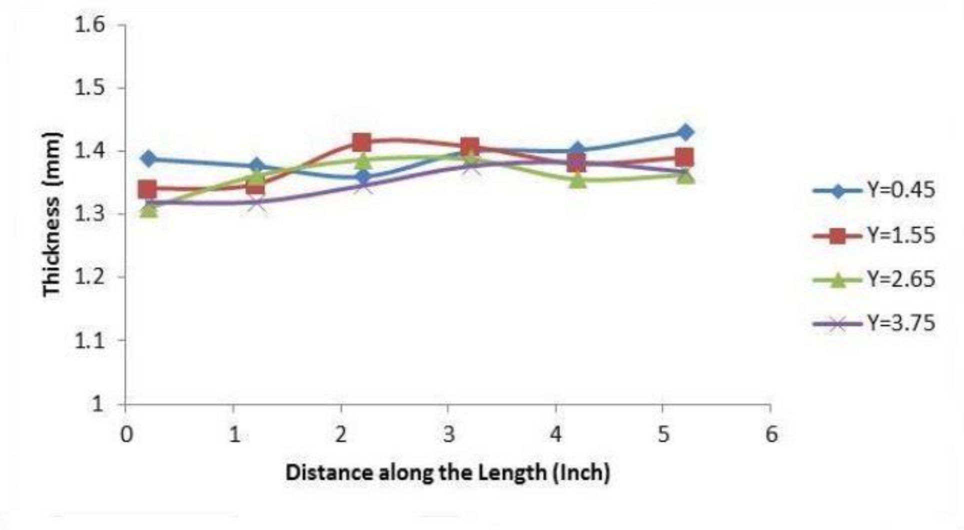

Figure 2.3: Plot showing spatial thickness variation of the film sample (Y indicates distance along width of the sample).

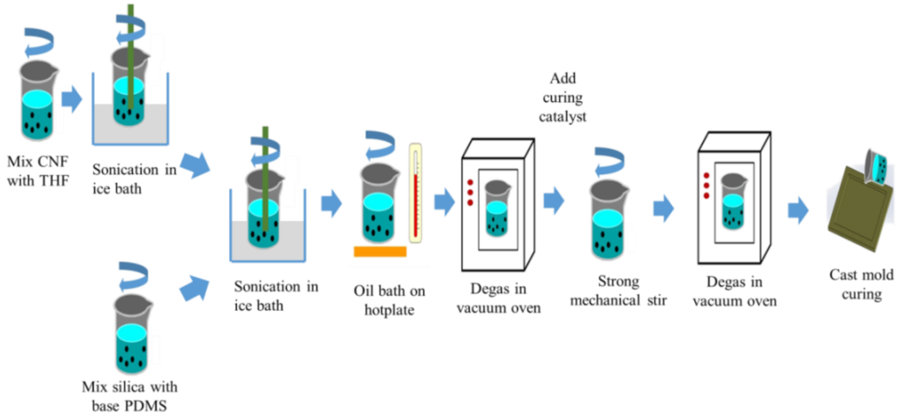

Figure 2.4: Schematic showing fabrication procedure for PDMS/CNF nanocomposite.

As mentioned earlier, both sheet type specimen with small thickness and beam type specimens of nanocomposites were produced throughout the whole study using the same manufacturing procedure.

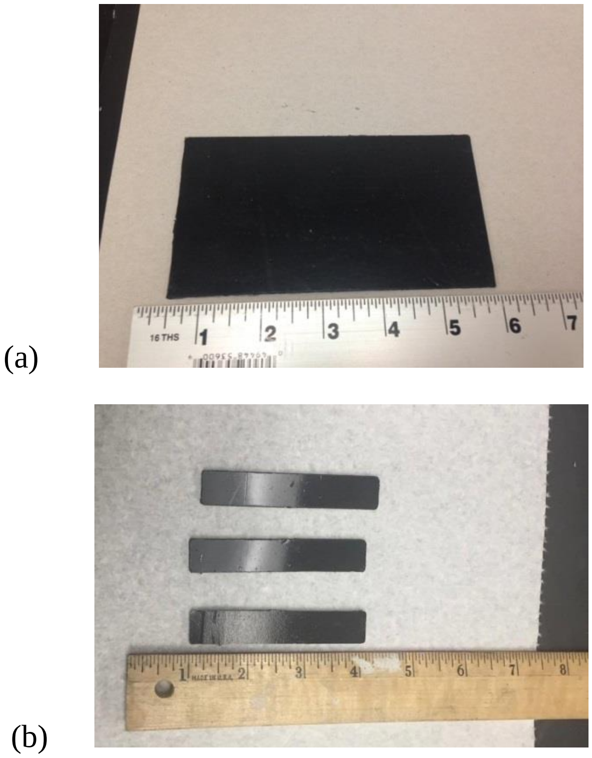

Figure 2.5: Photographs of manufactured sheet and beam type nanocomposites.

As a proof-of-concept of the applicability of the fabrication process, Figure 2.5 shows good quality representative specimens in both sheet and beam structure. Both the surface quality and inside of the nanocomposites were uniform. Thus, the proposed fabrication method can be used for subsequent production with good confidence.

Chapter 3 Material Properties: Thermal, Morphology, and Electrical Conductivity

Objectives of this chapter are to fully characterize and understand the critical material properties of the synthesized nanocomposites discussed earlier using advance material characterization techniques. Materials properties that are the most pertinent to this research are thermal properties, surface morphology for dispersion state of CNFs, and electrical conductivity to understand the electrical properties of the overall nanocomposites. The materials developed for this research had the end goal of obtaining optimized electrical conductivity and pressure sensing capabilities. As many strain and pressure sensing materials are usually exposed to a wide range of temperature, it is vital to characterize the material's thermal properties. For example, thermogravimetric analysis can reveal thermal stability of the material which indicates the usable temperature range without significant mass loss. Furthermore, uniform dispersion of conducting fillers inside nanocomposites is a critical parameter that dictates the electrical properties and thus good dispersion is required for viability of the fabrication method. Microscopic imaging is a qualitative approach that can be used to justify the manufacturing procedure. Finally, electrical conductivity is another material property that can help to select the optimum material formulation. In this chapter, the main focus will be charactering the thermo-mechanical and electrical properties of the manufactured materials that will be useful for subsequent study.

3.1 Thermal Characterization

3.1.1 Thermogravimetric Analysis

Thermogravimetric analysis (TGA) is a thermal analysis that can be conducted to characterize the thermal stability of polymers. In this test, weight loss of specimens are measured as a function of increasing temperature via precisely calibrated mass and thermocouples and can reveal information such as characteristic decomposition, degradation mechanism, chemical changes like second order phase transitions. Thermogravimetric analysis of 12 types of PDMS were carried out in order to analyze the thermal stability using TA instruments Q-50 machine with a ceramic pan under nitrogen purge gas condition. All the specimens were heated from 35°C to 950°C at the ramp rate of 15°C/min. All the obtained data were processed using TA Universal Analysis software. Figure 3.1 shows a photograph of the TGA machine.

Figure 3.1: TA instrument Q-50 model used for TGA tests.

Both weight (%) and derivative of weight loss were plotted as a function of temperature. Figure 3.2 shows the effects of silica concentration and CNF loading on the thermal stability. The degradation of samples without silica took place in only one stage, as shown in Figure 3.2 (a). However, the degradation of all the samples with both silica and CNF loading took place in two stages, as shown in Figures 3.2 (b) and (c). The first decomposition temperature (Td1) was around 500°C and the second decomposition temperature (Td2) was around 690°C. Td1 and Td2, as well as the 5 wt% loss temperature (T5%), are summarized in Table 3.1. There is no report on literature which suggests that parts (bonds) decompose at two different stages yet. However, there exists a relationship between bonding intensity and the decomposition, i.e. a strong bond has a corresponding higher decomposition temperature, while a weak bond has a lower decomposition temperature. Typical bond energies of C–C, C–O, C–H, and Si–Si are 349, 370, 337, and 327 kJ/mol respectively[33, 34].

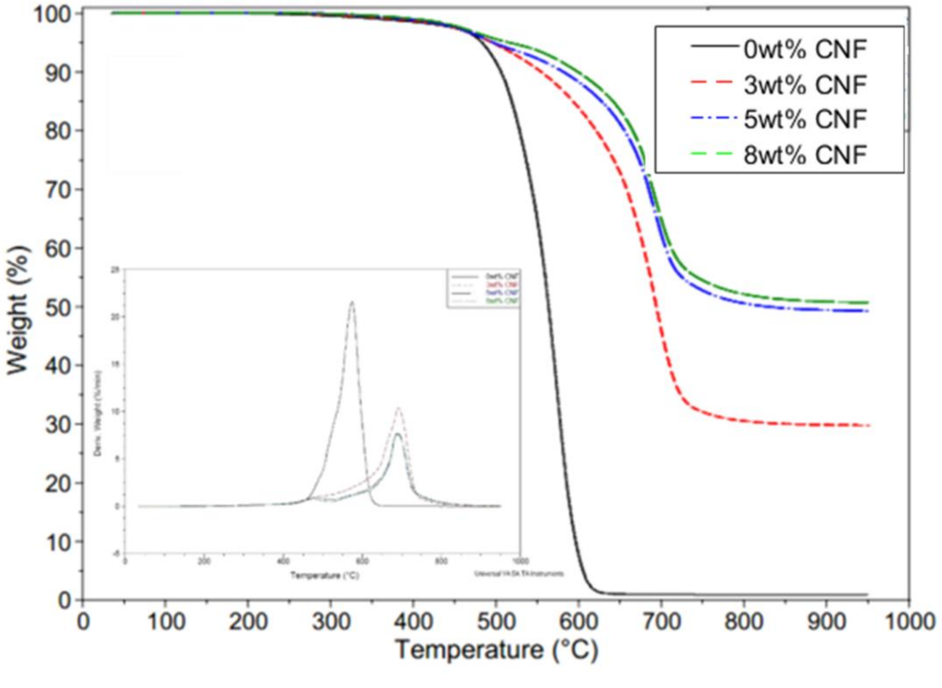

(a)

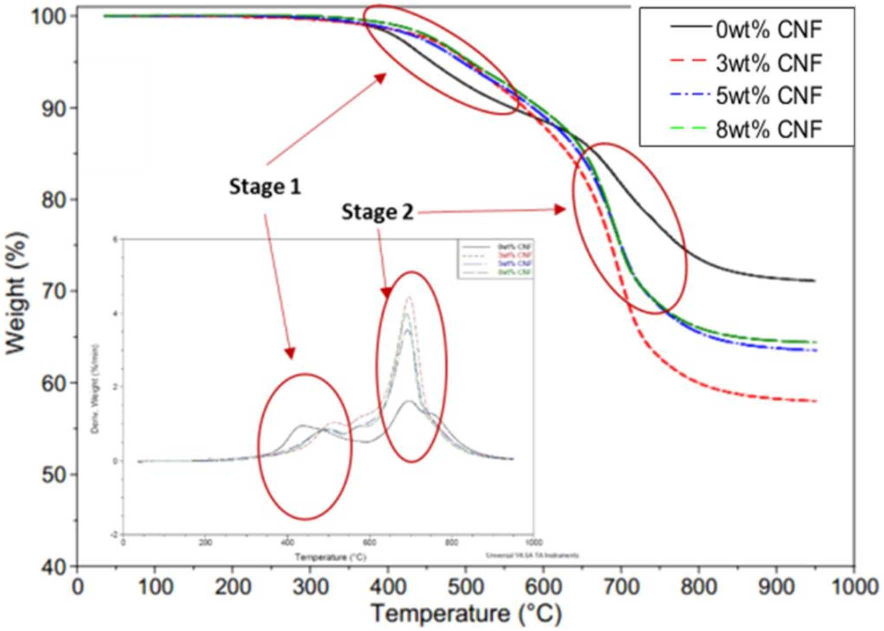
Weight (%)
100
90
80
70
60
50
40
0
100
200
300
400
500
600
700
800
900
1000
Temperature (°C)
0wt% CNF
3wt% CNF
5wt% CNF
8wt% CNF
Stage 1
Stage 2
Deriv. Weight (%/min)
6
4
2
0
-2
0
200
400
600
800
1000
Temperature (°C)
Universal V4.5A TA Instruments

(b)

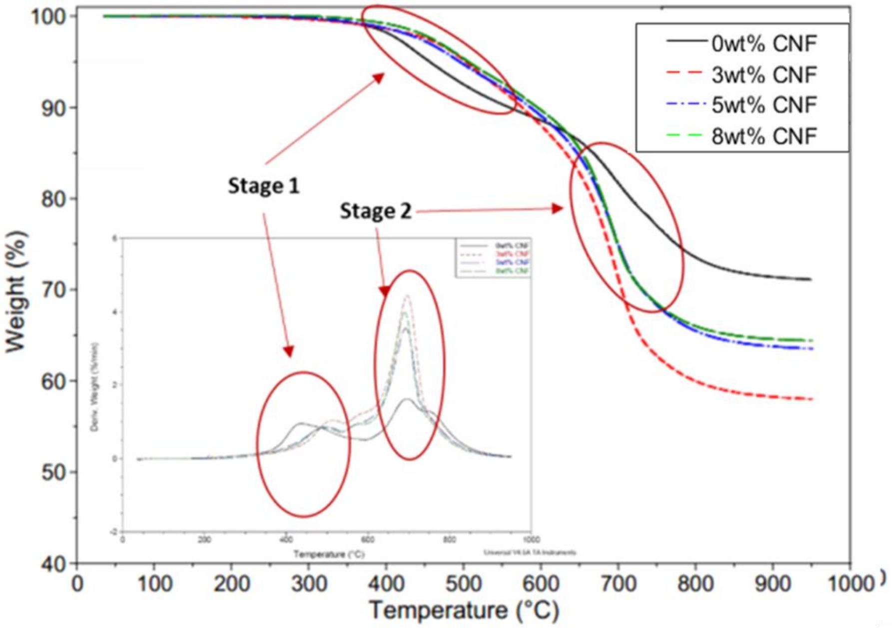
Weight (%)
100
90
80
70
60
50
40
0
100
200
300
400
500
600
700
800
900
1000
Temperature (°C)
0wt% CNF
3wt% CNF
5wt% CNF
8wt% CNF
Stage 1
Stage 2
Deriv. Weight (%/min)
6
4
2
0
-2
0
200
400
600
800
1000
Temperature (°C)
Universal V4.5A TA Instruments

(c)

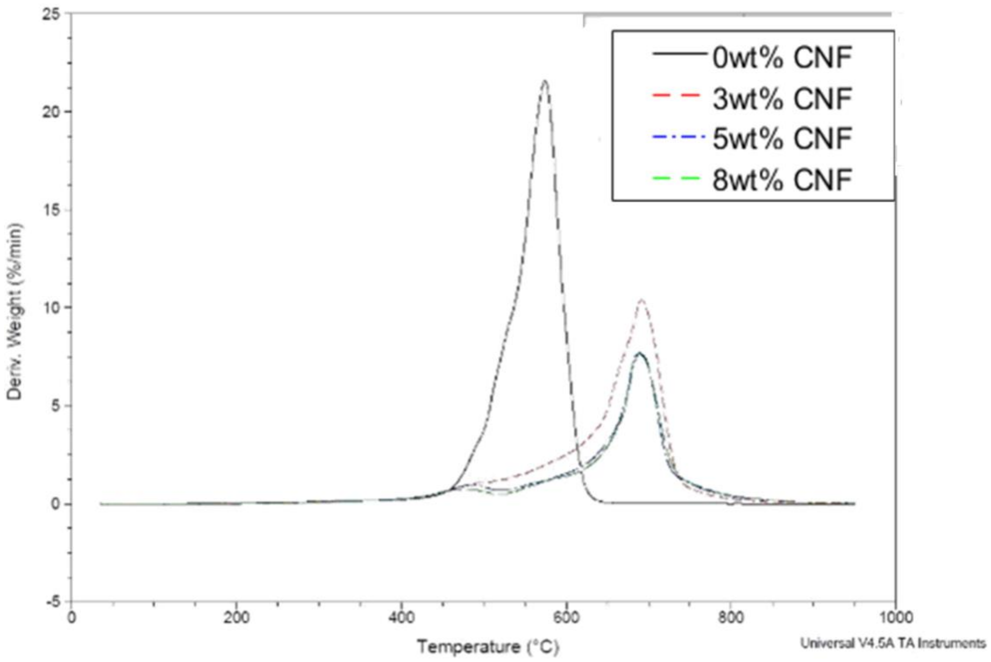

(d)

Figure 3.2: TGA weight loss curves (inset showing differential weight loss) of (a) 10:0 (b) 10:1 (c) 10:2 polymer to silica ratio specimens, and (d) magnified differential weight loss curve.

The single bonds of C–C, C–O, C–H, and Si-Si are susceptible to chain scission during thermal degradation and act as weak links, which correspond to the decomposition of PDMS polymer at Td1. The further decomposition at Td2 can be [33, 34]attributed to the degradation of Si–O bond, where the Si–O bond energy is 798 kJ/mol. The CNF loading also affect the Td1 and Td2 of the nanocomposites reinforced with CNFs. When no silica concentration was included in PDMS formulation, the influence of CNF loading was significant. The variation of Td1 was about 110°C for nanocomposites with no silica concentration. As silica concentration increased, the variation of Td1 was about 60°C and 45°C respectively, for nanocomposites with 10:1 silica concentration and those with 10:2 silica concentrations. The influence of CNF on Td2 was not as large as those to Td1, which is less than 30°C for all the tested samples. It is worth noticing that Td1 increases slightly with the increase of CNF loading. This slight increase of decomposition temperature is attributed to the increased free volume of nanocomposites upon the increased CNF loading, which is consistent with the results of fumed silica particles in glassy amorphous poly(4-methyl-2-pentyne) reported in the literature[35].

Table 3.1: Thermal stability of the CNF/PDMS nanocomposites.

Polymer to silica ratio	**CNF (wt%)**	**Temperature of 5 wt% loss (°C)**	**Td1 (°C)**	**Td2 (°C)**
10:0	0	483	573	N.A
	3	495	691	N.A
	5	497	689	N.A
	8	516	688	N.A
10:1	0	456	435	696
	3	502	509	697
	5	494	491	693
	8	506	494	690
10:2	0	454	477	710
	3	490	504	682
	5	501	511	692
	8	501	522	688

3.1.2 Thermal Diffusivity

Thermal diffusivity of a material indicates the ability of transferring heat from hot side to cold side. The value of thermal diffusivity (α) can be calculated by the formula :

$$\alpha = \frac{k}{\rho C_p} \tag{1}$$

where, k is the thermal conductivity, ρ is the density, and C_p the specific heat capacity at constant pressure. All the thermal diffusivity properties were measured using a LFA HyperFlash laser system.

The schematic of the laser flash system is shown in Figure 3.3 (a). The light beam heats the lower sample surface and an infrared (IR) detector measures the temperature change on the upper surface. Circular samples of the diameter of 12.5 mm and the thickness of around 2 mm were first prepared and then coated with graphite spray. Each sample was measured 12 times to improve the accuracy. All the thermal diffusivity measurements were taken from 22°C to 25°C. The principle of the laser flash method is to irradiate the front side of a specimen using a short energy pulse which is provided by a laser, and record the subsequent temperature rise on the rear side of the specimen using an IR detector [36]. From the shape of the temperature–time curve of the rear side and the specimen thickness, the thermal diffusivity of the specimen can be determined. Due to the transparent nature of the PDMS specimens, they had to be coated prior to testing to ensure absorption and emission at the front and rear faces, respectively. Graphite spray was used in these experiments. Figure 3.3 (b) shows a typical specimen used for laser flash method experiment for thermal diffusivity measurement. It is to be noted that these specimens were cut using a punching machine from the nanocomposite sheets previously prepared.

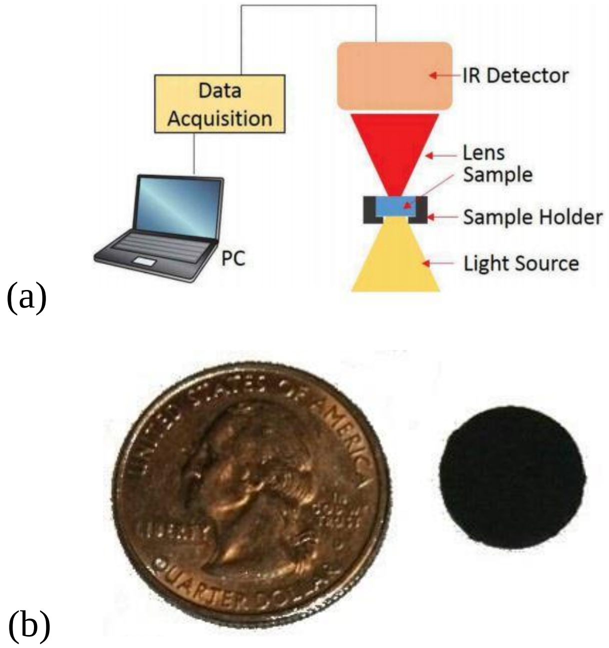

Figure 3.3: (a) Schematic of laser flash based thermal diffusivity measurement (b) specimen for the experiment.

The directly measured properties of thermal diffusivity are presented in Figure 3.4. Scatter bars show the level of repeatability of results, at the 95% confidence level typically used for engineering applications, the values being obtained from 12 repeated tests. Less than 3% of variation was observed from all the measurement which indicated the reliability and repeatability of the experiments. Both CNF and silica loading in PDMS/CNF nanocomposites have impact on the thermal diffusivities. The silica effect on thermal diffusivity can be clearly seen by comparing the samples without any CNF. The thermal diffusivity of such samples increased from 0.12 mm^2/sec to 0.14 mm^2/sec (increased by 17%) when silica loading increased from 10:0 to 10:2 by weight ratio. In addition, the CNF effect on thermal diffusivity can be observed by comparing the samples without any silica loading. The thermal diffusivity of such samples increased from 0.12 mm^2/sec to 0.22 mm^2/sec (increased by 84%) when CNF content increased from 0 wt% to 8 wt%. Since, intrinsic CNF is highly thermally and electrically conductive nanoparticle, it is reasonable to see more significant change of thermal diffusivity when more CNFs were dispersed in nanocomposites. In the future, this result can be used to adjust silica and CNF concentration to obtain desired thermal diffusivity if necessary.

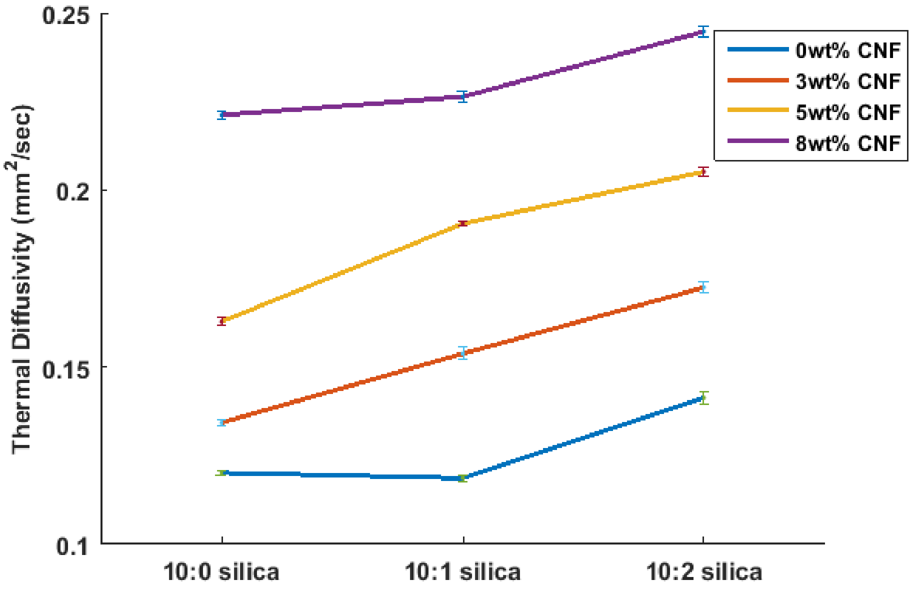

Figure 3.4: Thermal diffusivity of the fabricated neat/nanocomposite PDMS.

3.1.3 Dynamic Mechanical Analysis

Dynamic mechanical analysis (DMA) test were performed on the prepared specimens to characterize the viscoelastic behavior with varied temperature. In this process, mechanical load is applied as a sinusoidal function and resultant sinusoidal strain is measured. However, for polymers, there is a phase lag between applied sinusoidal stress and measured strain due to viscoelastic damping. The ratio of in and out of phase components of modulus (referred to as storage and loss modulus respectively) can give a measure of phase lag in terms of tan δ where δ is the phase lag. The measurement of tan δ with varying temperature can provide valuable information such as glass transition temperature Tg of polymers. Glass transition temperature of a polymer is the temperature when it changes phase between glassy and rubbery state and is usually indicated by sharp rise in tanδ . At Tg, the mechanical properties of polymers degrade largely and that is it is mandatory to operate away from the glass transition temperature[37].DMA experiments of the nanocomposites were performed using TA instrument Q-800 model. Film tension clamp was used due to the softness of the nanocomposites at 0.1% strain with 1Hz frequency of oscillation and 0.01N preload force. The temperature range employed was from 35^{0}C to 150 ^{0} C at a ramp rate of 2^{0}C/min. All the obtained data were analyzed using TA Universal Analysis software.

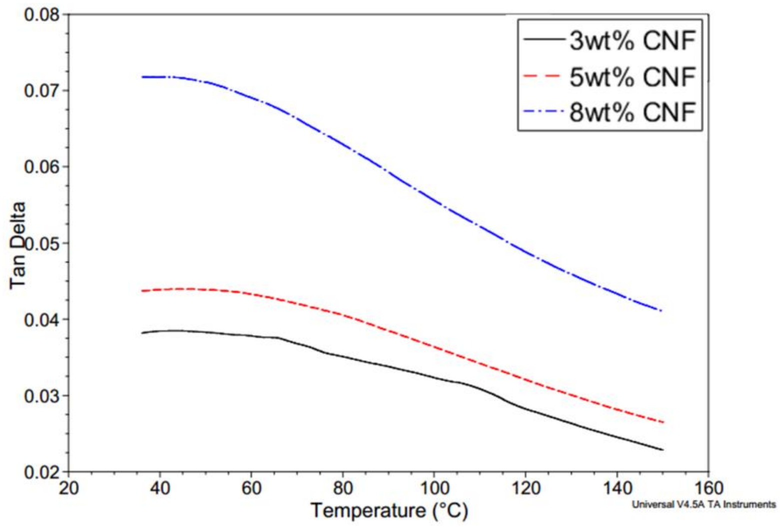

(a)

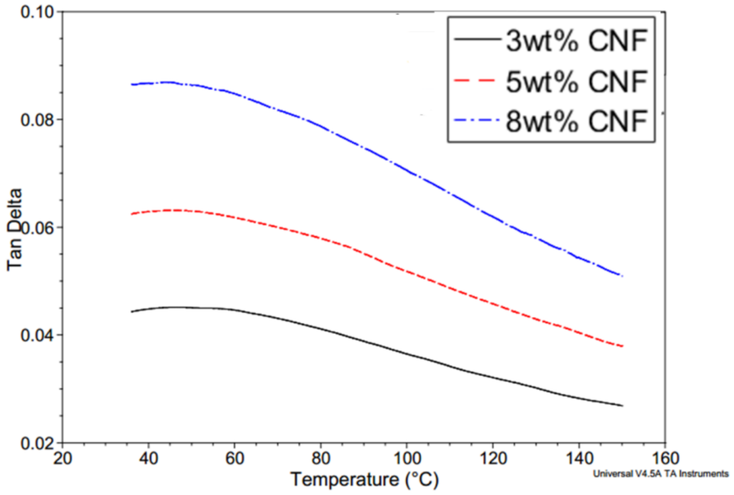

(b)

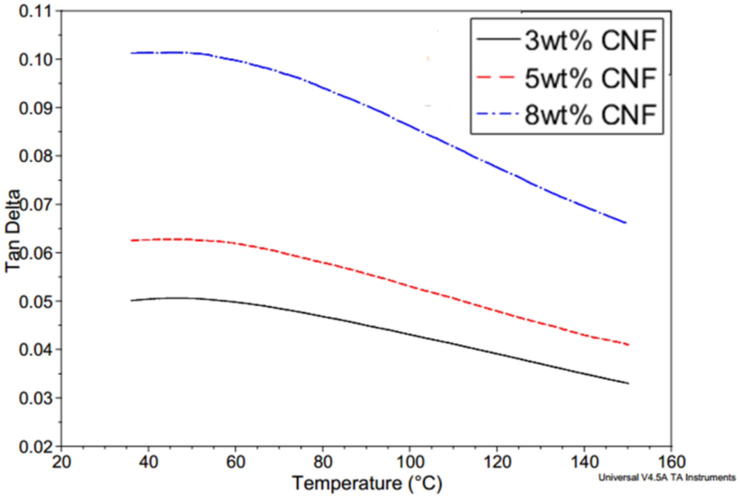

(c)

Figure 3.5: DMA results showing tanδ curves for samples with 10:0 silica (b) 10:1 silica, and (c) 10:2 silica.

DMA experiments were carried out at single frequency tensile strain mode in order to find out whether there is any major drop in storage modulus or peak in tanδ within typical application temperature range. The nanocomposite materials without any CNFs were too soft to test. It can be seen from Figure 3.5 that there is no peak in tanδ curves, Thus, it can be concluded that the glass transition temperature for these materials is not within the tested range and is typically in the negative temperature region[38].

3.2 Morphology Characterization

Nanoparticles that are commercially available come as entangled with each other (carbon nanomaterials) or need to be exfoliated (nanoclays). These phenomenons are attributed to the intrinsic high aspect ratio (> 1000 for CNT or CNF) of nanomaterials which result in extremely high surface area. Besides, there is tube to tube or wall to wall Van-der-Walls attractive force which results in nanoparticles entangled and bundled together in size much higher than their individual characteristic size. In addition, carbon based nanomaterials are chemically inert due to their stable sp2 bonding which result in poor adhesion with polymer matrix and not conducive to uniform dispersion. As a result, external energy is required to overcome the van-der-wall forces and break the agglomeration to achieve homogeneous and uniform dispersion at both micro and nano level[39-41]. Figure 3.6 shows SEM images of pristine CNFs as obtained from supplier signifying the agglomeration and bundled phenomenon.

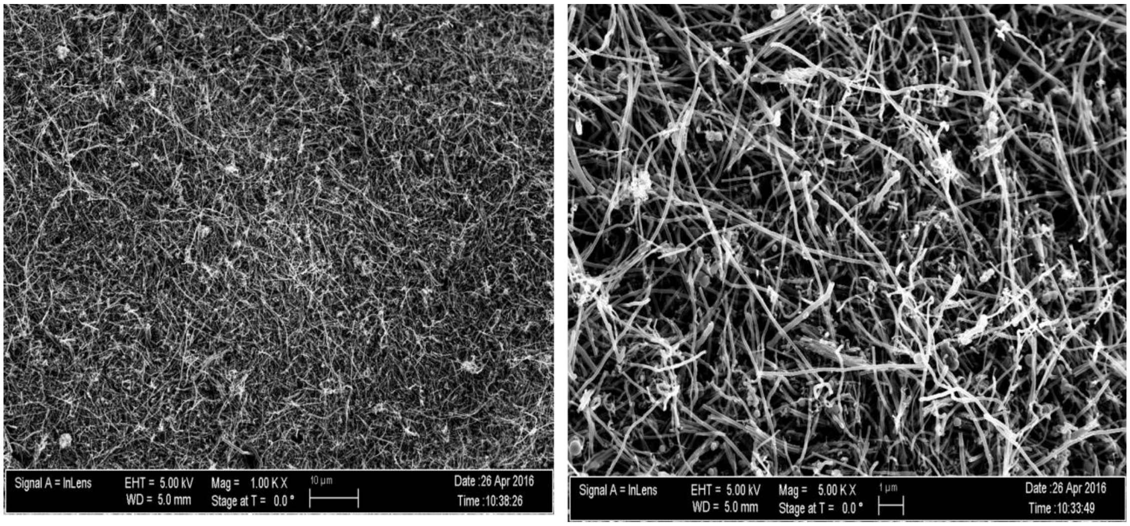

Figure 3.6: SEM micrographs of pristine CNF at different length scales.

If these agglomerated and entangled nanoparticles are not uniformly dispersed within the polymer matrix, the target properties will hardly be achieved and people have reported that mechanical properties like tensile strength can even go down if nanoparticles are poorly dispersed. The bundled nanoparticles act as localized stress concentration region and can act as crack initiator. Besides, there will hardly be any interactions with polymer. In the case of electrical application, such as piezoresistance based pressure sensing, these nanoparticles have to create multiple conductive paths throughout the matrix which is not achievable without uniform dispersion. Song et. al. has compared the overall properties of CNT/epoxy nanocomposite for uniform dispersed and poorly dispersed case. The result is there are orders of magnitude differences in electrical conductivity between poor vs. well dispersion specimens[40]. Due to the size of nanoparticles, light microscopy technique that is used for traditional composites are not suitable. That is why electron microscopy techniques such as scanning electron microscopy (SEM), transmission electron microscopy (TEM) etc. are the most popular imaging techniques to qualitatively characterize dispersion state of nanoparticles inside matrix. Both techniques depend on directing electron beams toward specimen and getting secondary electrons that are characteristic to surface morphology (SEM) or transmitted electron that are representative of through the thickness morphology (TEM). Due to these reasons, SEM images of specimen cross sections have been used to observe the surface morphology and qualitatively characterize the dispersion quality.

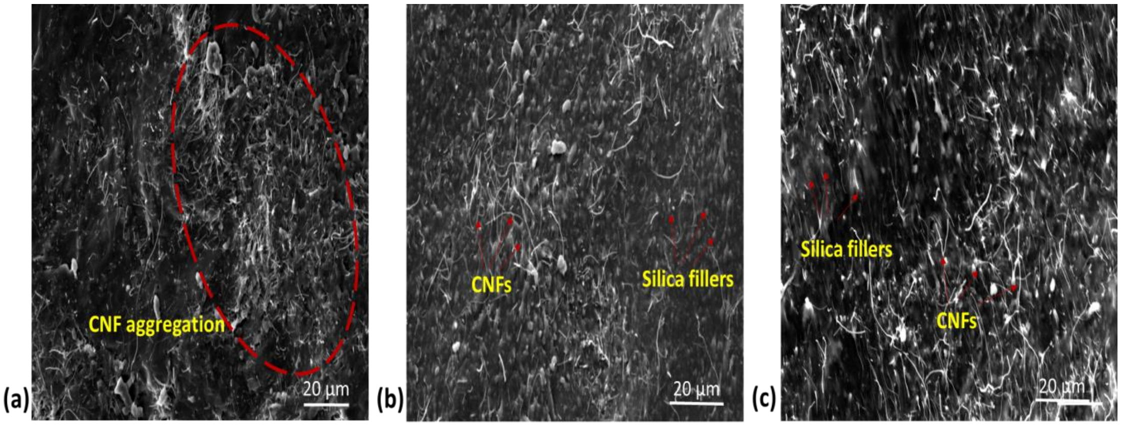

Figure 3.7: SEM micrographs of synthesized nanocomposites: (a) 10:0 polymer to silica weight ratio 3 wt% CNF; (b) 10:1 polymer to silica ratio 3 wt% CNF; (c) 10:2 polymer to silica weight 8 wt% CNF.

SEM images were taken using VEGA TESCAN instrument with 20 KV accelerating voltage at different locations. For better SEM observation, samples were fractured and sputter coated with gold-palladium alloy (~ 2 nm thicknesses). The effects of silica filler to CNF distribution were studied by comparing SEM images taken from samples with different silica concentration and CNF loadings. As shown in Figure 3.7(a), CNF aggregation was clearly observed in the nanocomposite samples of 10:0 polymer to silica ratio and 3 wt% CNF loading. However, the distribution of CNFs in PDMS polymer was significantly improved when silica fillers were introduced in the synthesized nanocomposites. As shown in Figure 3.7(b), in the sample of 10:1 polymer to silica ratio and 3 wt% of CNF loading, the CNFs were much more uniformly distributed in PDMS polymer. Since the CNF loadings in Figures 3.7(a) and 3.7(b) were the same, the improvement of CNF distribution in PDMS polymer was mainly caused by the introduction of silica fillers. Similar results were also observed in other fabricated nanocomposite samples. For example, in the nanocomposite of 10:2 polymer to silica ratio and 8 wt% of CNF loading, both good CNF and silica distributions were observed. The improvement of CNF distribution also led to the improvement of electrical conductivity. To verify the feasibility of fabrication method, SEM micrographs were also taken at different length scale at different locations of the nanocomposite with highest silica and CNF concentrations showing excellent dispersion with little or no agglomerations as well. The idea is that as this specific nanocomposite solution had the highest viscosity during sonication, it would be the hardest to disperse. Thus, if it is able to show good dispersion, the fabrication procedure is justified for the application in hand. Figure 3.8 indeed shows good uniform dispersion at different length scales.

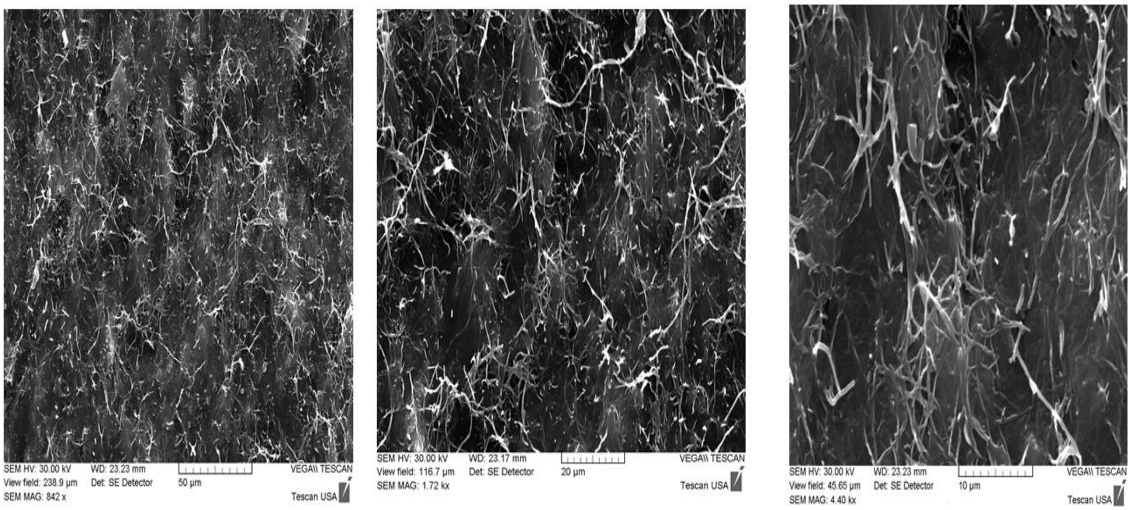

Figure 3.8: SEM micrograph of nanocomposite with 10:2 polymer to silica ratio and 8 wt% CNF.

3.3 Electrical Conductivity

Electrical conductivity is an intrinsic material property that quantifies a material's ability to conduct electrical current. For electrical resistance based application such as piezoresistance based sensing, it is thus imperative to characterize this property and will provide further insight and guidance for choosing the most suitable material formulations. Rectangular samples of CNF/PDMS with dimension approximately 75 mm x 10 mm x 2.5mm were used for electrical conductivity measurements. Initially both the two probe and the four probe based technique were used to compare the results. Figure 3.9 shows both schematic and photograph of four probe electrical conductivity measurement method in real time.

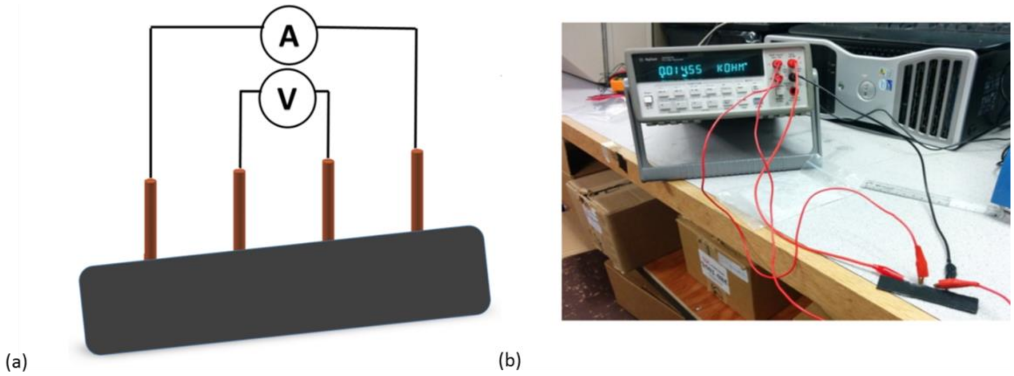

Figure 3.9: Four probe conductivity measurement (a) schematic (b) real time measurement.

In both the two and the four probe methods, copper wires were attached inside the nanocomposites and resistance value was continuously recorded using Agilent multimeter and RS-232 data logger with a sampling frequency of 3 Hz. Each measurement lasted for at least 1 min and the electrical conductivity was averaged from three measurements. In the case of four probe method, electrical current is passed through the two outer wires and electrical voltage measurement between the two center wires give the value of resistance. In all cases, both methods provided stable resistance reading at room temperature. However, the two probe method gives rise to the dominant contact resistance which can be eliminated by employing four probe method. As can be seen from Figure 3.10 that four probe method provides more reliable result by eliminating contact resistance.

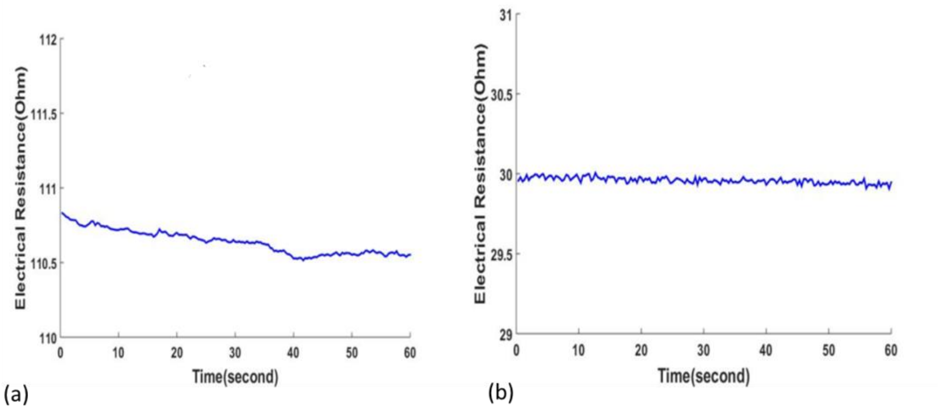

Figure 3.10: Electrical resistance measurement of a typical nanocomposite (a) two probe method (b) 4 probe method.

For nanocomposites with high resistivity Keithley 6105 Resistivity Adapter was used as shown in Figure 15[42] as it is capable to measure very small current in the nano-ampere range thus can operate in the very high resistance region.

Figure 3.11: Electrical conductivity measurements for highly resistive specimens.

The electrical resistivity and conductivity were calculated using Eqs. (2) and (3).

$$\rho = R\frac{A}{L} \qquad (2)$$

where, R is the electrical resistance measured from the rectangular nanocomposite sample using four probe method; L is the length between the two probes in the middle; and A is the cross-sectional area of the rectangular sample. Volume conductivity, σ, is defined as the inverse of resistivity:

$$\sigma = \frac{1}{\rho} \quad (3)$$

Table 3.2: Electrical resistivity and volume conductivity of manufactured nanocomposites.

	10:0 Silica			**10:1 Silica**			**10:2 Silica**		
	3 % CNF	**5% CNF**	**8% CNF**	**3% CNF**	**5% CNF**	**8% CNF**	**3% CNF**	**5% CNF**	**8% CNF**
Resistivity ($\boldsymbol{ohm - m}$)	0.159	0.059	0.032	24.1	0.031	0.012	0.148	0.032	0.012
Volume Conductivity (**siemens/m**)	6.312	17.178	31.733	0.042	32.631	80.919	6.760	31.311	83.138

Table 3.2 shows the electrical resistivity and volume conductivity of the nanocomposite samples. The resistivity of nanocomposite with 10:1 silica concentration and 3 wt% CNF was significantly higher than the other samples. Therefore, it is reasonable to expect the percolation of nanocomposite with 10:1 silica should be slightly lower than 3 wt% CNF. The percolation for other two silica concentration was not observed. As listed in Table 3.2, both silica and CNF concentration can improve the electrical conductivity of the cured nanocomposites. For example, the nanocomposites with 8 wt% CNF and no silica concentration showed about five times higher conductivity compared to the samples with 3 wt% CNFs. The similar trend was also observed in nanocomposite samples with high silica concentrations. Compared to silica, CNF has more significant effects on the electrical conductivity of the developed nanocomposites because of the superior electrical conductivity of constituent CNFs. The observed trend of electrical properties can be useful while designing the formation of new PDMS/CNF nanocomposites.

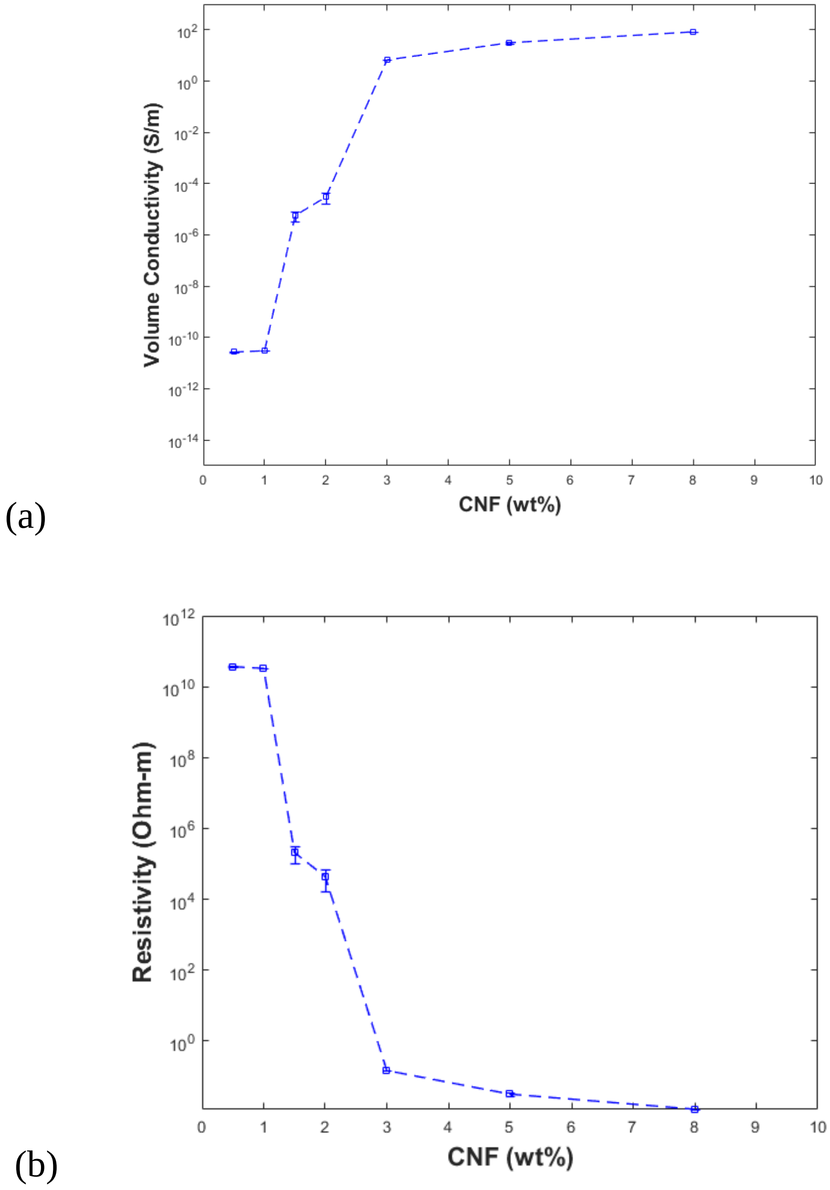

Figure 3.12: (a) Volume conductivity and (b) resistivity of 10:2 polymer nanocomposites resulting percolation threshold at 3 wt%.

For the overall nanocomposite to be electrically conductive there has to be a minimum number of connecting networks created between the carbon nanofibers. This minimum number of connecting networks can only be created when a critical concentration of CNF is reached which is called “percolation threshold”. To quantify the electrical percolation threshold of 10:2 polymer nanocomposites, measurements were taken at lower than 3wt%.CNF concentration. It can be seen from Figure 3.12 that the percolation threshold should be around 3wt% CNF marked by sharp increase in conductivity and decrease in resistivity at that concentration by orders of magnitude and no significant change afterward with increased concentration. This result is consistent with percolation threshold theory[43-45].

In this chapter, some fundamental material properties of the developed novel nanocomposites have been methodologically studied to obtain more insight of the behavior of the materials. Thermal, morphology, and electrical properties that have characterized can be used as guideline to select materials for specific desired properties or even predicting the material behavior with contents not included in this study via method of extrapolation. Thus, this a major step toward the goal of identifying the ideal material formula that will be used as potential pressure sensors.

Chapter 4 Sensing Concept Validation: Tensile and Compressive Loading

Pressure and strain sensors work on the principle of converting externally applied mechanical load to output signals. Depending on which physical properties are being changed under applied load/strain, they can be termed as piezoresistive[46], capacitive [47], piezoelectric [48], triboelectric[49] etc. sensors. The materials developed in this study work on piezoresistive effect. The term piezo refer to the Greek word “piezen” which means “to press” and resistance refers to electrical resistance. So, piezoresistance is change of electrical resistance of material due to externally applied load and thus this change in resistance can be correlated to predict the load being exerted. Electrical resistance of any materials is in general a function of its physical dimensions & resistivity and can be expressed by the following formula:

$$\mathrm{R} = \frac{\rho \mathrm{l}}{\mathrm{a}} \tag{4}$$

where, *l* is the length, *a* is the average cross section area, and ρ is the resistivity of the material. When a small load is applied, the total resistance change is generated by both geometric effect (Poisson’s ratio *v*) and fractional change in resistivity. Total resistance change can be expressed by Equation 5.[50, 51]

$$\frac{\Delta \mathrm{R}}{\mathrm{R}} = (1 + 2v) \in + \frac{\Delta \rho}{\rho} \tag{5}$$

where, ΔR is the change in resistance value from initial resistance, and ∈ is the applied strain on the material. Finally, a term called “Gauge Factor (GF)” is defined to quantify piezoresistive effect relative to strain as follow:

$$\mathrm{GF} = \frac{\frac{\Delta \mathrm{R}}{\mathrm{R}}}{\in} \tag{6}$$

For metallic materials, change in resistance is generated only from geometric effect and change in resistivity is insignificant. Thus, the gauge factor is small and ranges from 1.4 to 2.0 only. However, for semiconductor materials, changes in resistivity improve the gauge factor significantly. With the advancement in semiconductor materials, silicon based sensors are available commercially. However, this technology has a few major drawbacks including the brittle and rigid nature of semiconductors which does not allow it to withstand large deformation rendering not useful for flexible applications[52]. The same goes to commercially available metal strain gauges which can hardly measure 10% strain with low gauge factor[53]. Therefore, a superior alternative has been proposed and explored in this study based on CNF/PDMS nanocomposite materials which possess both the flexibility of PDMS matrix and large change in resistance similar to semiconductors that comes from CNF nanomaterial. The piezoresistive phenomenon in nanocomposite material is graphically shown in Figure 4.1.

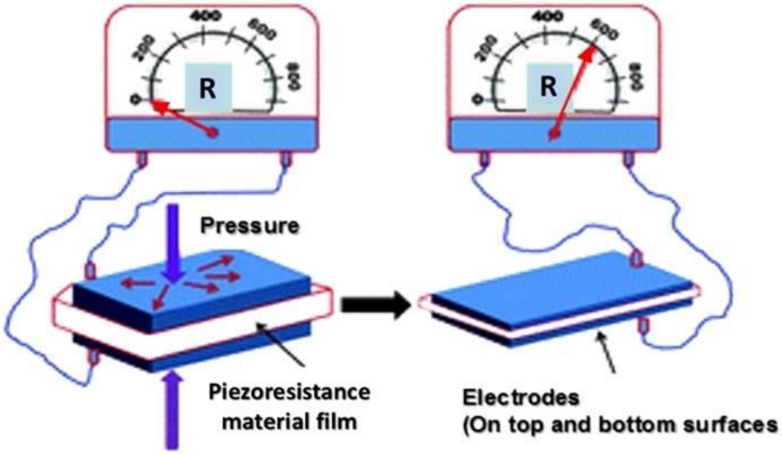

Figure 4.1: Schematic representation of piezoresistance based pressure sensing.

In this chapter, the synthesized nanocomposites will be characterized under both tensile and compressive loading conditions to validate the concept of piezoresistive sensing. This result will provide benchmark for selecting the best material formula. Finally, the sensitivity of the optimum material will be improved in terms of gauge factor by considering different geometric shapes.

4.1 Sensing Response under Tensile Loading

All the CNF filled PDMS nanocomposites as described in previous chapters were experimentally characterized to understand their sensing capabilities. The specimens were characterized under tensile loading conditions at different maximum strain amplitudes. The maximum strains applied to the beam shape nanocomposites in these experiments were 10%, 20%, and 30%, unless the samples failed before reaching the maximum strain. The experiments were performed in a single column INSTRON machine as shown in Figure 4.2. The specimen was always electrically isolated using electrical tapes to avoid any electrical leakage or short circuit connection. The electrical signals were recorded using RS-232 data logging interface with the computer running the data acquisition of the testing machine. The crosshead speed of the testing machine was 2.5mm/min while a sampling frequency of 3 Hz was applied for continuous real time electrical resistance recording. The piezoresistance responses were collected continuously during all the experiments.

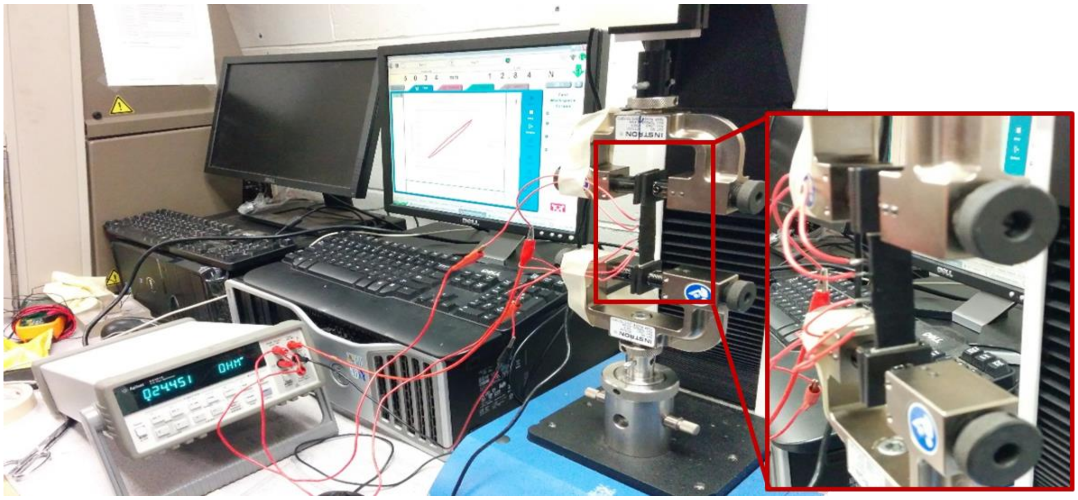

Figure 4.2: Experimental setup of the piezoresistance based sensing tests in tensile loading condition.

The sensing function of nanocomposites in tension with different silica content is shown in Figures 4.3 through 4.5 in terms of percentage resistance change with respect to percentage tensile strain. Nanocomposites without any silica content could only withstand up to 20% maximum strain as they were too soft due to lack of silica fillers which usually provide the mechanical strength. As shown from these Figures, other nanocomposites exhibited excellent flexible properties of PDMS with the ability to stretch as high as 30% where traditional metal strain gauges cannot operate due to high stiffness. The piezo resistance sensing function increased as larger strain was applied and better linearity was obtained using nanocomposites with higher CNF concentration. The gauge factors of each tested nanocomposites are summarized in Table 4.1. Since nanocomposites with 0% silica failed before reaching up to 30% max strain, the gauge factors for this type of materials are only available for up to 20% maximum strain. Significant large resistance change was observed using the nanocomposites with 3 wt% CNF and the base polymer (DMS-V31) to silica weight ratio of 10:1. This may be due to being significantly close or lower than the percolation threshold for this material. However, the resistance value was too high to be used for practical sensing applications and also failed to show repeatable sensing response. That is why focus was given on 5wt% and 8wt% CNF content samples with 10:1 and 10:2 polymer to silica ratio PDMS for subsequent studies as they had good electrical conductivity and mechanical flexibility. Their resultant gauge factors were as high as 3.3, 2.7, and 1.7 at the range of 10%, 20%, and 30% maximum strain respectively. At higher silica concentration (10:2) all nanocomposite samples were found to be appropriate for sensing application based on tension loading. These results can be used as another parameter of selecting optimized material formulation.

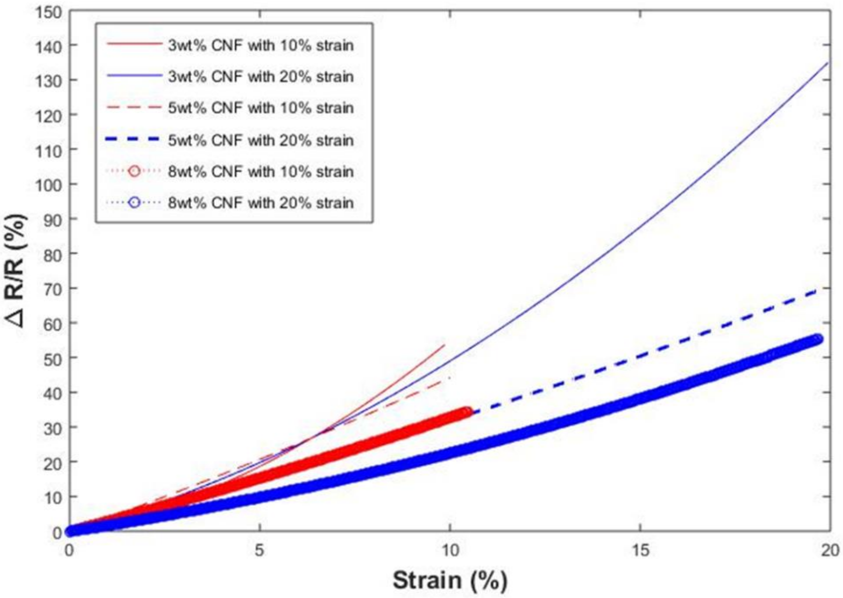

Figure 4.3: Sensing response of nanocomposites containing 0% silica.

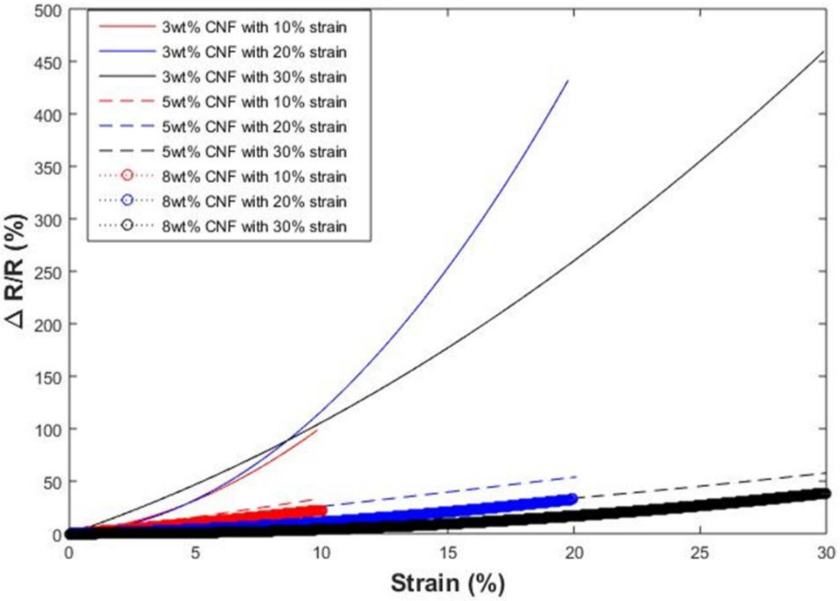

Figure 4.4: Sensing response of nanocomposites containing 10:1 polymer to silica ratio.

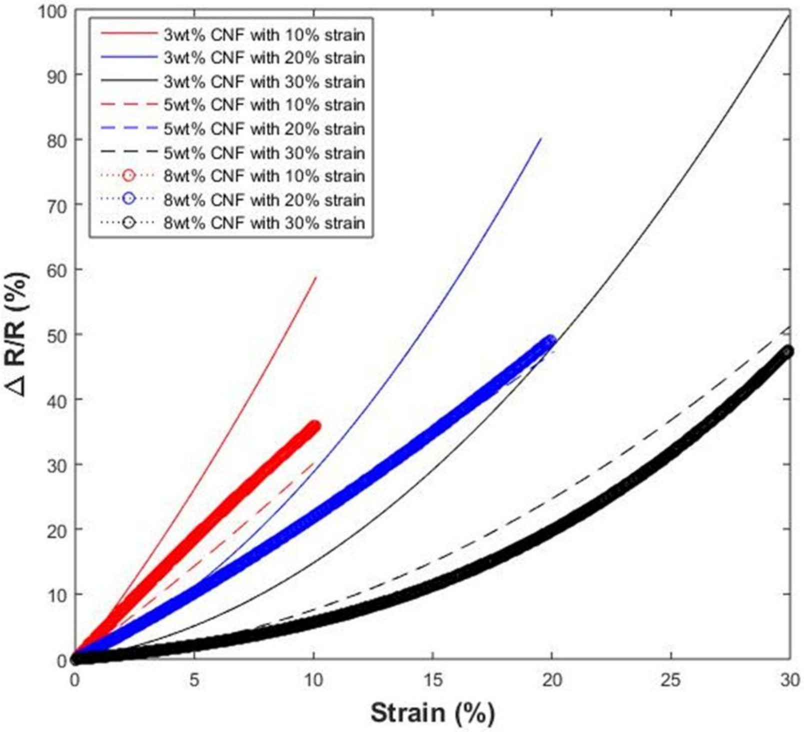

Figure 4.5: Sensing response of nanocomposites containing 10:2 polymer to silica ratio.

Table 4.1: Gauge factor of tested nanocomposites under tensile load conditions.

	10:0 silica			10:1 silica			10:2 silica		
	3% CNF	5% CNF	8% CNF	3% CNF	5% CNF	8% CNF	3% CNF	5% CNF	8% CNF
10% strain	5.44	4.42	3.29	10.04	3.36	2.24	5.81	3.01	3.31
20% strain	6.77	3.71	2.79	21.82	2.69	1.64	4.1	2.35	2.46
30% strain	-	-	-	15.37	1.92	1.29	3.3	1.71	1.59

The effect of strain rate on the sensing function was also investigated. The 10:2 weight ratio silica 8wt% CNF sample was chosen for this purpose due to its better mechanical strength, relatively high conductivity, and superior sensing function in the tensile strain range 30%. Three different loading rates as 2.5, 5, and 10 mm/min were applied and it can be seen from Figure 4.6 that there is some effect of the strain rate on the sensing response. However, this is a common phenomenon due to hysteresis effect for this type nanocomposite and is within acceptable range. Also, PDMS is a viscoelastic material and as a result there can be variations in the subsequent measurements due to viscoelastic damping.

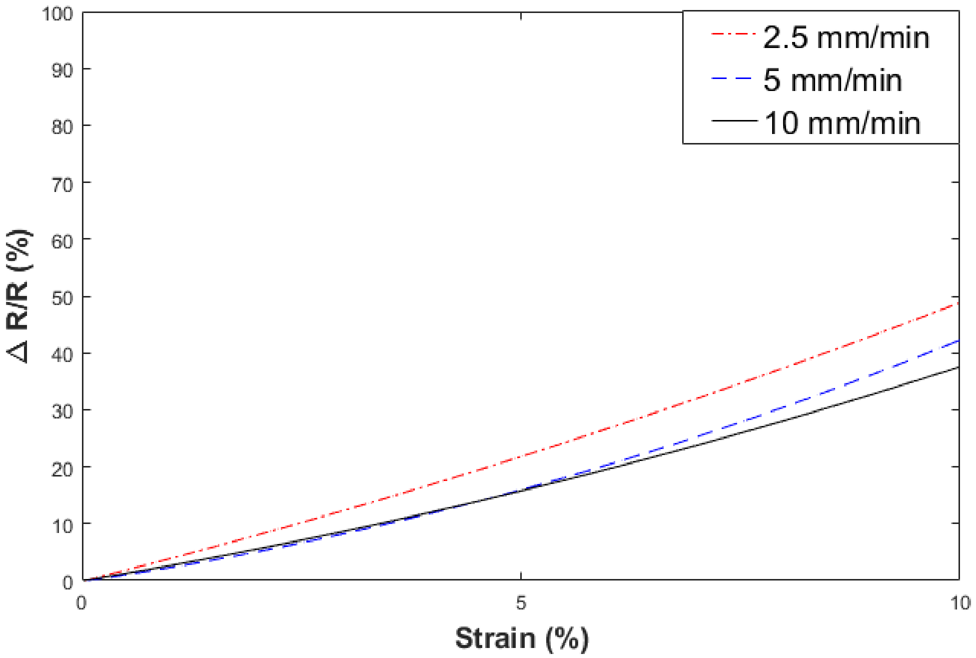

Figure 4.6: Effect of strain rate on the sensing response of the nanocomposite containing 10:2 weight ratio silica and 8wt% CNF.

4.1.1 Experimental Study of Piezoresistance Behavior under SEM

Electrical conductivity of nanocomposites arises from highly conductive nanofillers such as CNT, CNF, and Graphene as polymer matrix is electrically insulative and thus can be neglected. At low concentration of fillers, there are not enough conductive paths that exist for electrical current to flow. As the filler content reaches critical value, (i.e. percolation threshold) sufficient conducting networks are created and thus small tunneling current arises. Under applied load, the inter-filler distance changes by changing the number of conducting paths and smallest distance between fillers. As a result, the amount of tunneling current flow changes which is the basis of piezoresistance effect. Various theoretical models have been developed relating change in resistance to interfiller distance and number of conducting paths to applied strain/load [46, 54, 55]. According to the statistical model developed in literature, conductor particles, in the vicinity of percolation threshold V_C, assemble in clusters.

Upon approaching percolation threshold V_C, the correlation radius ξ (the average distance between two opposite particles of a cluster) diverges as following:

$$\xi \sim |V - V_C|^{-k} \tag{7}$$

where k is the critical index. After percolation threshold, electrical conductivity σ of the composite changes as

$$\sigma \sim |V - V_C|^{-k} \tag{8}$$

where, k is the critical index. Under mechanical deformation of composites, ξ and, consequently, σ change. This is the reason behind the existence of piezoresistive effect. If load is applied to a composite sample, the resistance will be altered due to the change of particle separation (least distance between conducting particles). Assuming that under applied load the particle separation changes from s_0 to s, the relative resistance (R/R_0) is given by the following formula where particle separation s changes depending on applied strain.

$$\frac{R}{R_0} = \frac{s}{s_0}\, e^{[\gamma(s-s_0)]} \tag{9}$$

However, this is the first time to knowledge this phenomenon has been experimentally shown where definite change in interactions between nanofibers have been observed when tensile load was applied under SEM. Therefore, this study categorically proofs the concept of piezoresistance in a manner that was never done before.

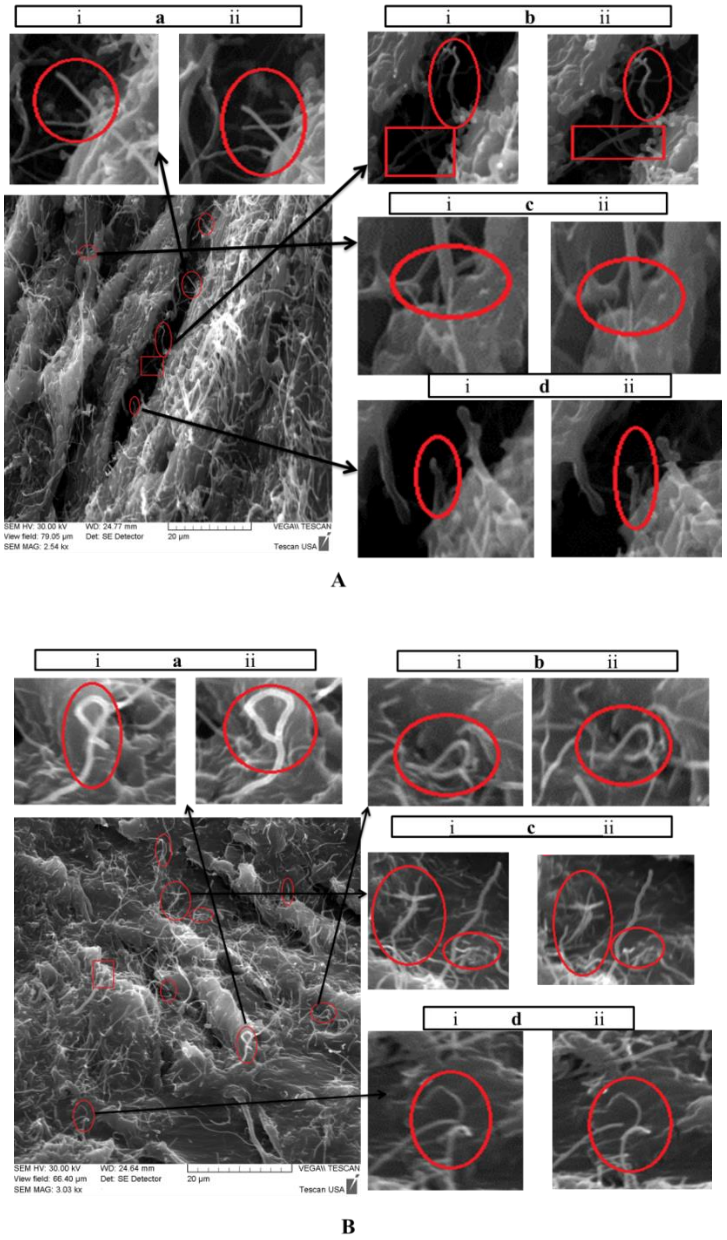

Figure 4.7: Tension test under SEM showing piezoresistance phenomenon (a-b): rotation of nanofibers (c-d): change in interfiber distance where i) no load and ii) after tensile load applied (A and B represents 20% and 40% average strain respectively).

Nanocomposite samples were uniaxially pulled under SEM using a DEBEN microtester (200N load cell) at 1mm/min displacement rate and micrographs were taken at different displacements. SEM images were taken at the same locations of specimens both initially and after being pulled in tension. Figure 4.7 shows the comparison between two states at 20% and 40% strain levels respectively at two different locations. Clear interactions between nanofibers were observed where both rotation of nanofibers and change in interfiber distance were visible. The rotation phenomenon (Figure 4.7: a-b) is due to alignment of nanofibers under load which explains the noise during transition between loading and unloading[56] as shown in Figure 4.10 in next section. As the nanocomposites were pulled in tension, it resulted in increased nanofiber distance (Figure 4.7:c-d). Initially more nanofibers were connected with each other. After the application of tensile load, the interfiber distance increased and thus decreasing the number of connected nanofibers which causes amount of tunneling current flow. This result explains the change in resistance under load due to change in tunneling current and provide experimental validation for the theoretical models.

4.2 Sensing Response under Compressive Loading

Characterization of the sensing capabilities of the CNF filled Gelest PDMS nanocomposites under compression load is one of the key objectives in this study and appropriate for pressure sensing applications. Pressure ranges for the flexible nanocomposites were selected as 50,100, and 150 Psi which is much higher than similar tactile sensors reported by others. Initially, regular cubic shapes, with the physical dimension of 10×10×10 mm were used. In order to reduce contact resistance during compression tests, the top and bottom surfaces of each sample was modified using plasma coating, and a thin layer of gold/palladium, as shown in Figure 4.8, to reduce any contact resistance during sensing experiments.

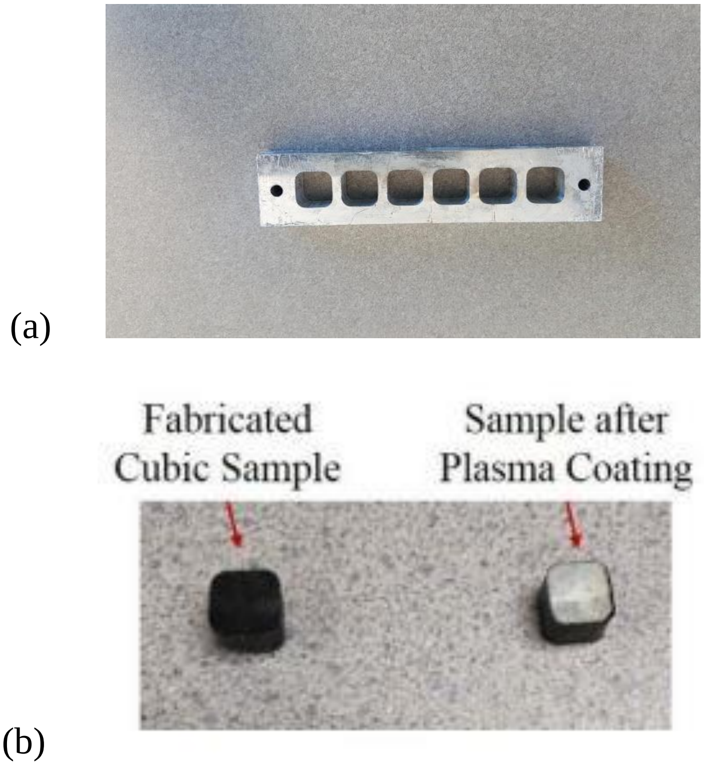

Figure 4.8: (a) Mold used for cubic samples (b) cubic CNF/PDMS before and after plasma coating.

The cubic nanocomposites were characterized under compression cyclic load-unload conditions at different pressure amplitudes using INSTRON single column machine. Three criteria were considered during the characterization of sensing capability: 1) the maximum strain of the candidate nanocomposite under the given pressure range cannot exceed 30%; 2) the sensing feature need to be repeatable under cyclic loading unloading conditions; 3) the change of electrical resistance should be smooth during the load and unload procedure. The material formulation recommended for the pressure ranges were selected following the three criteria. The maximum pressures applied in these experiments were 50 psi (0.345 MPa), 100 psi (0.634 MPa), and 150 psi (1.035 MPa).For all the experiments the load rate was kept at 1 mm/min. The schematic of compression experiments is shown in Figure 4.9.

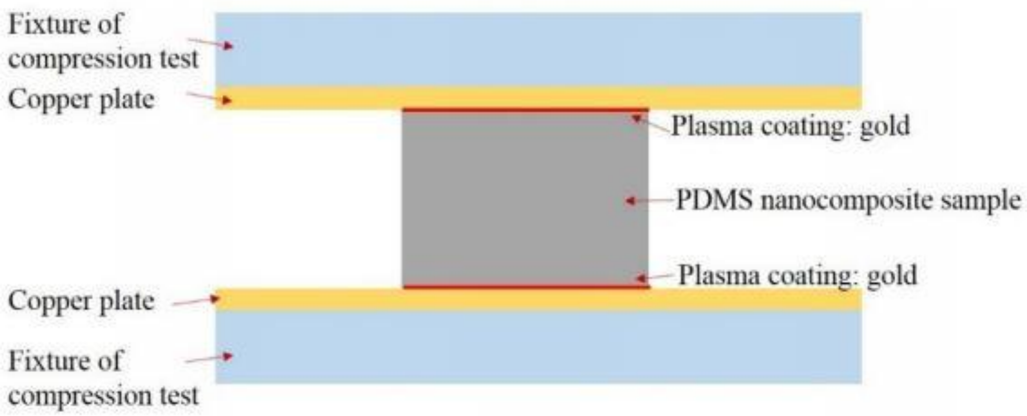

Figure 4.9: Schematic of cyclic compression tests during sensing experiment.

The preliminary experiments in tension demonstrated that the samples of 10:0 silica containing CNF were extremely soft and were not considered as candidates henceforth. Samples of 10:1 silica 3% CNF, 10:1 silica 5% CNF, and 10:2 silica 3% CNF did not perform repeatable sensing capabilities due to the low electrical conductivity of such materials. Samples of 10:1 silica 8% CNF, 10:2 silica 5% CNF, and 10:2 silica 8% CNF showed good sensing repeatability under the given pressure range, as shown in Figures 4.10 through 4.12. The gauge factors of the three types of CNF filled PDMS nanocomposites (10:1 silica 8wt % CNF, 10:2 silica 5wt% CNF, and 10:2 silica 8wt% CNF) are listed in Table 4.2. It is noted that the samples using 10:2 silica and 8% CNF have the largest gauge factor, which show that this material is most sensitive to all the three pressure ranges considered in this research. Therefore, this material formula is the best candidate selected. It can be seen from Figures 4.10 through 4.12 that there is noise in the sensing response during transitions from loading to unloading condition. This is typical phenomenon for this type of material[57, 58]. Also, PDMS is notoriously noted for its inherent hysteresis. Although there were changes in resistance values between subsequent cycles, the percentage change of resistance remained almost same which is another indication for the applicability of this material for pressure sensing.

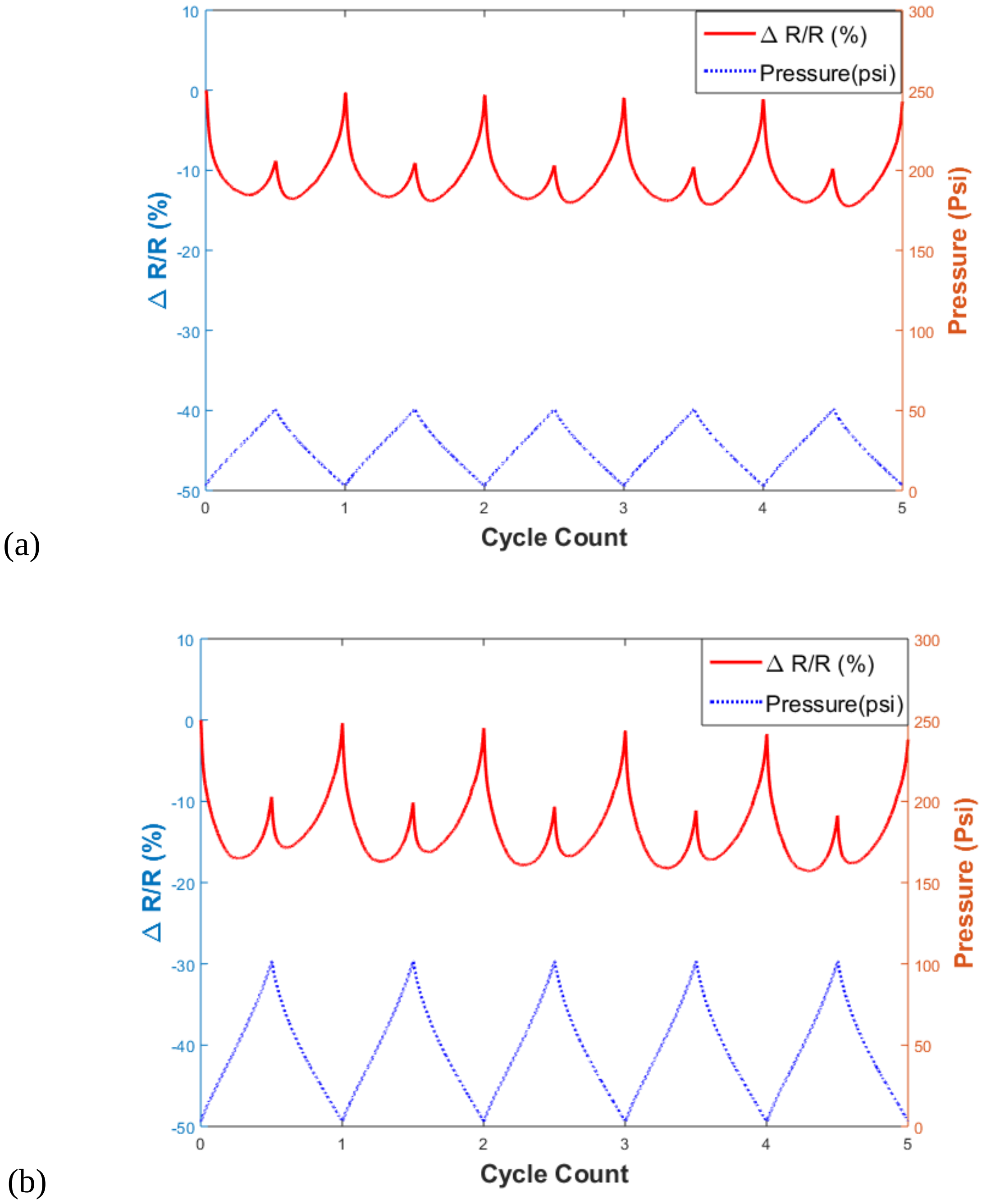

Figure 4.10: Piezoresistance based sensing for cubic samples of 10:2 Silica and 5wt% CNFs; (a) maximum pressure 50 psi, (b) maximum pressure 100 psi.

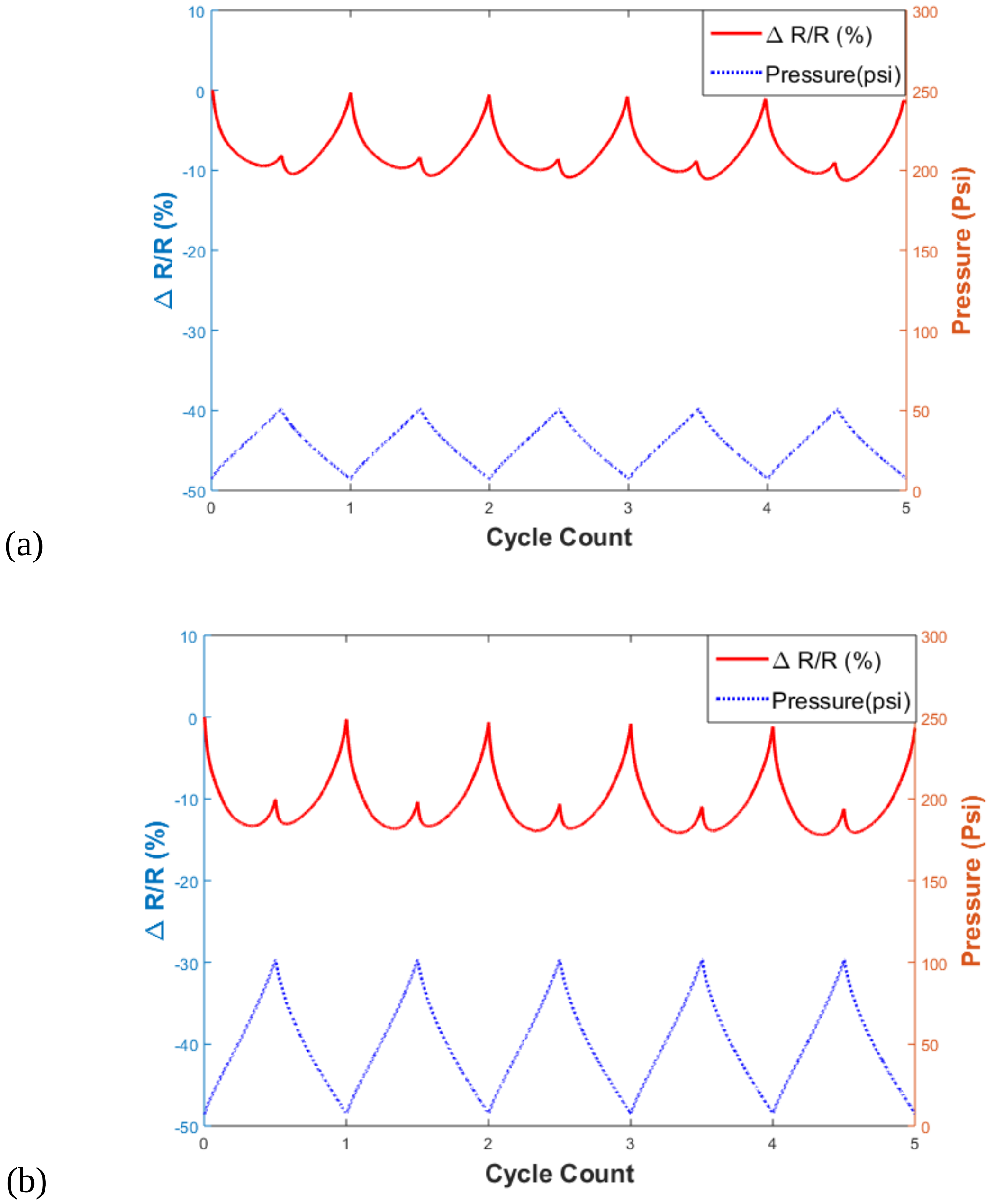

Figure 4.11: Piezoresistance based sensing for cubic samples of 10:1 Silica and 8 wt% CNFs; (a) maximum pressure 50 psi, (b) maximum pressure 100 psi.

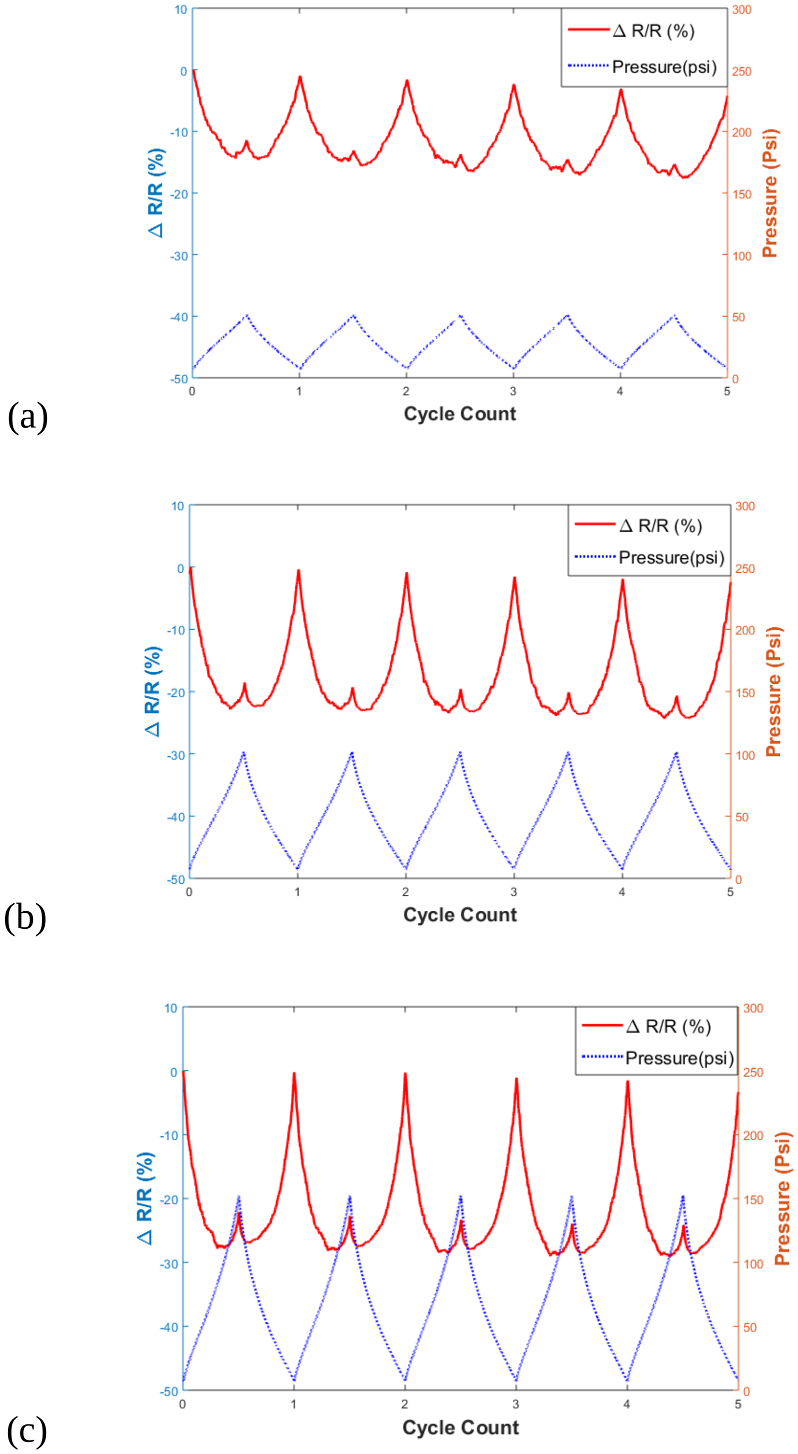

Figure 4.12: Piezoresistance based sensing for cubic samples of 10:2 Silica and 8% CNFs; (a) maximum pressure 50 psi, (b) maximum pressure 100 psi, (c) maximum pressure 150 psi.

Table 4.2: Gauge factor of tested nanocomposites under compressive load conditions.

	10:1 silica		**10:2 silica**	
	5% CNF	**8% CNF**	**5% CNF**	**8% CNF**
5-50 psi	**-**	1.18	1.0	2.14
5-100 psi	**-**	0.77	0.8	1.46
5-150 psi	**-**	-	-	1.33

It is clear that Figures above shows good repeatable sensing response for 3 types of nanocomposites under cyclic compressive loading-unloading experiments. Also, proposed sensing units could operate in the pressure range as high as 150 Psi. This is order of magnitude larger than the similar works reported where workable range was only low pressure regime[59].

4.2.1 Improving Sensitivity by Changing Geometric Shapes

Once the ideal nanocomposite material has been identified, the next step is to improve the sensing function of that particular 8wt% CNF 10:2 polymer to silica ratio material under compression load. Initial sensing function obtained from each sensing unit of cubic shape can be improved using different geometric shapes[60]. Cylindrical and conical shapes were chosen for the improvement in sensitivity as they have planar symmetry and more uniform strain throughout compared to cubic shape. In order to verify the concept, both cylindrical and conical shape nanocomposites (8wt% CNF 10:2 polymer to silica ratio) were produced. The dimension of the cylinder shape nanocomposites were 5mm x 10mm in radius and height whereas cone shape specimens were 5mm x 2.5 mm x 10 mm in bottom surface radius, top surface radius, and height. Figure 4.13 shows the molds that have been used and typical representative fabricated cylinder and cone shape nanocomposite specimens.

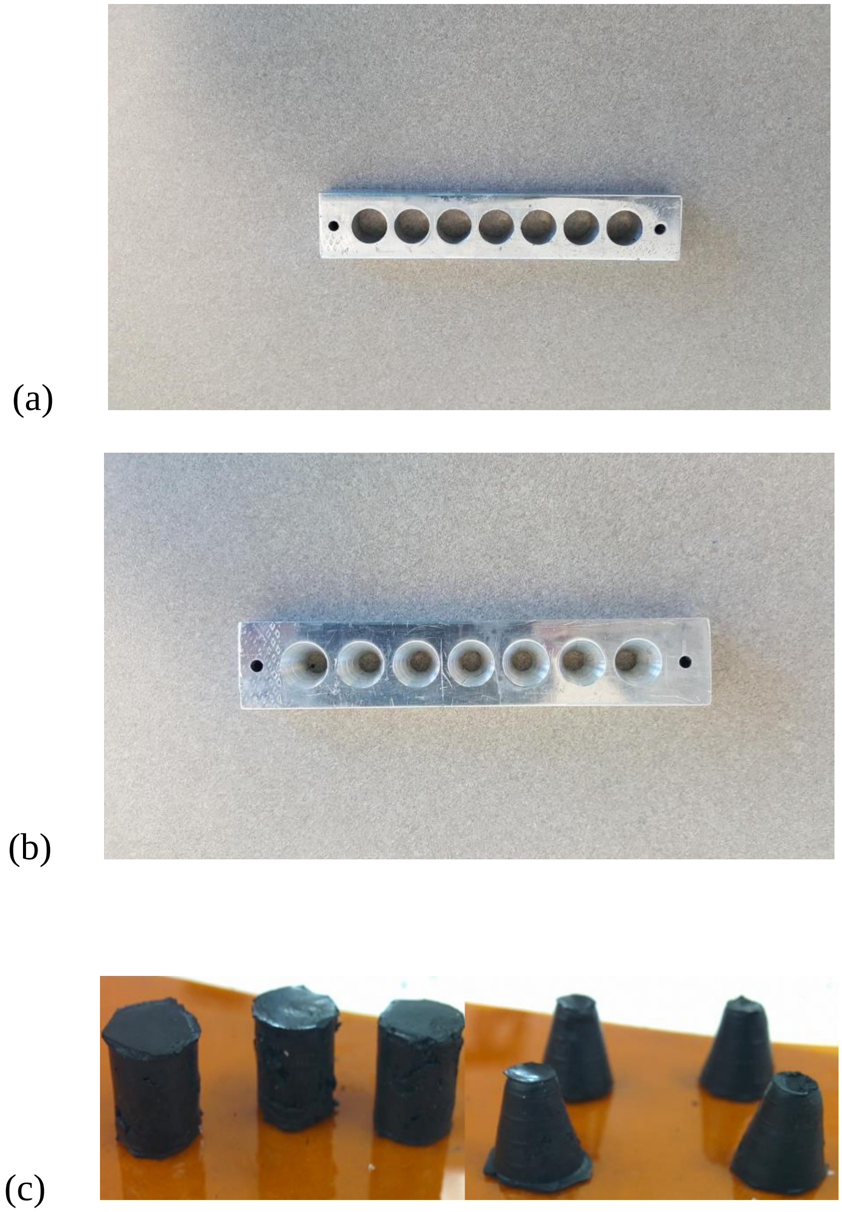

Figure 4.13: Photographs of (a) cylinder shape mold (b) cone shape mold (c) fabricated nanocomposites.

Figure 4.14 shows excellent sensing response of specimens with modified shapes at different maximum strains for 5 repeatable compression cycles and it clear that there is significant improvement compared to initial cubic shape results. Table 4.3 summarizes the gauge factors at different strain levels which shows at least 3 fold improvement. It is noted that the cylinder-shaped sensing unit was more sensitive at lower strain value (strain ~10%), but its sensitivity was significantly reduced when the strain value increased. On the other hand, the cone-shaped sensing unit is less sensitive in the lower strain range, but its sensitivity increases with higher strain values (strain >10%).

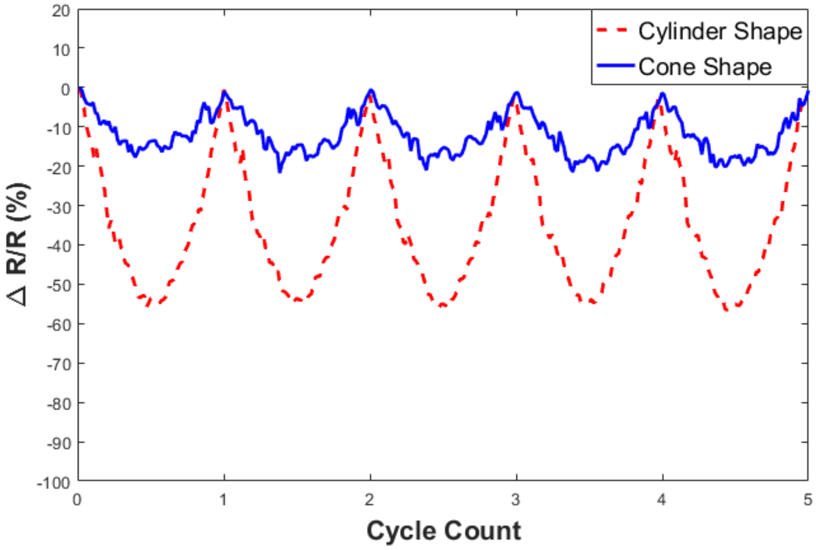

(a)

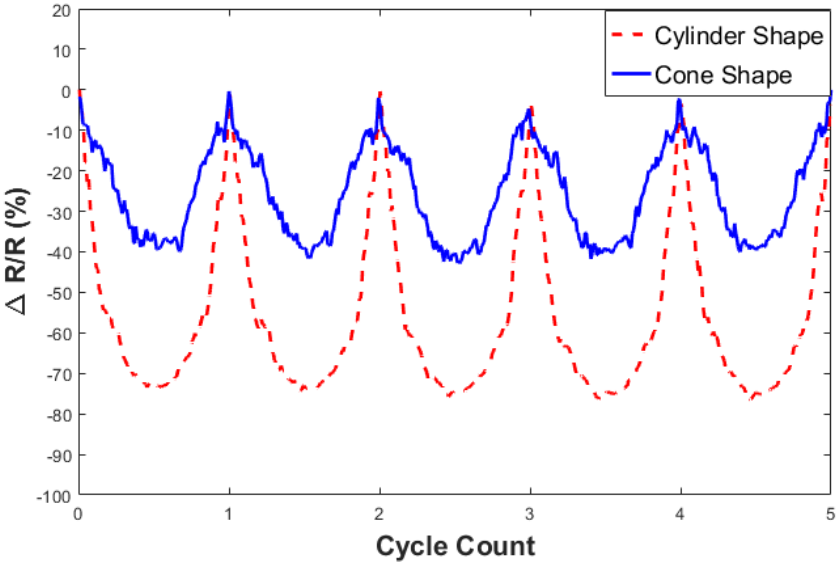

(b)

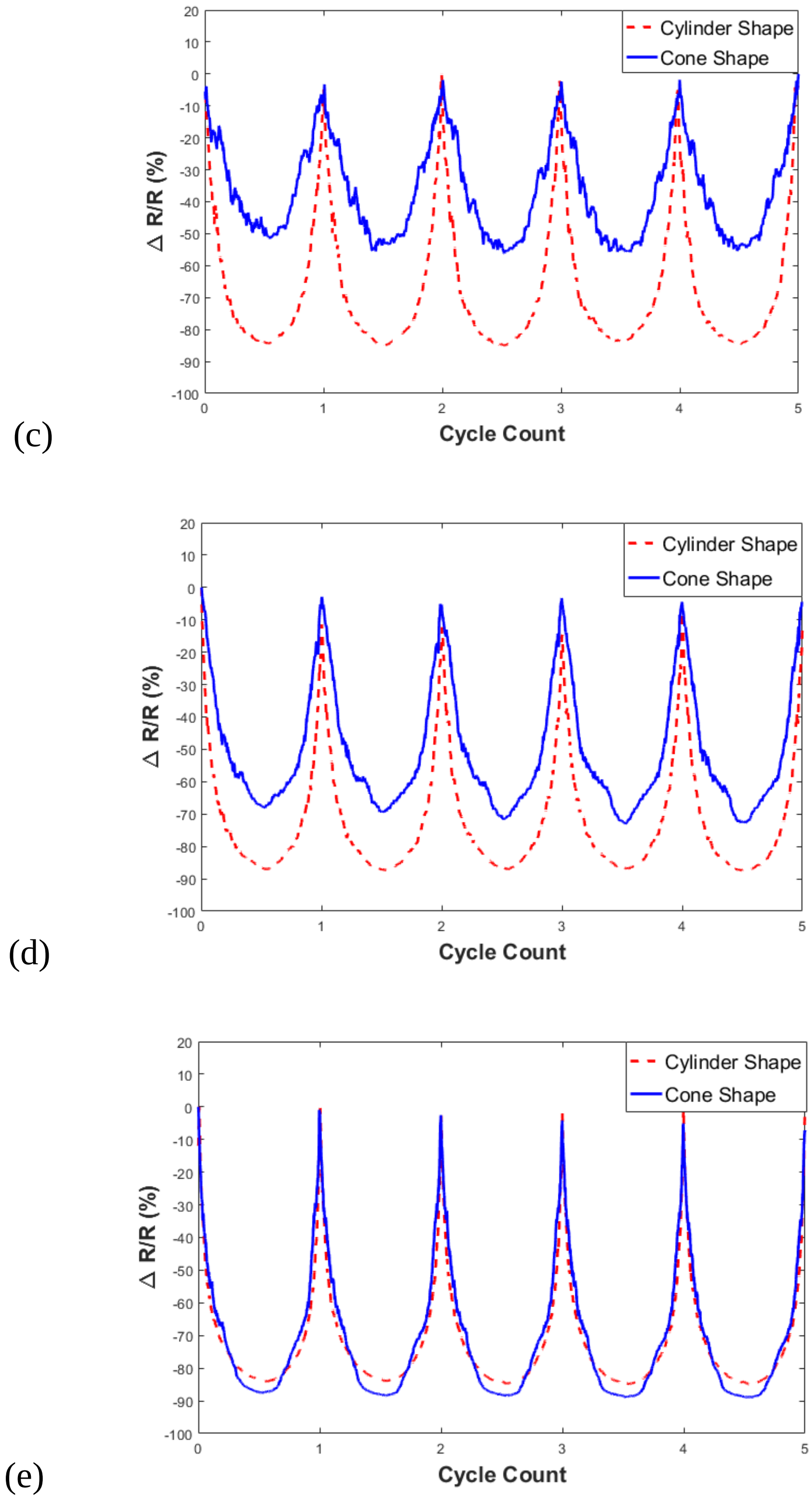

Figure 4.14: Sensing responses of PDMS nanocomposites sensing units of different shapes under compressive loading at: (a) 3% (b) 5%, (c) 10%, (d) 13%, and (e) 25% maximum strain.

Table 4.3: Gauge factor of cylinder and conical shape nanocomposites under compressive load conditions.

	Gauge Factor	
	Cylinder Shape	**Cone Shape**
3% Strain	18.3	6.3
5% Strain	14.8	8
10% Strain	8.2	5.5
13% Strain	6.6	5.4
25% Strain	3.51	3.52

These results indicate that by varying geometric shape, the optimum nanocomposite material unit can be used as flexible pressure and strain sensor for a wide range of loading conditions with improved and superior gauge factors.

4.2.2 Robustness and Durability of the Sensing Response

In order to commercially apply the sensing units as strain/pressure sensors, they have to be robustly operable over a wide range of strain rate. Compressive loading tests were performed on conical shape units with strain rate varying from 5% strain/min to 200% strain/min for multiple cycles and the results showed almost no effect of the strain rate on the overall response (Figure 4.15:a).The maximum percentage resistance change between loading and unloading cycle was almost constant regardless of the loading rate. To verify the durability of the sensing units, 1000 cyclic tests were performed at 27% maximum strain which produced excellent repeatable results in terms of maximum change in resistance which varied only from 92% to 96% over the course of 1000 cycles which is minimum considering the duration of the experiment. (Figure 4.15: b, c). Typical response of a single loading-unloading cycle is showed in Figure 4.15: d where three stages of sensing response can be observed as strain is increased to maximum 27%. So, it can be concluded that depending on the operating strain range, different slopes of the sensing response is generated as verified by Table 4.3 as well.

The resistance of the sensing unit also successfully returns almost to the initial value with very little hysteresis.

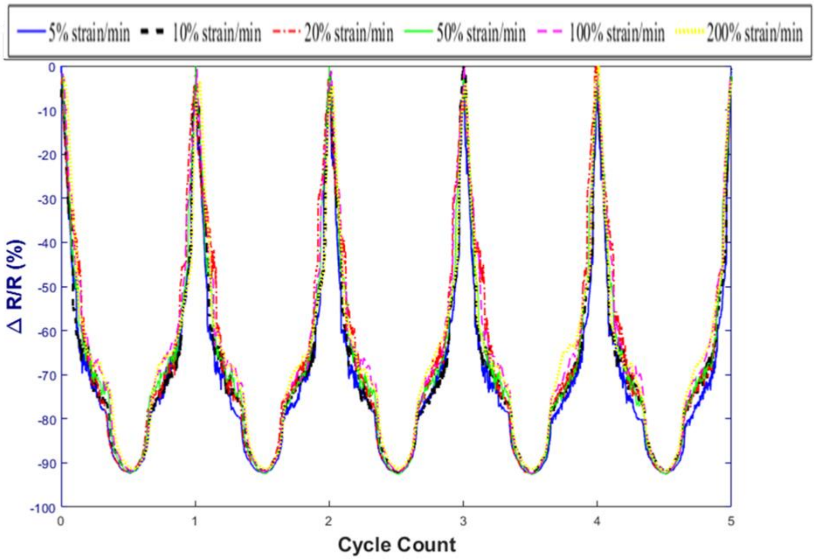

(a)

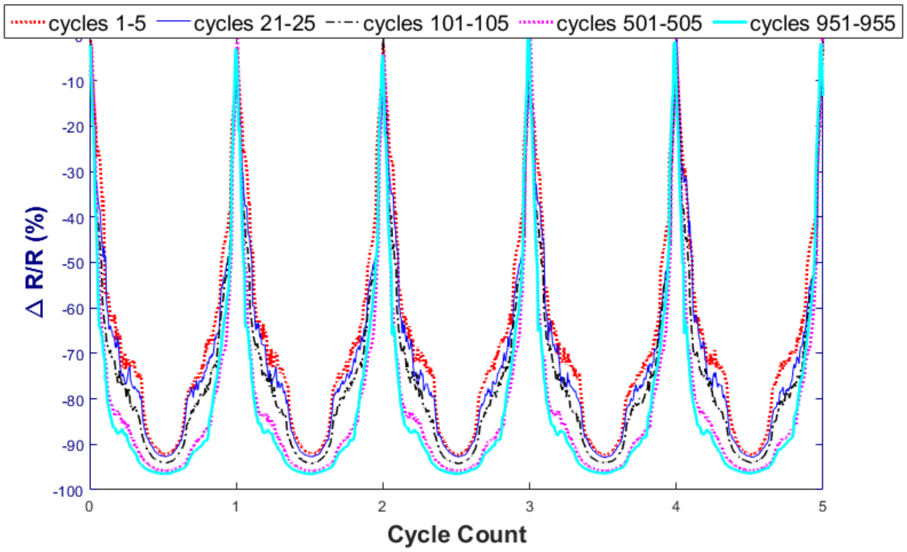

(b)

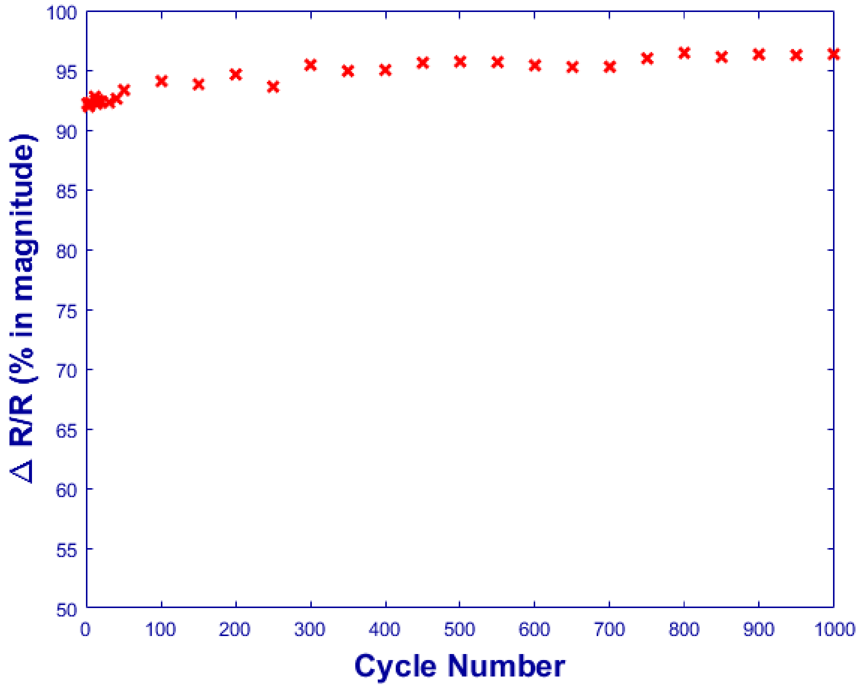

(c)

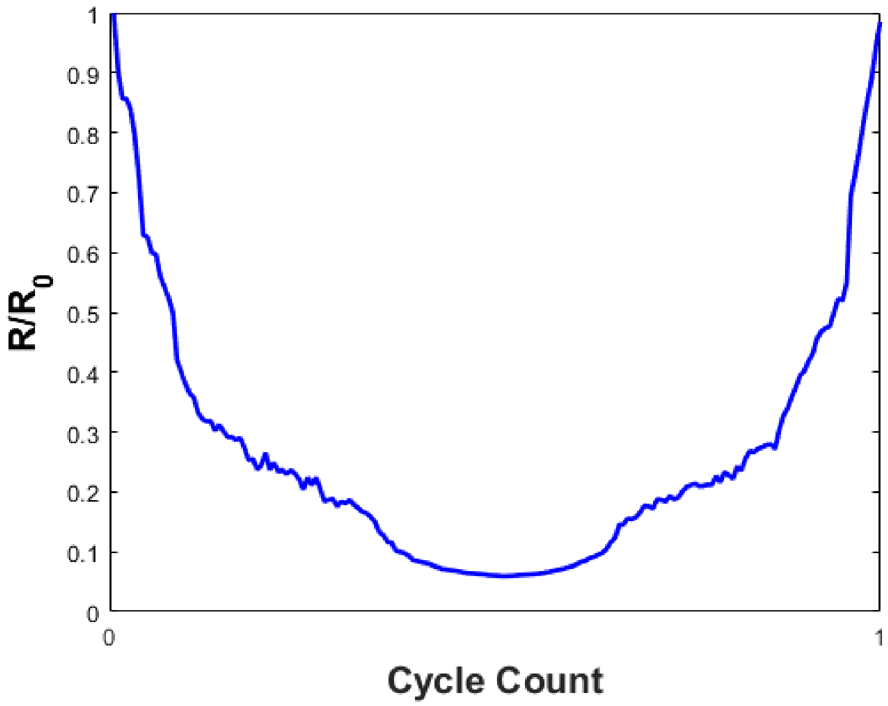

(d)

Figure 4.15: Sensing response showing reliability of the sensor at 27% maximum strain (a) strain rate effect (b-c) response over 1000 cycles (d) typical response of a single cycle showing instantaneous resistance as a function of initial resistance.

In this chapter, developed electrically conductive nanocomposites were studied for sensing functions under both tension and compression loading conditions. In tension loading, 30% maximum strain was applied whereas for compression loading three maximum pressures as 50, 100, and 150 psi were applied. Gauge factor was quantified for each material for both tension and compression loading conditions. These results helped identifying the nanocomposite with 8% CNF content and 10:2 polymer to silica ratio as the optimum material due to high gauge factors. The sensitivity of the ideal candidate material was improved by forming sensing units of different shapes as cylinder and cone shape. The ideal material sensing units also showed excellent robustness when loading rates were varied over orders of magnitude. Finally, to study the durability, 1000 cyclic tests were performed which revealed almost constant sensing response of the unit.

Chapter 5 Maximizing Sensing Response by Shape Optimization

Piezoresistance is a property by which a material's electrical resistance changes with applied load or strain as described in previous chapter. Therefore, theoretically, the piezoresistive sensing functions can be maximized by maximizing stress and strain resultants. Henceforth, in order to maximize the sensitivity of the overall sensor array, each sensing unit will be optimized by selecting the appropriate shape and adjusting critical geometrical parameters using both finite element analysis (FEA) and optimization algorithms. The objective of this chapter is to optimize the geometric dimensions of the ideal CNF/PDMS nanocomposite (8wt% CNF 10:2 polymer to silica ratio) sensor units under different pressure ranges (<50 psi, 50-100 psi, and 100-150 psi) using FEM and structural optimization algorithm. Static structural analysis based FEM simulation using commercially available ANSYS Workbench was first conducted. After that appropriate design points were identified within the operable range of each key parameter using central composites design algorithm and then FEM simulations were completed at those selected design points. Thereafter, the response surface of the key parameters, such as radius, height, and maximum stress/strain, were generated using the Kriging model algorithm. Finally, the screening optimization algorithm was employed to identify the optimum geometric dimensions following the desired optimization objectives and constraints. Three different geometric shapes including cylinder, cone, and truncated pyramid shapes were explored. Figure 5.1 shows the schematic of the technical approaches of the FEM analysis and optimization methods that have been used.

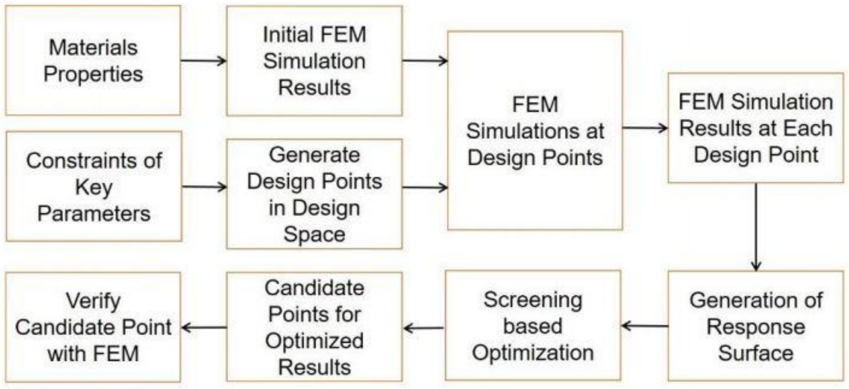

Figure 5.1: Flow chart of the FEM analysis and optimization process.

To obtain necessary inputs for structural optimization algorithms, FEM analysis was first performed for the selected shapes using experimental materials properties, idealized boundary conditions, and required pressure ranges. The experimentally characterized material properties for 8wt% CNF 10:2 ploymer to silica ratio material were used to generate a full stress-strain relationship using hyperplastic 2nd order MooneyRivlin model, and then was fed into all the FEM simulations as the required material properties. Once FEM simulation was accomplished and the design points within the design space were fully identified, then more simulations were completed to obtain all the required input information for optimization.

5.1.1 Material Properties

In literature, most previous modeling works simply treated PDMS as a linear elastic material in FEM simulations mainly to reduce the complexity or due to the lack of experimental data. It is reasonable to model PDMS as a linear elastic material when the deformation is small and within elastic range. However, for this study, the working pressure range results in a much higher deformation and strain. As a result, the assumption of linear elastic properties of PDMS and their nanocomposites will lead to inaccurate mechanics model. Hence, a hyperplastic material model by fitting experimentally obtained material properties under compression using Mooney-Rivlin three parameters model fit was used [61]. Figure 5.2 shows the fitted material property using the hyperplastic model. All the FEM simulations were created using the fitted material properties.

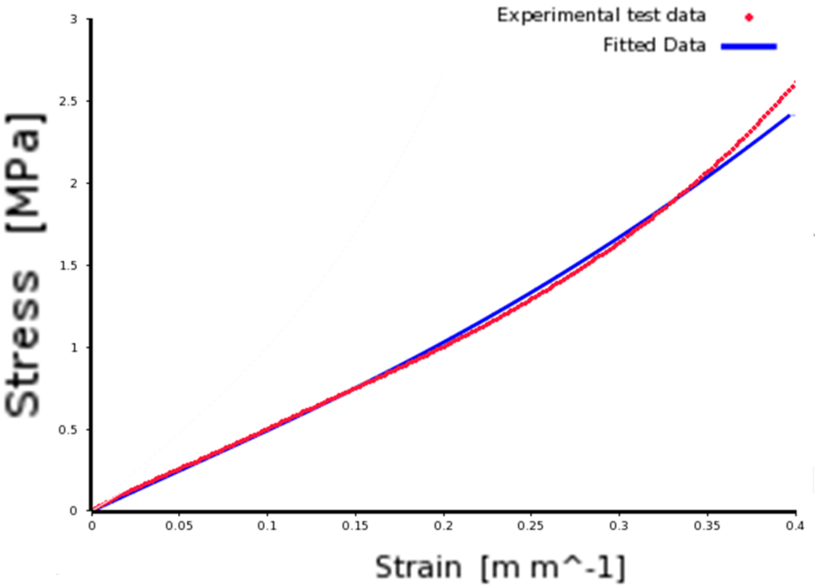

Figure 5.2: Curve fitting of hyper-elastic material model and experimental data.

Central composite design with face-centred-cubic (FCC) model was used to select design points distributed throughout the design space. For cylinder shape specimens, radius of the cylinder (X_1) and height (X_2) was used as the independent variables whereas three independent variables; radius of bottom surface (X_1), radius of top surface (X_2),and height (X_3) ; were required for the conical shape sensing units. Output dependent parameters were magnitude of maximum compressive stress (Y_1) and maximum compressive strain (Y_2). The total number of design points were generated by the formula:

$$Number\ of\ design\ point = 2^k + 2 * k + cp \tag{10}$$

where, k= number of independent variables, 2^k= number of factor points, 2*k= number of axial points, and cp= number of central points [62-64]. So, a total of 9 design points (22+2*2+1=9) and 15 (2^3+2*3+1) design points were used in the case of cylinder and conical shape unit optimization respectively. It is to be noted that extreme values of the design points were selected based on total deformation and manufacturable dimensions.

5.1.2 Response Surface Generation

Response surface method was used to spatially interpolate the whole design space from the obtained FEM results at the design points generated by central composite design. Kriging algorithm is the engine behind the response surface generation which in principal predicts the output of a function at desired points by computing weighted average of the known output of the same function at neighboring points. It is a suitable method for this study due to its unbiased estimation with minimum error. The response surface gives the expected maximum stress or maximum strain using any combination of geometric parameters by interpolation without actually involving large matrix inversion involved in FEM simulation and thus minimizing computational cost and time siginificantly. The algorithm used for Kriging method can be expressed by the following formula [65]:

$$Y^*(x_0) = \sum_{i=1}^{n} \lambda_i\,(x_0\,)Y(x_i) \qquad (11)$$

where, $Y^*(x_0)$ is the estimated value of the output parameters at desired spatial location x_0, $Y(x_i)$ is the values of output parameters at design points obtained by central composite design method, and $\lambda_i\,(x_0\,)$ are the weights associated with output at design points with additional constraints that $\sum_{i=1}^{n} \lambda_i\,(x_0\,) = 1$ relation has to be satisfied. To show the reliability of the generated response surface, goodness of fit for both output parameters are shown in Figure 5.3 which clearly indicates excellent linear fit.

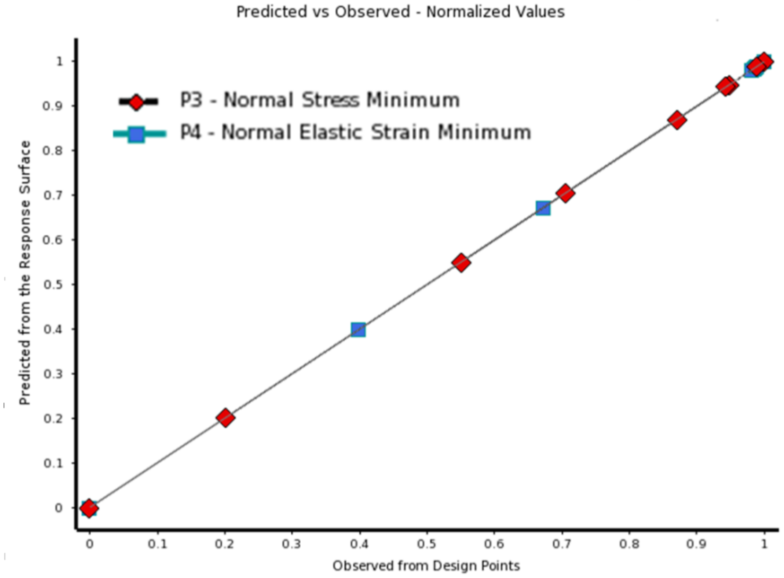

Figure 5.3: Graph showing goodness of fit for both maximum compressive stress and strain.

5.1.3 Goal Driven Optimization

Goal driven optimization (GDO) is an algorithm where the output parameters are optimized with respect to required objectives and constraints. The goal of the proposed sensing unit's geometric structure optimization is to find the optimal and critical geometric parameters that will result in the highest magnitude of both compressive stress and strain. However, the highest stress and highest strain may not be generated simultaneously at same design point and thus appropriate trade-off has to be made so that both the stress and strain can reach relatively high value at the optimal points. Shifted Hamersley Sampling Method or Screening algorithm; which is in principle an optima search method; was used to find the design points that results in optimum compressive stress and strain [66, 67]. Depending on the objectives and constraints, the inherent algorithm generated a few candidate points. Finally, the optimum design points generated by the optimization algorithm were verified using FEM simulations.

Using correct constraints for sensitivity optimization is critical for the success of the proposed optimization approach. The preliminary experimental results obtained from initial shapes demonstrated that the cylinder shaped sensing units had the highest sensitivity under relatively low compressive strain range (Figure 4.14). Therefore, optimizing cylinder-shaped sensor units were performed under two low pressure ranges (<50 psi and 50-100 Psi) only. Therefore, additional constraint can be applied to optimization algorithm as the maximum compressive strain should be as close as 10%. On the other hand, the cone-shaped sensor units had higher sensitivity at higher strain level. Therefore, the cone shape was chosen for the pressure sensing in the range of 100 and 150 psi pressure. Additional constraint was used as the compressive strain has to be more than 10%.

5.2 Optimization of Cylinder Shape Sensor Unit

As discussed in previous section, optimizing cylinder-shaped sensor units were focused on two relatively low pressure ranges (<50 psi and 50-100 Psi) only. The boundary conditions of the simulated FEM model are shown in Figure 5.4. The bottom surface was fixed in the loading direction. The friction at the top and bottom surfaces were not considered in these FEM simulations. Static unidirectional compressive pressure load was applied to the top surface of the cylinder sample. The load condition used in the FEM simulations was the same as those in the experiments conducted and thus mimicking the closest ideal condition. At first, one FEM simulation was conducted using cylinder-shaped sensor unit with the radius of 5 mm and the height of 10 mm similar to initial experiments conducted.

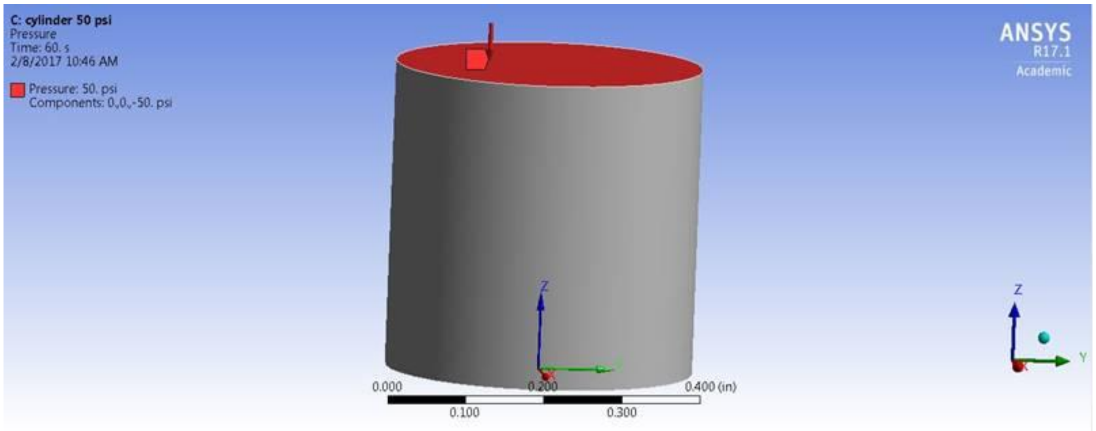

Figure 5.4: Loading and boundary condition for initial FEM analysis.

Figure 5.5 shows the simulation results for compressive stress and compressive strain in loading under 50 psi applied pressure. As expected, the stress was uniform at and near the top face and strain is less than 10%. To limit the radius and height variation within the reasonable ranges, the optimization constraints of these two parameters were designed considering the reasonable geometry for cylinder sensor units. Therefore, radius of the cylinder ranged from 1-5 mm and cylinder height ranged from 3-10 mm. Once the design points were all selected within the constraints of radius and height, nine more FEM simulations were conducted by adjusting the radius and height. The load pressure was kept constant at 50 psi in all the simulations. The maximum stress and max strain were recorded after completing each FEM simulation. Once the required simulations were completed, the results were feed backed into the Kriging model algorithm and used to find the response surfaces regarding to both dependent variables maximum stress and strain. The geometric parameters including radius and height were used as the control parameters to calculate maximum stress and max strain, finally resulting in the generation of the response surfaces. Either maximum stress or strain was used as the outcomes of each response surface plot. Therefore, two response surface plots were created, one for the identification of maximum stress, and the other one for the identification of maximum strain.

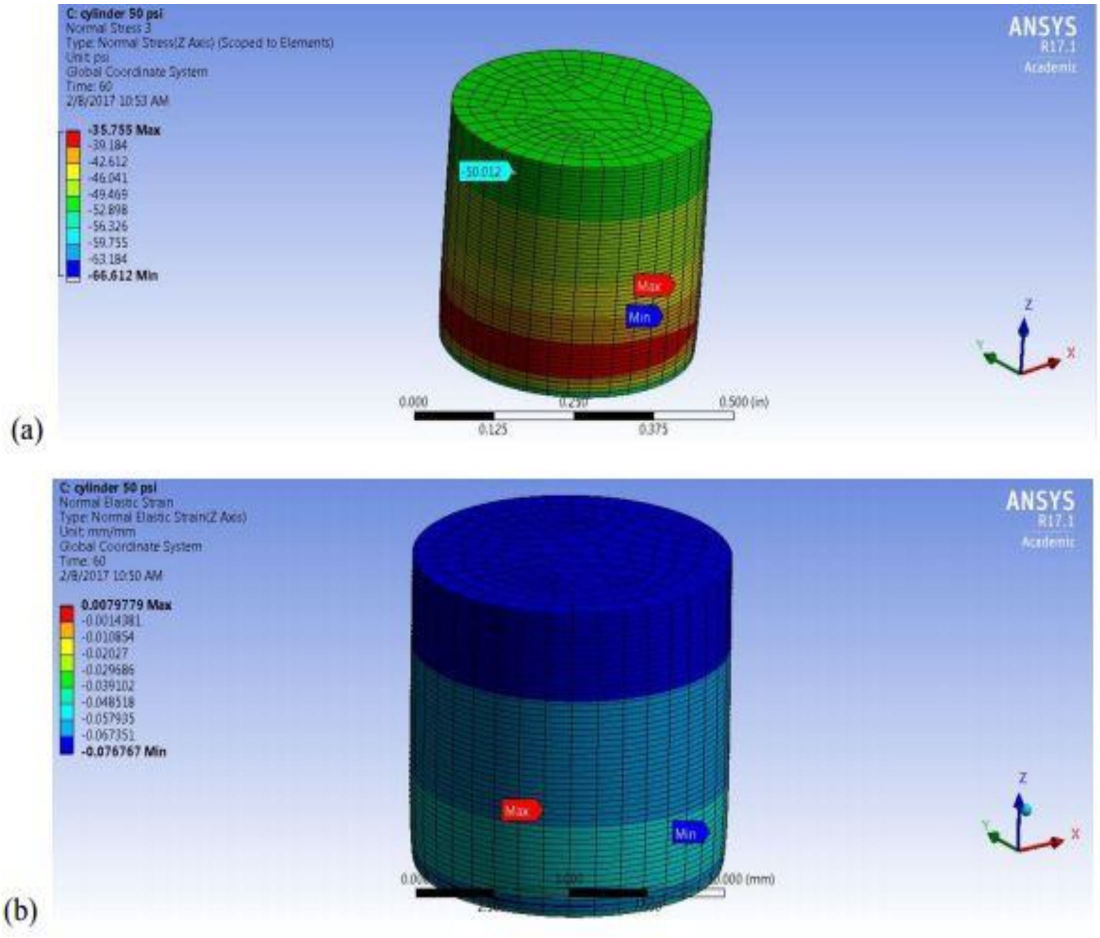

Figure 5.5: FEM simulation results showing (a) normal stress and (b) strain in loading direction under 50 psi pressure.

Figure 5.6 shows the response surface between input parameters and output results, such as compressive stress and strain. From the response surface, some critical information about how output parameters vary with each input design parameter can be identified. It is clear from Figure 37 that both maximum compressive stress and compressive strain increases (in terms of magnitude) with increasing radius and decreasing height of the cylinder. For the GDO algorithm, constraints such as the maximum strain should be less than 10% which was obtained from the experimental result indicating maximum sensitive range was also added. Figure 5.7 shows the summary of output design parameters for five different candidate points. It is clear that some of them are satisfied and some of them have failed to satisfy the required constraints. It can be seen that candidate point 1 with cylinder radius 5 mm and height 3 mm gives the best result in terms maximizing the stress and strain.

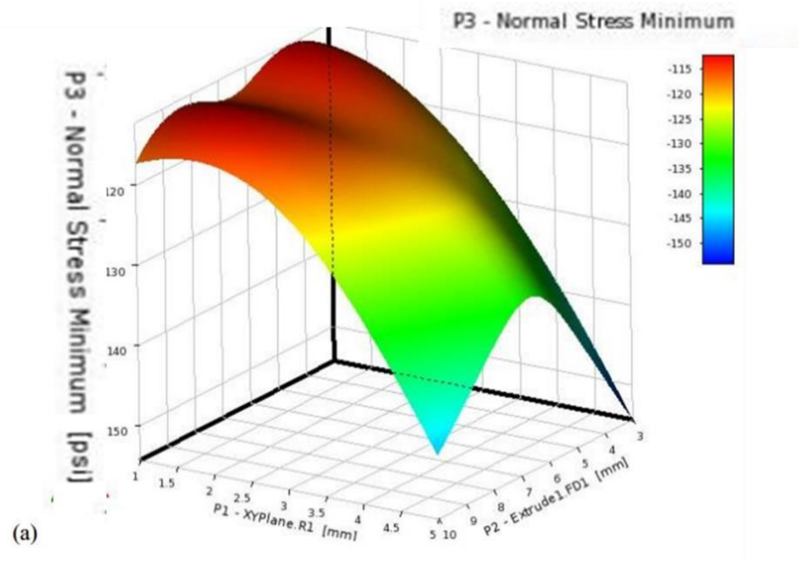

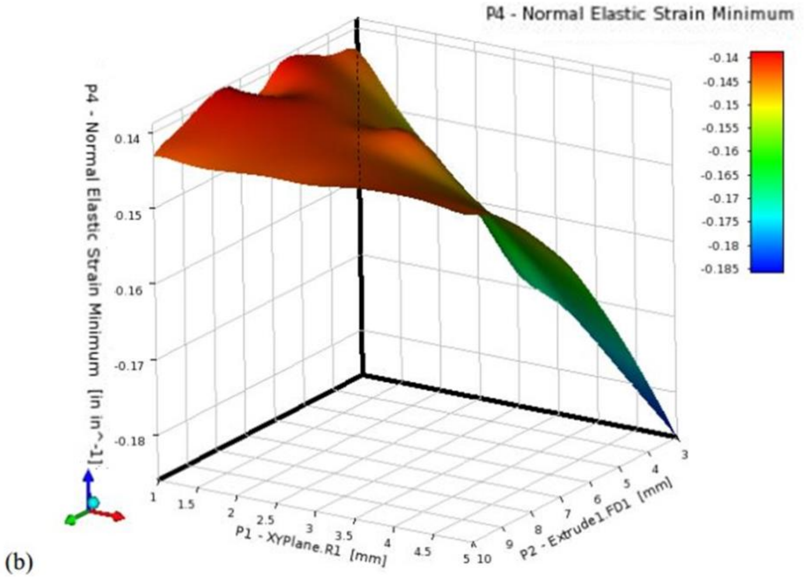

Figure 5.6: 3D response surface showing variation of (a) maximum compressive stress and (b) compressive strain as a function of input design parameters of radius (R1) and height (FD1) of cylinder.

Reference	Name	P1 - XYPlane.R1 (mm)	P2 - Extrude1 .FD1 (mm)	P3 - Normal Stress Minimum (psi)		P4 - Normal Elastic Strain Minimum (in in^-1)	
				Parameter Value	Variation from Reference	Parameter Value	Variation from Reference
●	Candidate Point 1	5	3	★★★ -69.13	0.00 %	★★ -0.09037	0.00 %
○	Candidate Point 1 (verified)			★★★ -69.13	0.00 %	★★ -0.09037	0.00 %
○	Candidate Point 2	4.986	4.0904	★★ -66.159	4.30 %	★★ -0.086779	3.97 %
○	Candid... Point 2 DP 2 (verified)			★ -65.672	5.00 %	★★ -0.087655	3.00 %
○	Candid... Point 3 DP 3	4.978	4.9654	★ -64.674	6.45 %	★ -0.084027	7.02 %
○	Candidate Point 4	4.826	4.692	★ -64.375	6.88 %	★ -0.0844	6.61 %
○	Candidate Point 5	4.474	4.0631	★ -63.763	7.76 %	★ -0.085193	5.73 %

Figure 5.7: Generated optimum candidate points for cylinder shape under 50 psi pressure.

As these results are obtained from response surface approximation only, the optimum design point needs to be verified using actual FEM simulation. Figure 5.8 shows the FEM results of the selected design points with maximum compressive stress and strain. The FEM simulations results verified that the selected geometric parameters for the cylinder sample has the largest resultant stress and strain at the applied pressure of 50 psi, which will result in the highest pressure sensitivity. The exactly same approach was used for 100 psi applied pressure and same design point with 5 mm cylinder radius and 3 mm height was found to be the best candidate.

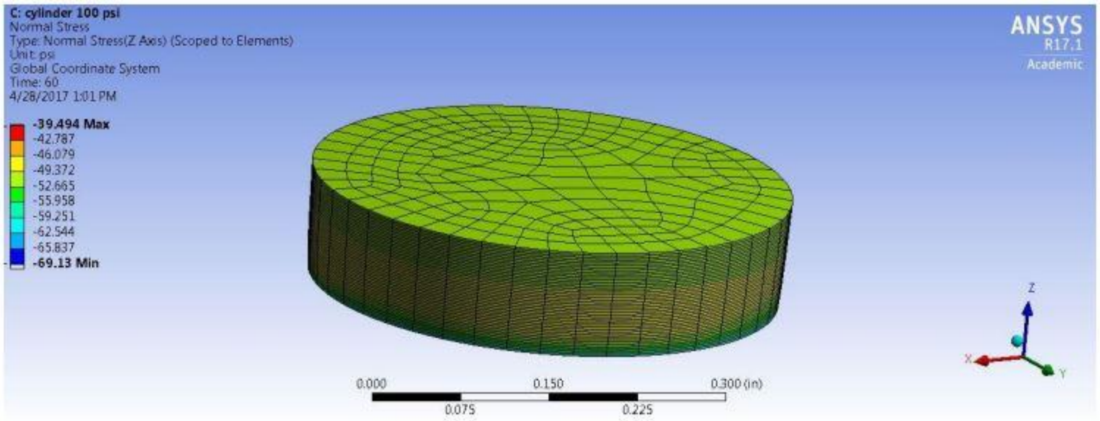

(a)

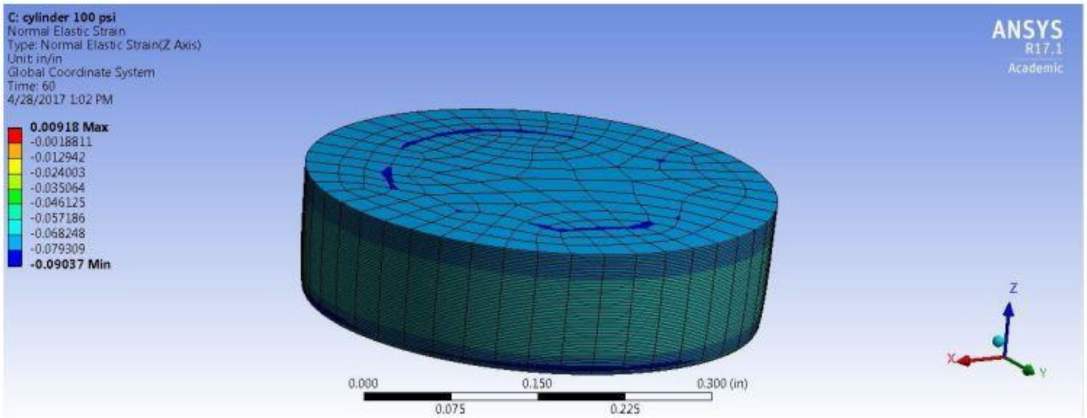

(b)

Figure 5.8: FEM results showing (a) normal stress and (b) strain of the optimum cylindrical shape under 50 psi pressure.

5.3 Optimization of Conical Shape Sensor Unit

The preliminary experimental study showed that the cone-shaped sensor units had higher sensitivity at larger strain level. Therefore, the cone shape is chosen for the pressure sensing at 100 and 150 psi pressure range. Similar loading and boundary conditions as the cylinder shape were applied. The bottom surface was fixed in loading direction. Pressure load was applied on top surface under the selected load value. Figure 5.9 shows the load conditions and initial FEM results for 100 psi applied pressure. As expected, normal stress is almost 100 psi at and near top surface as well as uniform. As the cross-sectional area is reduced, compressive stress at bottom surface also gets reduced. Initial cone shape was with 5 mm radius of bottom face, 2.5 mm radius of top face and 10 mm height for the cone. For cone shape, now there were 3 input design parameters. Radius of bottom face (XY Plane.R1) ranging from 4-5 mm, radius of top surface (Plane4.R1) ranging from 0.5- 2.5 mm, and height (Plane4.FD1) ranging from 3-10 mm are the input parameters, respectively. In order to obtain the optimal cone shape dimension for up to 100 psi pressure range, the goal is to maximize both the compressive stress and strain. Also, one constraint as the maximum strain should be more than 10% can be used which was obtained from experimental results. The resulted optimized shape should have shape with approximately 4.9 mm radius of bottom face, 2.45 mm radius of top face, and 3.4 mm in height. Figure 5.10 shows the verification of the optimum design point using FEM simulation. For 150 Psi pressure, similar design point was found to be the optimum one.

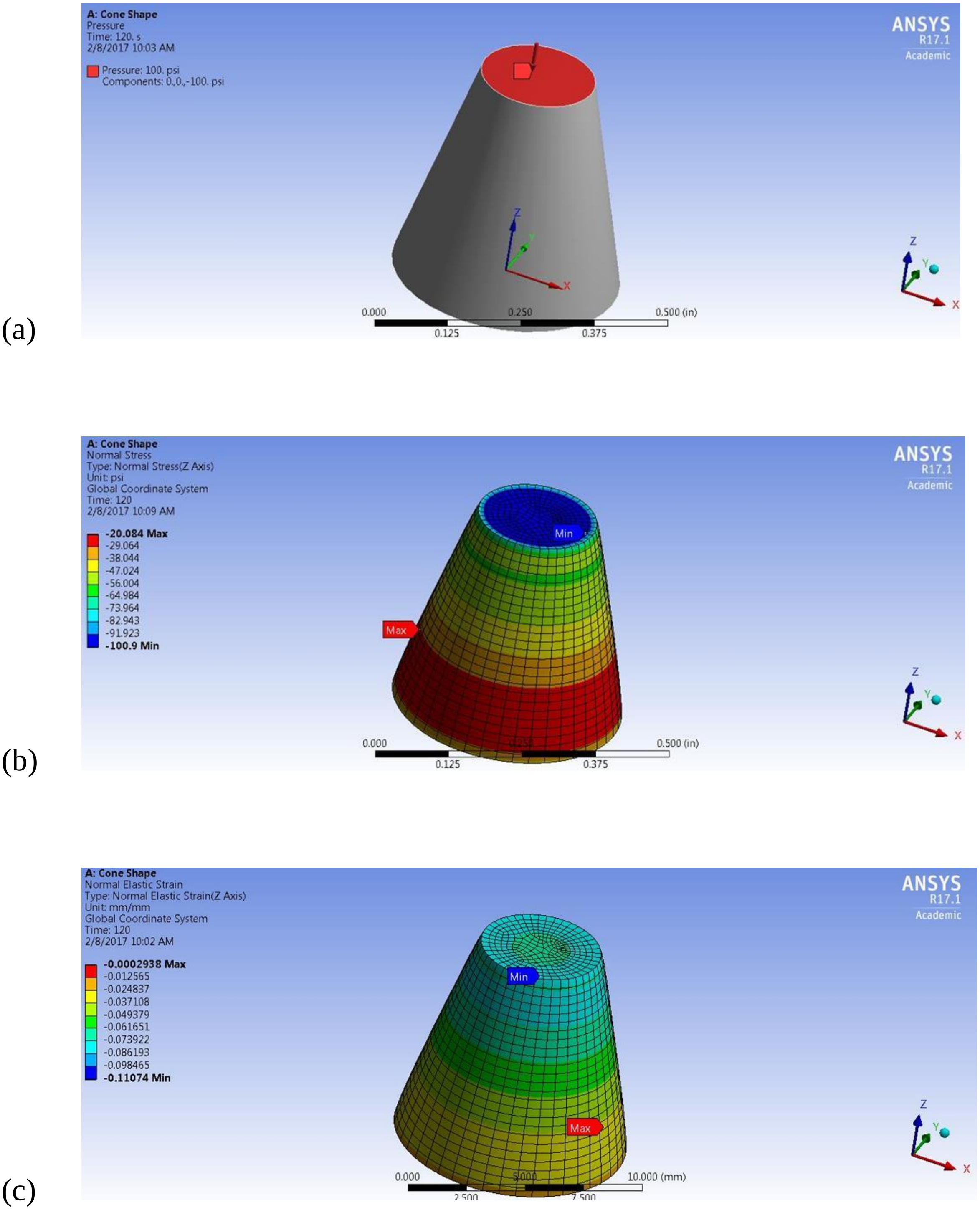

Figure 5.9: Initial FEM results showing (a) loading condition, (b) normal stress, and (c) strain in loading direction under 100 psi pressure for cone shape.

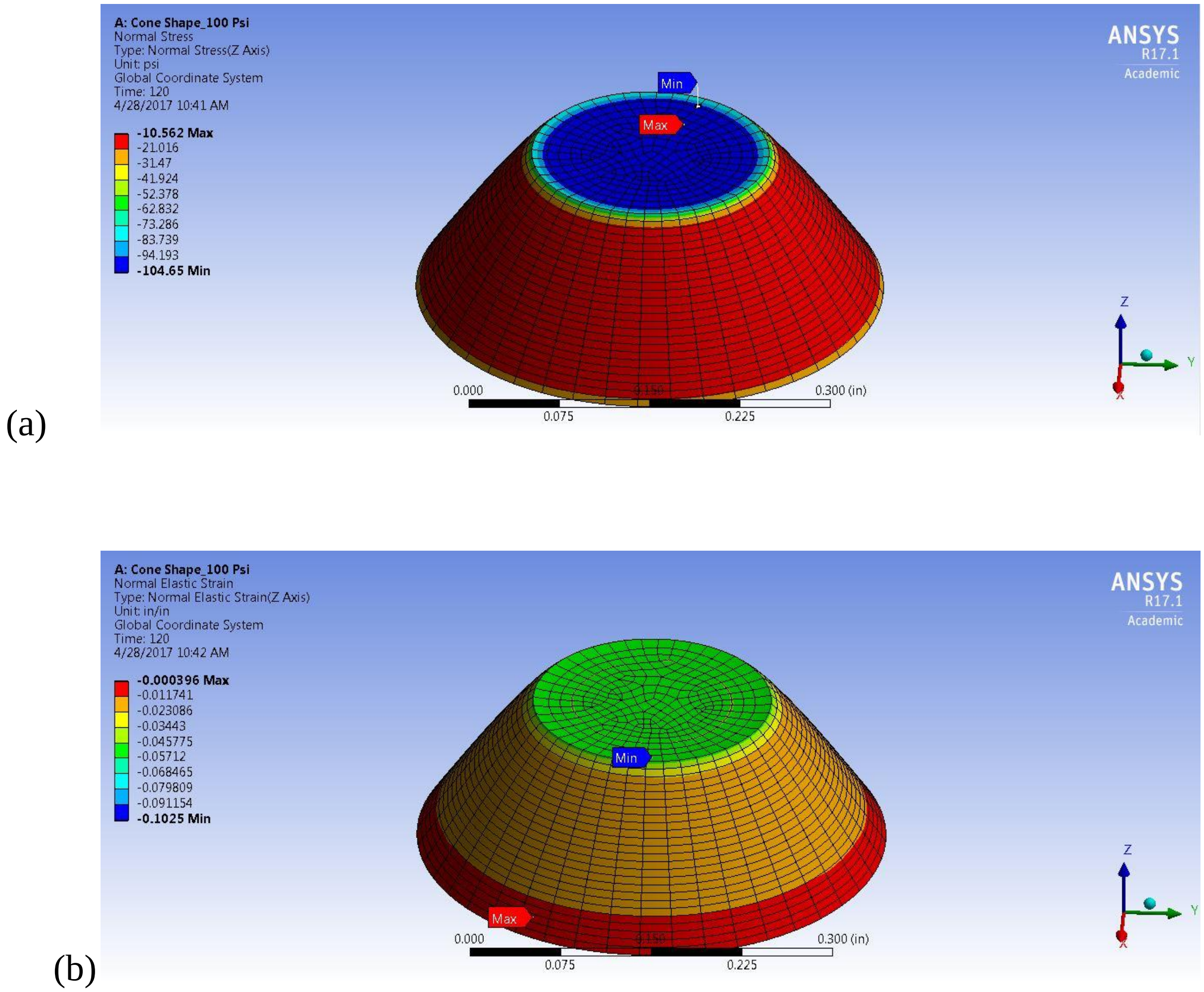

Figure 5.10: FEM results of the conical shape unit with optimum dimensions applied with 100 psi pressure showing (a) normal stress and (b) strain.

5.4 Optimization of Truncated Pyramid Shape Sensor Unit

Truncated pyramid is another shape that has been analyzed to obtain maximum piezoresistance sensitivity. Three input design parameters as size of the base, size of the tip of the pyramid, and pyramid height were used as independent variables. The maximum pressure of 100 psi was used for the optimization of truncated pyramid shape. Input design parameters of pyramid base length ranging from 6-10 mm, pyramid tip length ranging from 1-4 mm, and height ranging from 3-10 mm were selected. The optimization objective was to maximize the compressive stress and strain for the optimized shape while keeping the strain under 20%. The optimum shape obtained from FEM and optimization contains approximately 9.5 mm pyramid bottom base length, 2.3 mm tip base length, and 3 mm in height. Table5.1 summarizes the optimized dimensions obtained for three different shapes considered for this study.

Table 5.1: Dimensions of optimized shapes.

	Bottom radius/base (mm)	Top radius /base(mm)	Height(mm)
Cylinder shape	5	5	3
Cone shape	4.9	2.45	3.4
Truncated pyramid	9.5	2.3	3

5.5 Sensing Response of Optimized Shapes

Once optimized shape single sensing unit dimensions were identified by FEM and optimization algorithm, physical units were prepared and experimentally characterized under cyclic compressive loading conditions to experimentally verify the concept of maximizing the sensitivity. Figure 5.11 shows the fabricated optimum shape nanocomposites.

Figure 5.11: Photographs of nanocomposites with optimum shapes.

Figure 5.12 shows good repeatable 5 cycles for both cylinder and conical shape with optimized shape dimensions. It is clear from the Figure that indeed there is significant improvement in the sensing response at the same applied strain compared to the initial size specimens with highest resistance change as high as 98%. Also, sensitivity is improved in terms of much higher gauge factors.

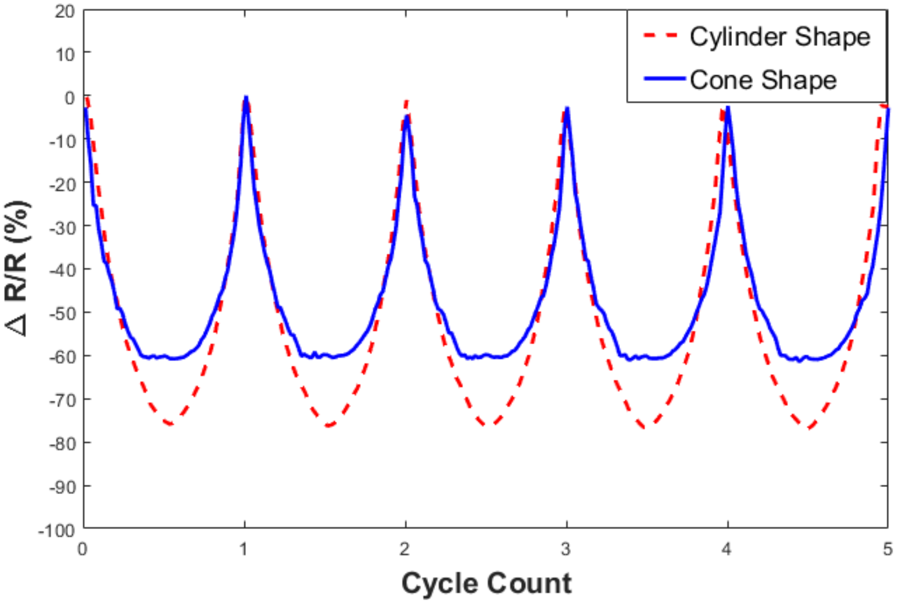

(a)

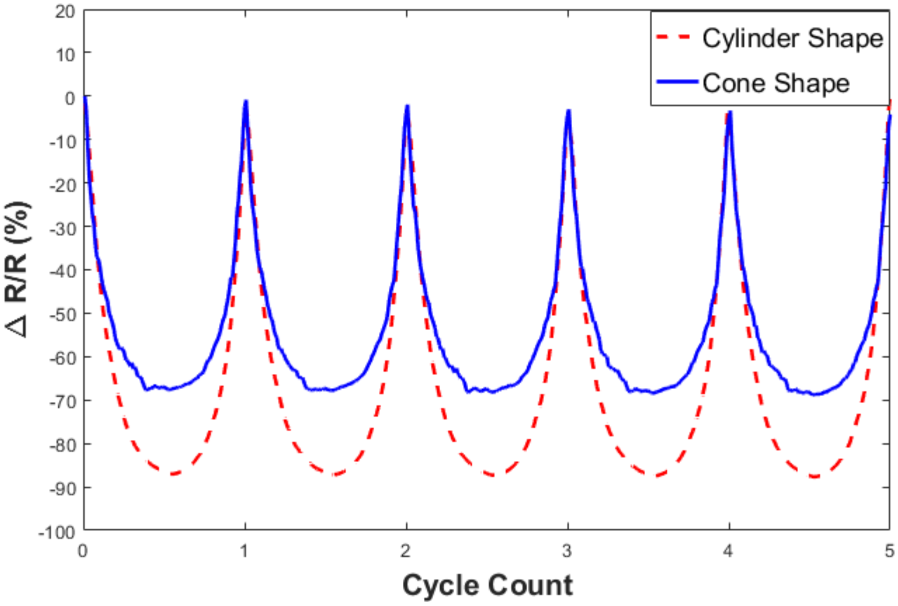

(b)

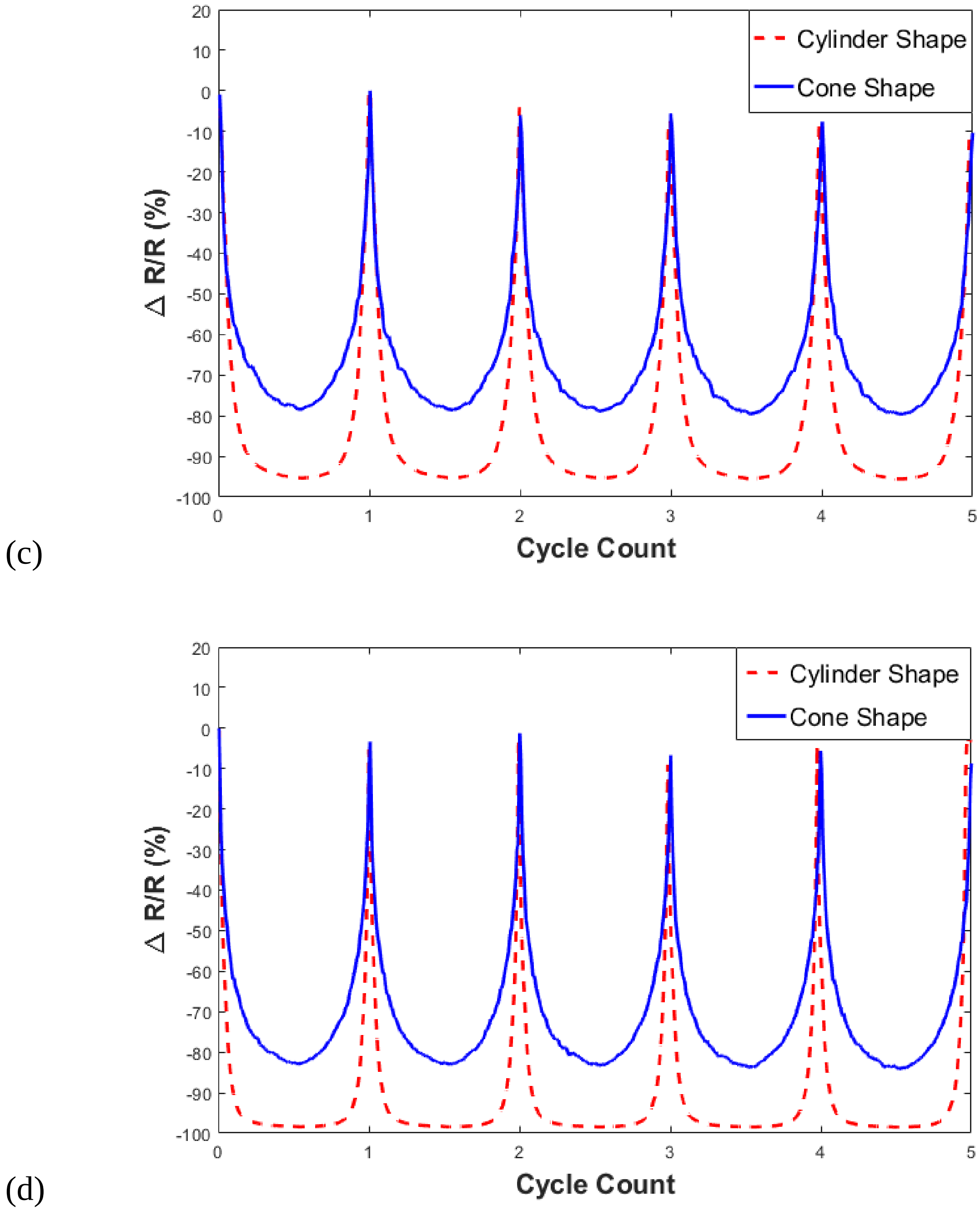

Figure 5.12: Sensing response of cylinder and cone shape nanocomposites with optimized dimension at (a) 3% (b) 5 % (c) 10%, and (d) 13% maximum compressive strain.

Although there was no initial experimental data to compare with in the case of truncated pyramid shape nanocomposites, they showed good repeatable sensing function with high sensitivity as well. Figure 5.13 shows the sensing response of the truncated pyramid shape specimen with optimized dimension and Table 5.2 summarizes the gauge factors.

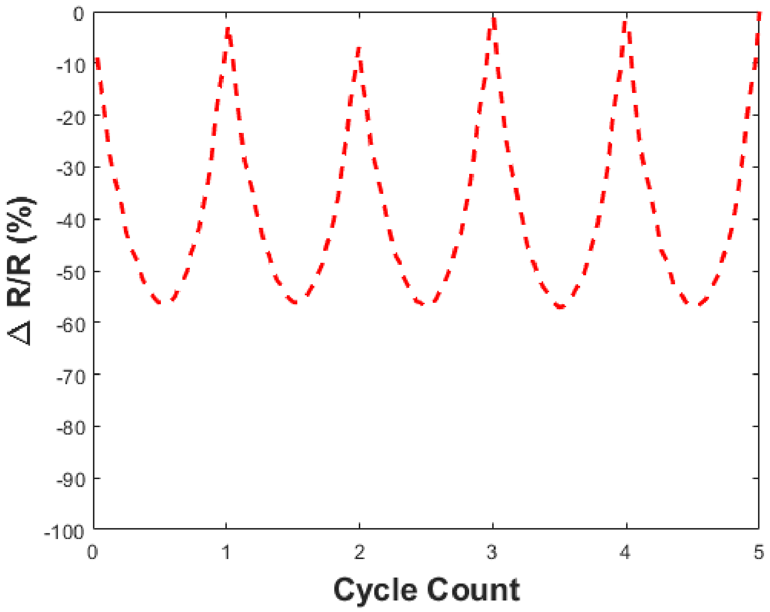

(a)

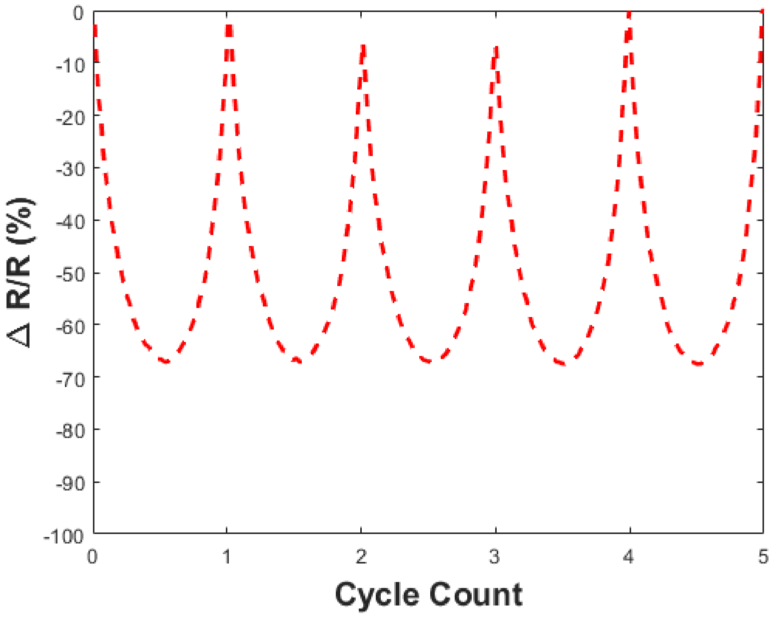

(b)

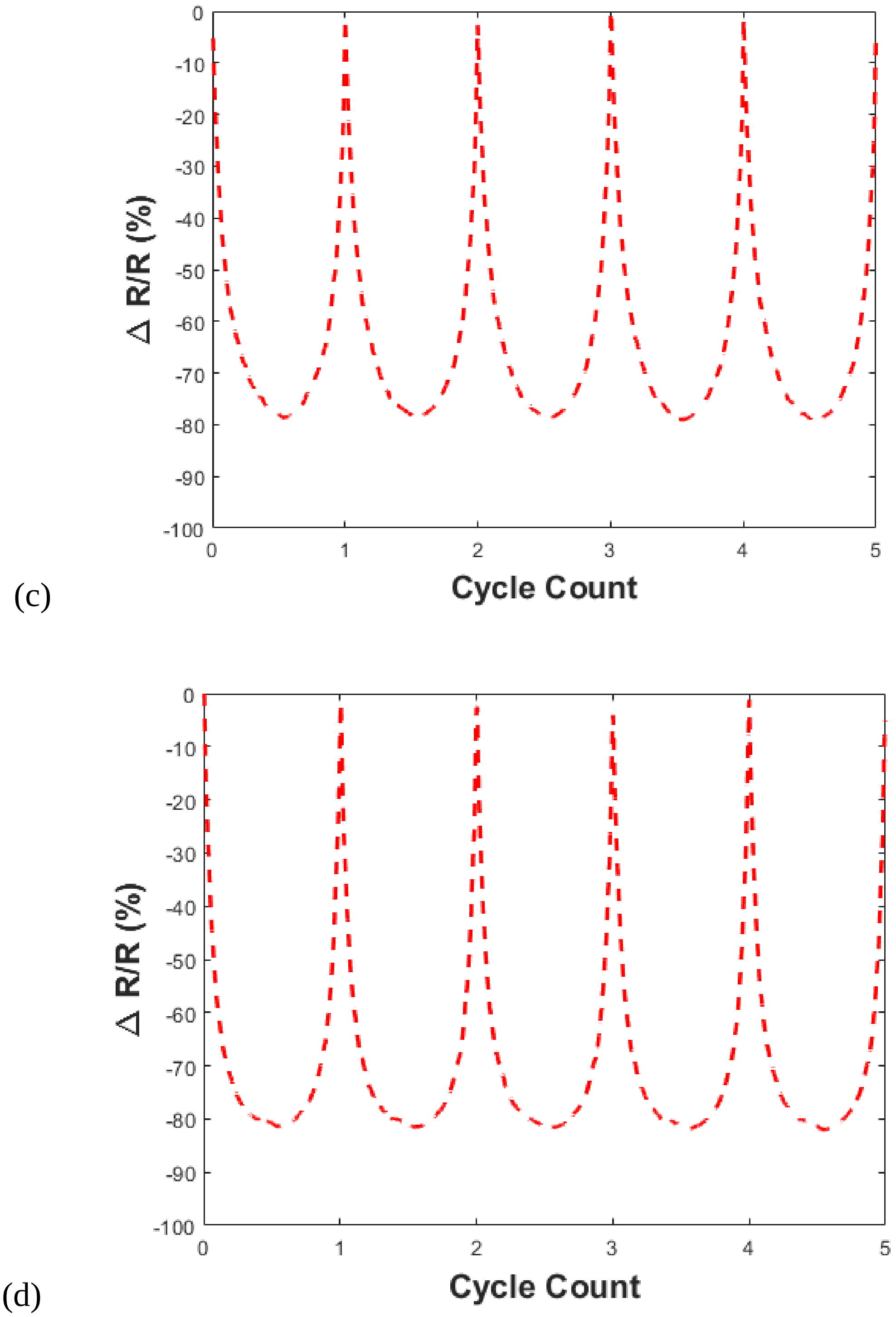

Figure 5.13: Sensing response of truncated pyramid shape nanocomposites with optimized dimensions at (a) 3% (b) 5 % (c) 10%, and (d) 13% maximum compressive strain.

Table 5.2: Gauge factor of sensing units of optimized dimensions showing improvement in sensitivity.

	Gauge Factor		
	Cylinder Shape	**Cone Shape**	**Truncated Pyramid**
3% strain	25	20	18.3
5% strain	17.4	13.4	13.4
10% strain	9.5	7.8	7.7
13% strain	7.5	6.3	6.1

In order to compare the sensitivity of the cylinder and cone shape sensing units with initial dimensions and with optimized dimensions, Table 5.3 can be referred to. It clearly shows the comparison and the maximizing of sensing functions between the gauge factors of same sensing units with initial dimensions and after structural optimization. For the cylinder shape units, an improvement of as high as 37% was achieved under 3% compressive strain. For cone shape sensing units, the improvement was much more substantial with as high as 217% improvement for 3% maximum compressive strain. Also, the similar trend is still noticeable in terms of higher sensitivity of cylinder shape units in the lower strain range region whereas cone shape units are more responsive in the higher strain range region.

Table 5.3: Comparison of gauge factors for cylinder and cone shape units before and after geometric structural optimization.

	Cylinder Shape			**Cone Shape**		
	Initial gauge factor	**Gauge factor with optimized structure**	**Percentage improvement**	**Initial gauge factor**	**Gauge factor with optimized structure**	**Percentage improvement**
3% strain	18.3	25	37%	6.3	20	217%
5% strain	14.8	17.4	18%	8	13.4	68%
10% strain	8.2	9.5	16%	5.5	7.8	42%
13% strain	6.6	7.5	14%	5.4	6.3	16%

In this chapter, the nanocomposite sensing unit with ideal material formulation has been optimized for structural dimensions. FEM and object based optimization algorithm are the two principal tools that have been used. Three unique shapes as cylinder, cone, and truncated pyramid shape units have been optimized to improve upon the bulk material's sensing response obtained from cubic shape units. Maximum resultant stress and compressive strain were the two desired output parameters that were maximized to obtain maximum piezoresistance sensing response. The physical dimensions generated by optimization algorithm for each of the unit were also verified by both FEM and experimental study under compression load. Experimental results showed significant improvement in gauge factors for both cylinder and cone shape units with optimized dimensions.

Chapter 6 Sensor Array

Once single sensing units of nanocomposites have been characterized for load sensing, the next step forward is to connect a number of units together in an array form mimicking large area deployable sensor prototype. That will be the main focus of this chapter. As a proof of concept, both cylinder and cone shape sensing units were connected in a row and column format resulting in a 3 by 3 array of cylinder and 4 by 4 array of cone shape units sensor prototypes. Similar works are well documented in literature [68]. Copper tapes have been used as the conductive electrodes for each row and column due to their very high conductivity, availability, good adherence to PDMS surface .Silver epoxy has been used to connect the sensing units with electrodes to ensure minimum contact resistance. Neat PDMS sheets were used at top and bottom to form a closed sandwich structure and provide insulative layers between sensing units. Single sensing unit was connected to a unique combination of row and column electrodes. The advantage of this type of connection is the ability of responding and sensing both distributed and differential pressures. Figure 6.1 shows the mesh grid manner of the 3 by 3 cylinder units array and 4 by 4 conical units array. Rows of the arrays were tagged as i= 1,2… and columns were tagged as j= A,B…etc. As a result each nanocomposite sensing unit contained unit identification such as 1A, 1B… etc. Each units were checked for any inadvertent short circuit connections. When testing for piezoresistance based sensing, two probe connections were provided to each unit by connecting wires to two electrode copper tapes.

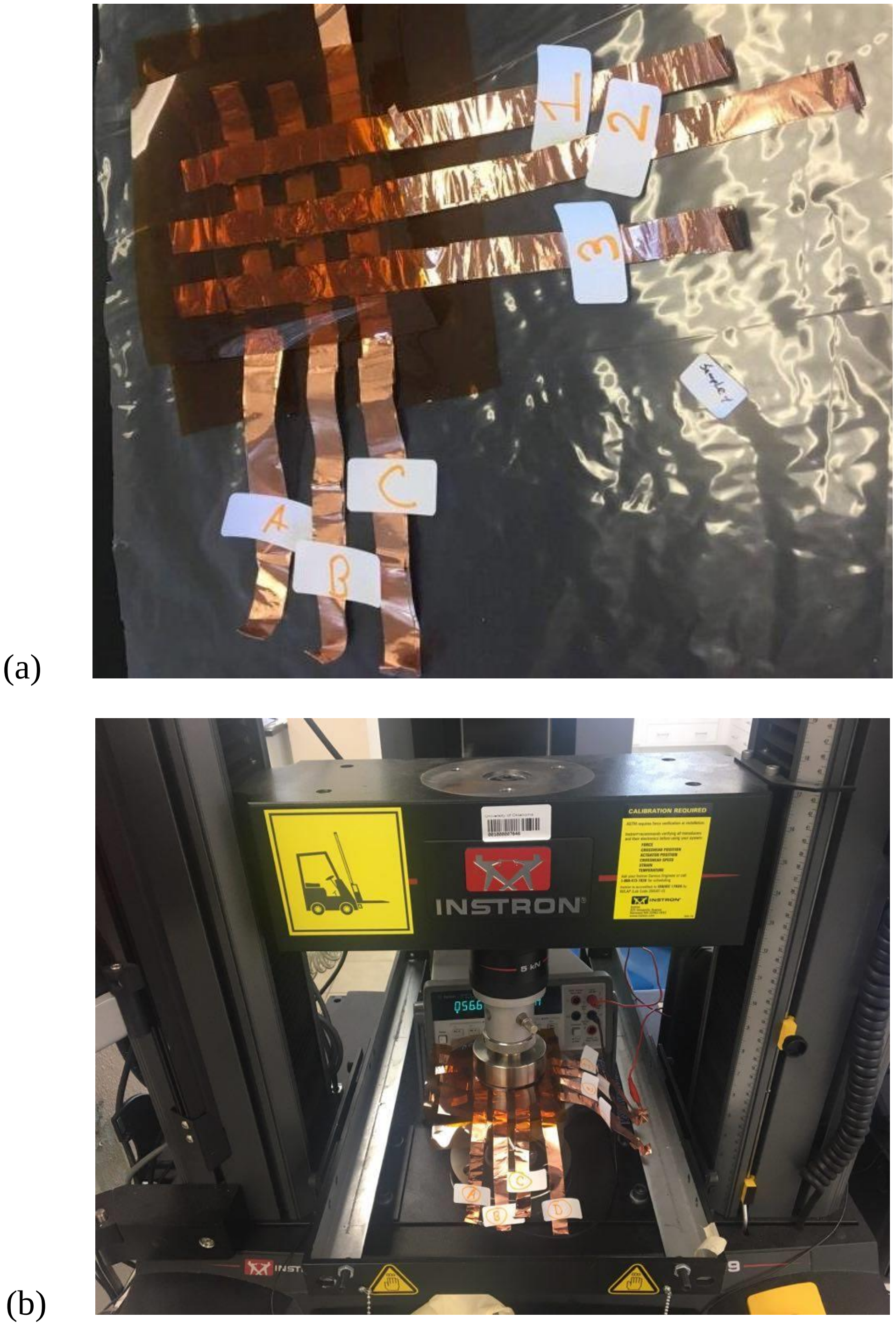

Figure 6.1: Sensor arrays produced from nanocomposites (a) 3 by 3 array from cylinder shape (b) 4 by 4 array from conical shapes.

For cylinder shape array, 25, 50, and 100 Psi distributed static pressures were applied due to the concept that the prototype of cylinder shape units array will be used for maximum 50, and 100 psi applied pressure range. This concept stemmed from the result that cylinder shape units are more sensitive in the low pressure and strain region. In the case of conical shape sensor arrays, up to maximum 150 psi static pressure was applied for the reasons discussed in previous chapters. Table 6.1 shows the results for 3 by 3 cylinder shape units sensor array and Table 6.2 for the 4 by 4cone shape units sensor array. It can be verified from Table 6.1 and 6.2 that cylinder shape array is more sensitive in the low pressure range (50 Psi) as the sensitivity in terms of percentage of resistance change does not increase much with increased applied pressure afterwards. However, the conical shape array was sensitive in the higher pressure range as the percentage change in resistance is not as high as the cylinder ones in the low pressure range. Whereas, the change rate is relatively larger as the applied pressure range is increased. This trend is similar as was evident in the case of single sensing units. Also, under distributed pressure, the sensing response is close to being uniform for each unit. The slight variations may be due to not having a perfectly flat surface and uniformly distributed pressure.

Table 6.1: Sensing response of 3 by 3 array under static distributed pressure.

Applied pressure (Psi)	Resistance change (% magnitude)	Sensing Unit								
		1A	1B	1C	2A	2B	2C	3A	3B	3C
25		35.8	73.3	93.5	89.3	83.8	91.8	64.8	77.3	89.4
50		55.4	81.3	96.7	91.6	90.7	95.7	82.6	85.6	94.1
100		66.8	84.5	97.4	92.4	93.3	96.9	87.1	87.9	95.9

Table 6.2: Sensing response of 4 by 4 array under static distributed pressure.

Applied pressure (psi)	25	50	100	150
Sensing Unit	Resistance change (% magnitude)			
1A	36.3	37.1	37.9	44.1
1B	69.1	75.7	80.2	86.5
1C	50.1	54.5	62.3	76.5
1D	39.7	49.8	59.7	65.4
2A	63.2	70.2	75.9	76.5
2B	49.4	59.1	68.1	72.3
2C	52.6	68.8	75.2	76.2
2D	50.2	61.1	66.9	68.1
3A	41.1	48.3	65.2	69.0
3B	58.2	65.8	71.8	57.1
3C	37.4	48.4	63.4	73.4
3D	59.5	67.5	73.5	77.7
4A	52.7	59.7	71.0	78.1
4B	42.9	51.0	57.0	65.6
4C	24.6	32.4	46.5	60.5
4D	59.6	64.8	68.6	71.8

Sensor array prototypes were also characterized under cyclic loading conditions to verify the reliability of sensing response that was generated under static pressure. Figure 6.2 shows the plot for sensing array element 4A for the conical sensing array under 100 psi cyclic pressure loading. It clearly shows good repeatable results in loading-unloading cycles and equivalent to static loading sensing response in terms of ~71% resistance change magnitude.

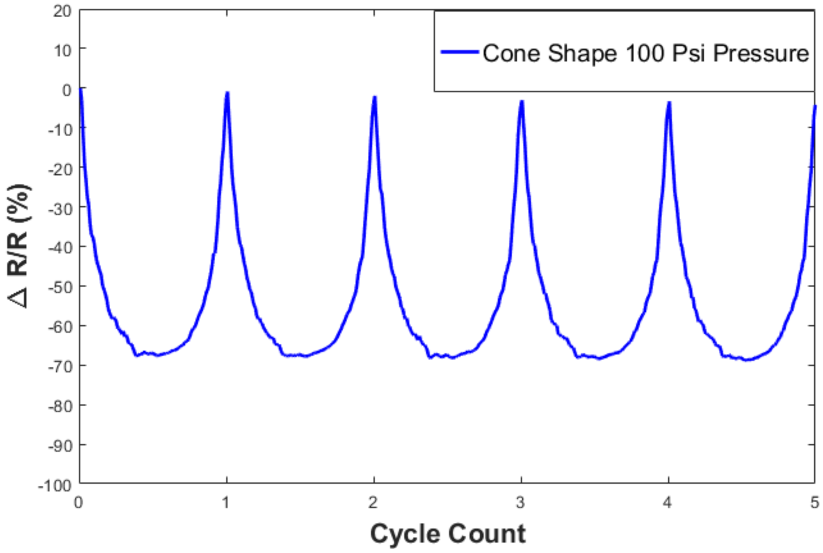

Figure 6.2: 100 Psi cyclic pressure applied to 4 by 4 sensor array showing good repeatable result for representative array element 4A.

6.1 Differential Pressure Contour

It can be a serious addition to the applicability of proposed nanocomposite based sensors if they have the ability to sense differentially applied pressures. With that motivation, different pressures were applied at different locations of both 3 by 3 and 4 by 4 sensor array prototypes and change in resistance was recorded. The concept is that at locations where higher pressures are applied, the percentage change in resistance will be larger. Thus, it will be possible to generate pressure contour plots from differential change in resistance at different locations on the sensor array. For 3 by 3 cylinder unit sensor array three different pressures as 50 psi, 25 psi, and ~5 psi were applied at different locations. In the case of cone shape unit sensor array, 100, 25, 15, and 5 psi pressures were applied. In order to verify the contour plots generated by percentage change in resistance at different locations, FEM simulations were performed by applying different static pressures on individual sensing units with similar boundary condition discussed in chapter 5. Figure 6.3 and 6.4 shows the contour plots as well FEM simulated stress plots for 3 by 3 and 4 by sensor array respectively. 2D contour plot generated from sensing results closely mimic the results obtained from FEM simulations thus verifying the viability of the concept. Where the maximum pressure is applied, the change in resistance was the highest as conceptualized and those regions are close to color red in the contour plots. On the other hand, where very low pressures were applied (less than 5 psi), those regions generated almost no change in resistance and marked by color close to blue. The similar responses are observed in the FEM simulations. The units where the highest pressures were applied (Figure 6.3: b and 6:4 b), the stress resultant were maximum signified by red color in the color spectrum. This result verifies that the sensor array is sensitive to pressure with spatial gradient and generates different response at different locations. These results can be used to detect and predict spatially differential pressures applied on the sensor area in future. It is to be noted that of course if sensor arrays are made with much larger number of units, the contour plots will have much smoother gradients.

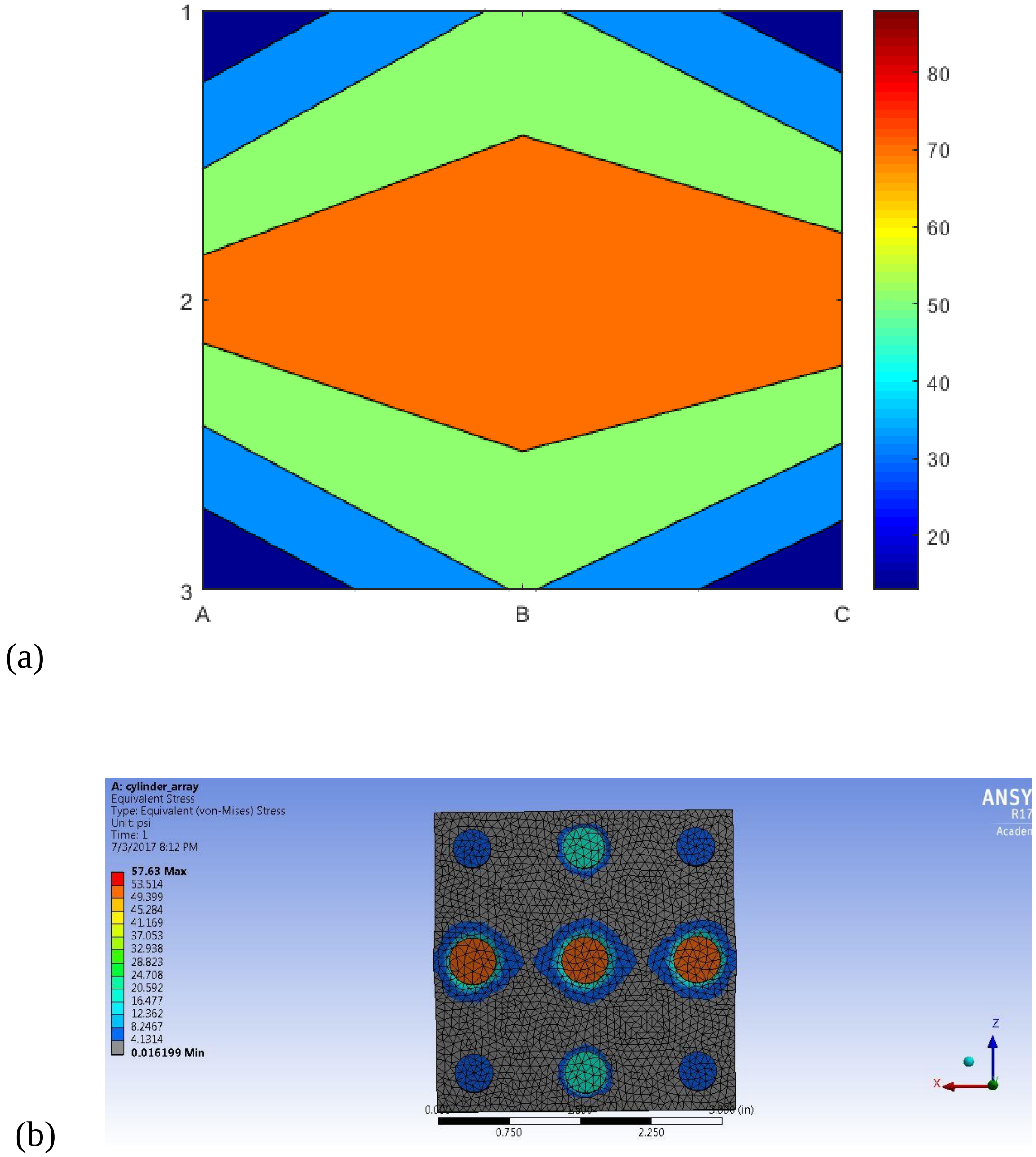

Figure 6.3: Differential pressure sensing with 3 by 3 sensor array (a) 2D contour plots generated from sensing results (b) FEM simulation.

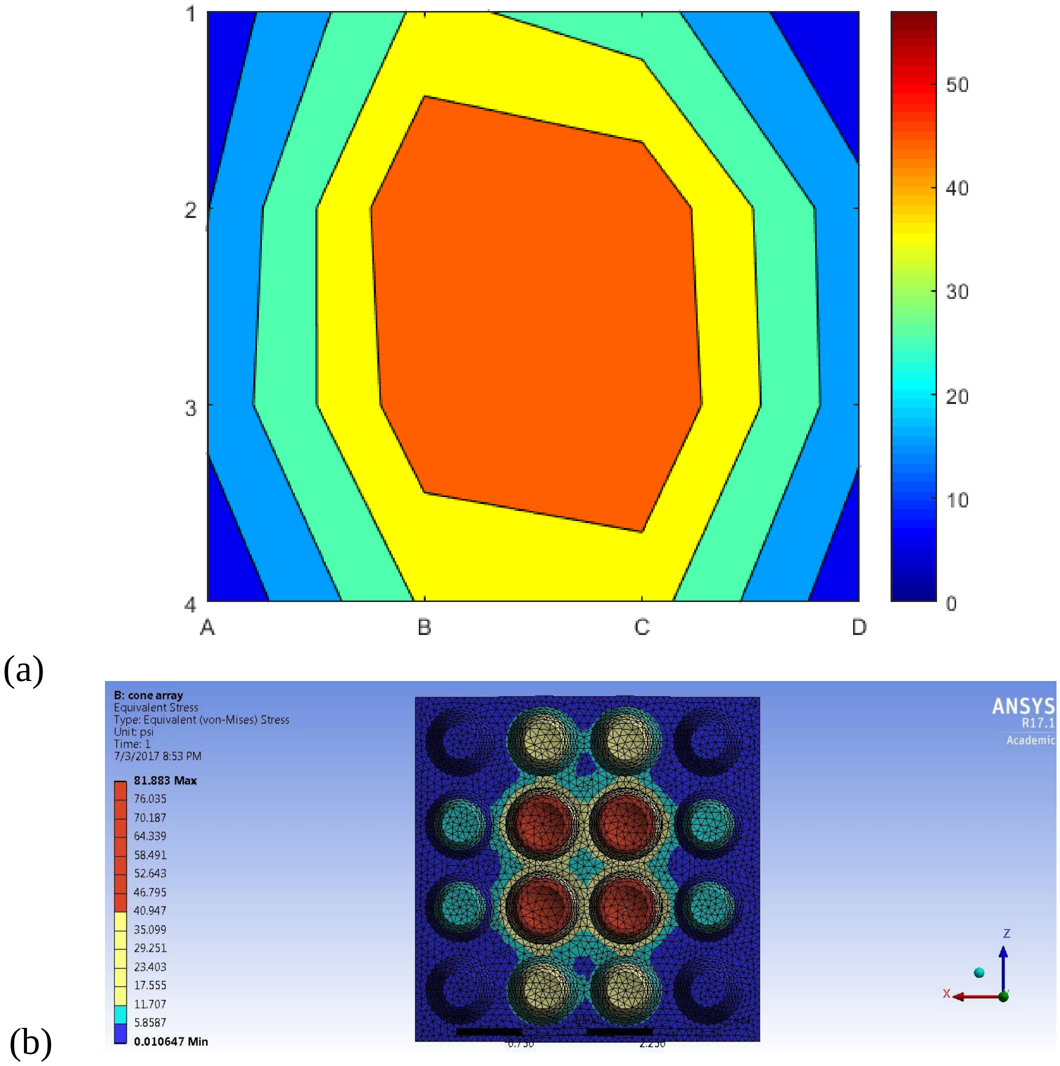

Figure 6.4: Differential pressure sensing with 4 by 4 sensor array a) 2D contour plots generated from sensing results b) FEM simulation.

As this research is application oriented, it is always the main objective to produce a sensor prototype that is commercially viable. In this chapter, the sensing units with two different shapes were connected in an array form that can be deployed to continuously monitor pressure over a large area. Both the sensor array could successfully response to static and cyclic distributed pressure on the sensor pad area. Finally, differential pressure contour plots could be generated from the sensing response of the arrays when different pressures were applied at different locations. This can be an attractive addition to the applicability of the proposed sensor.

Chapter 7 Conclusion and Scope for Future Work

This thesis presented a number of novel CNF/ PDMS nanocomposites with self-sensing functions based on piezoresistance that can be used for flexible pressure and strain sensing applications. A solvent-assisted dispersion method was used during the fabrication, providing good dispersion of CNF within PDMS polymer matrix verified by SEM micrographs at different locations and different length scales. Such uniform dispersions of CNFs resulted in good electrical conductivity of the materials. The thermal and electrical properties of the developed nanocomposites were experimentally characterized. A laser flash method was used to characterize the thermal diffusivity. The results showed that CNFs have stronger influence than silica on the thermal diffusivity properties. A TGA system was employed to characterize the thermal decomposition of each nanocomposite. Two-stage decomposition was recorded if the nanocomposites consisted of silica content. Dynamic mechanical analysis showed no glass transition temperature exists in the range of 30^0C to 150^0C. The electrical resistivity and conductivity were characterized using four-probe method to eliminate the effects of contact resistance during measurements. The percolation threshold of nanocomposites was found to be around 3 wt% CNF concentration.

Materials with electrical conductivity were tested under quasi static tensile and compressive loading conditions to determine the piezoresistive sensing function of each material and the best material formulation. Nanocomposites without any silica content failed to withstand more than 20% strain in tension due to inherent softness. 8 wt% CNF and 10:2 polymer to silica ratio material was found to be the optimum material formulation considering gauge factors both in tension and compression combined with the ability to carry load as well. The piezoresistance gauge factor for the ideal material was 3.31, 2.46, and 1.59 at 10%, 20%, and 30% maximum tensile strains respectively. Cyclic quasi-static compression tests showed good repeatable change in resistance with gauge factors 2.14, 1.46, and 1.33 in the maximum pressure range 50 psi, 100 psi, and 150 psi respectively. The concept of piezoresistance was experimentally proved by showing change in nanofiber distance and interactions with applied load under SEM.

The nanocomposite material with optimum formulation was then molded into sensing units of different shapes to improve upon the sensitivity. Initially, cylinder and cone shape was considered which showed gauge factors as high as 18.3 and 6.3 respectively at 3% maximum compressive strain. Gauge factor at higher loading with 25% maximum strain was found to be improved as well at 3.51, and 3.52 respectively. The cylinder shape units showed higher sensitivity in the low range of applied load whereas the cone shape sensing units showed the opposite trend. Sensing units also showed good robustness and durability at different rates of loading and for 1000 loading-unloading cycles.

In order to maximize the sensing functions of each shape units, optimization algorithm coupled with finite element analysis was used to find the optimum dimensions. The desired pressure range for the cylinder was 50 and 100 psi, for cone shape was 100, and 150, and for truncated pyramid was 100 psi. The sensing units with optimized dimensions were experimentally verified under cyclic compression loading conditions with gauge factor as high as 25 and 20 respectively for cylinder and cone shape at 3% maximum strain. Finally, as proof of concepts cylinder and cone shape sensing units were connected in array form to manufacture large area sensor prototype.

The produced sensor array could successfully demonstrate to sense both uniform and differential pressure applied on sensing pad area.

Although all the results were very promising and pointing towards the feasibility of such sensor, a number of improvements on current work can be suggested for future development. The CNFs obtained from manufacturer can be functionalized to improve the sensing function of bulk nanocomposite material. More experimental study under SEM can be carried out to quantify the change in resistance relation with nanofiber distance and interaction when load is applied. An integrated printed circuit board can be developed to connect the sensing units in a more robust nature so that the sensor prototype is closer to commercial level. Finally, a large number of prototypes can be produced in future to generate more statistically reliable data.

References

1. F. Yatsuyanagi, N.S., M. Ito, and H. Kaidou, *Effects of secondary structure of fillers on the mechanical properties of silica filled rubber systems.* Polymer 2001. **42**(23): p. 9523–9529.
2. Gordon, J.E., *The New Science of Strong Materials*. 2nd ed. 1976: Princeton University Press, Princeton, NJ
3. Sundararaj, M.H.A.-S.a.U., *A review of vapor grown carbon nanofiber/polymer conductive composites.* Carbon, 2009. **47**(1): p. 2-22.
4. J.N. Coleman, U.K., W.J. Blau, and Y.K. Gun'ko, *Small but strong: A review of the mechanical properties of carbon nanotube.* polymer composites, 2006. **44**(9): p. 1624-1652.
5. T. Kuilla, S.B., D. Yao, N.H. Kim, S. Bose, and J.H. Lee, *Recent advances in graphene based polymer composites.* Prog. Polym. Sc.I 2010. **35**(11): p. 1350-1375.
6. Huang, Z.-M., et al., *A review on polymer nanofibers by electrospinning and their applications in nanocomposites.* Composites science and technology, 2003. **63**(15): p. 2223-2253.
7. Rodriguez, N.M., *A review of catalytically grown carbon nanofibers.* Journal of Materials Research, 1993. **8**(12): p. 3233-3250.
8. R.J. Kuriger, M.K.A., D.P. Anderson, and R.L. Jacobsen, *Processing and characterization of aligned vapor grown carbon fiber reinforced polypropylene.* Compos. Part A Appl. Sci. Manuf. , 2002. **33**(1): p. 53-62.
9. H. Gojny, M.H.G.W., B. Fiedler, I.A. Kinloch, W. Bauhofer, A.H. Windle, and K. Schulte, *Evaluation and identification of electrical and thermal conduction mechanisms in carbon nanotube/epoxy composites.* Polymer, 2006. **47**(6): p. 2036-2045.
10. Bhowmick, N.R.a.A.K., *Novel in situ carbon nanofiber / polydimethyl siloxane nanocomposites: Synthesis, morphology, and physico-mechanical properties.* J. Appl. Polym. Sci. , 2012. **123**(6): p. 3675–3687.
11. A. Paleo, X.G., L. Arboleda-Clemente, F. Van Hattum, M. Abad, and A. Ares, *Enhanced thermal conductivity of rheologically percolated carbon nanofiber reinforced polypropylene composites.* Polym. Adv. Technol. , 2015. **26**(4): p. 369–375.
12. S. Gordeyev, F.M., J. Ferreira, F. Van Hattum, and C. Bernardo, *Transport properties of polymer-vapour grown carbon fibre composites.* Physica B: Condensed Matter 2000. **279**(1-3): p. 33-36.
13. Tibbetts, I.C.F.a.G.G., *Electrical conductivity of vapor-grown carbon fiber/thermoplastic composites.* J. Mater. Res. , 2001. **16**(06): p. 1668–1674.
14. J. Xu, J.P.D., and C.U. Pittman, *Pittman, Preparation, electrical and mechanical properties of vapor grown carbon fiber (VGCF)/vinyl ester composites.* Compos. Part A Appl. Sci. Manuf., 2004. **35**(6): p. 693–701.
15. Bhowmick, N.R.a.A.K., *In situ preparation, morphology and electrical properties of carbon nanofiber/polydimethylsiloxane nanocomposites.* J. Mater. Sci., 2012. **47**(1): p. 272–281.

16. Sandler, J., et al., *Carbon-nanofibre-reinforced poly (ether ether ketone) composites.* Composites Part A: Applied Science and Manufacturing, 2002. **33**(8): p. 1033-1039.
17. Shui, X.a.D.C., *Conducting polymer-matrix composites containing carbon filaments of submicron diameter.* Advanced Materials: Performance Through Technology Insertion, 1993. **38**: p. 1869-1875.
18. Murphy, E.B., Wudl, F. *The world of smart healable materials*. in *Progress in Polymer Science*. 2010.
19. Liu, Y., Lv, H., Lan, X., Leng, J., Du, S., *Review of electro-active shape-memory polymer composite.* Composite Science and Technology, 2009. **69**: p. 2064-2068.
20. Montalvao, D., Maia, N.M.M., and Ribeiro, A.M.R., *A review of vibration-based structural health monitoring with special emphasis on composite materials.* The Shock and Vibration Digest, 2006. **38**(4): p. 295–324
21. Liu, Y., Mohanty, S., Chattopadhyay, A., *Condition based structural health monitoring and prognosis of composite structures under uniaxial and biaxial loading.* Journal of Nondestructive Evaluation, 2010. **29**(3): p. 181-188.
22. Lucarotti, C., et al., *Synthetic and bio-artificial tactile sensing.* A review. Sensors, 2013. **13**(2): p. 1435-1466.
23. Chortos, A.a.Z.B., *Skin-inspired electronic devices.* Materials Today, 2014. **17**(7): p. 321-331.
24. Pang, Y., et al., *Flexible, Highly Sensitive, and Wearable Pressure and Strain Sensors with Graphene Porous Network Structure.* ACS Applied Materials & Interfaces, 2016. **8**(40): p. 26458-26462.
25. Cheng, M.-Y., et al., *The development of a highly twistable tactile sensing array with stretchable helical electrodes.* Sensors and Actuators A: Physical, 2011. **166**(2): p. 226-233.
26. Woo, S.-J., et al., *A thin all-elastomeric capacitive pressure sensor array based on micro-contact printed elastic conductors.* Journal of Materials Chemistry C, 2014. **2**(22): p. 4415-4422.
27. Lipomi, D.J., et al., *Skin-like pressure and strain sensors based on transparent elastic films of carbon nanotubes.* Nature nanotechnology, 2011. **6**(12): p. 788-792.
28. Persano, L., et al., *High performance piezoelectric devices based on aligned arrays of nanofibers of poly (vinylidenefluoride-co-trifluoroethylene).* Nature communications, 2013. **4**: p. 1633.
29. Jiao, J.e.a., *Antibacterial and anticancer PDMS surface for mammalian cell growth using the Chinese herb extract paeonol(4-methoxy-2-hydroxyacetophenone).* Scientific Reports, 2016. **6**: p. 38973.
30. http://pyrografproducts.com/nanofiber.html#_PR-24-XT-LHT_Data_Sheet.
31. Park, J., et al., *Giant tunneling piezoresistance of composite elastomers with interlocked microdome arrays for ultrasensitive and multimodal electronic skins.* ACS nano, 2014. **8**(5): p. 4689-4697.
32. Park, J., et al., *Tactile-direction-sensitive and stretchable electronic skins based on human-skin-inspired interlocked microstructures.* ACS nano, 2014. **8**(12): p. 12020-12029.

33. M. Kinoshita, T.N., T. Souda, and K. Takeda, *Semi-quantitative analysis of thermal degradation in polyphenylene-ether.* Polym. Degrad. Stab., 2000. **68**(3): p. 2000.
34. G. Camino, S.L., and M. Lageard, *Thermal polydimethylsiloxane degradation. Part 2. The degradation mechanisms.* Polymer, 2002. **43**(7): p. 2011–2015.
35. T. Merkel, B.F., R. Spontak, Z. He, I. Pinnau, P. Meakin, and A. Hill, *Ultrapermeable,reverse-selective nanocomposite membranes.* Science 2002. **296** (5567): p. 519-522.
36. B. Hay, J.F., J. Hameury, and L. Rongione, *Uncertainty of thermal diffusivity measurements by laser flash method.* Int. J. Thermophys. , 2005. **26**(6): p. 1883–1898.
37. Menard, H.P., *Dynamic Mechanical Analysis: A Practical Introduction*. 2nd ed.: CRC press.
38. Sheth J, A.A., Wilkes G. L, Yilgor E, Atilla E, Yilgor I and Beyer F *Influence of system variables on the morphological and dynamic mechanical behavior of polydimethylsiloxane based segmented polyurethane and polyurea copolymers: a comparative perspective* polymer, 2004. **45**: p. 6919–6932.
39. Yasmin, A.e.a., *Mechanical and thermal behavior of clay/epoxy nanocomposites.* Composites Science and Technology 2006. **66**: p. 2415 2422.
40. Young Seok Song, J.R.Y., *Influence of dispersion states of carbon nanotubes on physical properties of epoxy nanocomposites.* Carbon, 2005. **43**: p. 1378–1385.
41. Geng, Y.e.a., *Effects of surfactant treatment on mechanical and electrical properties of CNT/epoxy nanocomposites.* Composites: Part A 2008. **39**: p. 1876–1883
42. Genetti, W.B.e.a., *Polymer matrix composites: Conductivity enhancement through polypyrrole coating of nickel flak.* JOURNAL OF MATERIALS SCIENCE, 1998. **33**: p. 3085- 3093.
43. Hu, L.e.a., *Percolation in Transparent and Conducting Carbon Nanotube Networks* Nano Lett, 2004. **4**: p. 2513-2517.
44. Sandler, J.K.W.e.a., *Ultra-low electrical percolation threshold in carbon-nanotube-epoxy composites.* Polymer, 2003. **44**: p. 5893–5899.
45. Rinaldi, A.e.a., *A Flexible and Highly Sensitive Pressure Sensor Based on a PDMS Foam Coated with Graphene Nanoplatelets* Sensors 2016. **16**: p. 2148.
46. Chen, L., G. Chen, and L. Lu, *Piezoresistive Behavior Study on Finger‐Sensing Silicone Rubber/Graphite Nanosheet Nanocomposites.* Advanced Functional Materials, 2007. **17**(6): p. 898-904.
47. Mannsfeld, S.C., et al., *Highly sensitive flexible pressure sensors with microstructured rubber dielectric layers.* Nature materials, 2010. **9**(10): p. 859-864.
48. Khan, S., et al., *Flexible tactile sensors using screen-printed P (VDF-TrFE) and MWCNT/PDMS composites.* IEEE sensors Journal, 2015. **15**(6): p. 3146-3155.
49. Fan, F.-R., et al., *Transparent triboelectric nanogenerators and self-powered pressure sensors based on micropatterned plastic films.* Nano letters, 2012. **12**(6): p. 3109-3114.
50. Cookson, J.W., *Theory of the piezo-resistive effect.* Phys Rev. , 1935. **47**(194–195).

51. Barlian, A.A.e.a. *Review: Semiconductor piezoresistance for microsystems*. in *Proc IEEE Inst Electr Electron Eng.* . 2009.
52. Lucarotti, C.e.a., *Synthetic and bio-artificial tactile sensing: A review.* Sensors, 2013. **13**(2): p. 1435-1466.
53. Dobie, W.B.I.P., C. G. , *Electric Resistance Strain Gauges* 1948: English Universities Press Limited.
54. Zhang, X.e.a., *Time Dependence of Piezoresistance for the Conductor-Filled Polymer Composites.* Journal of Polymer Science: Part B: Polymer Physics, 2000. **38**: p. 2739 –2749
55. Knite, M.T., V. Kiploka, A. Kaupuzs, J. , *Polyisoprene-carbon black nanocomposites as tensile strain and pressure sensor materials* Sensors and Actuators A 2004. **110**: p. 142-149.
56. Toprakci, H.A., et al., *Polymer Nanocomposites Containing Carbon Nanofibers as Soft Printable Sensors Exhibiting Strain-Reversible Piezoresistivity.* Advanced Functional Materials, 2013. **23**(44): p. 5536-5542.
57. Hou, Y.e.a., *Positive piezoresistive behavior of electrically conductive alkyl-functionalized graphene/ polydimethylsilicone nanocomposites* J. Mater. Chem. C, 2013. **1**: p. 515–521.
58. Paleo, A.J.H.F.W.J.R., J.G. Lanceros-Mendez, S. , *Piezoresistive polypropylene–carbon nanofiber composites as mechanical transducers* Microsyst Technol 2012. **18**: p. 591-597.
59. Zhu, B., et al., *Microstructured graphene arrays for highly sensitive flexible tactile sensors.* Small, 2014. **10**(18): p. 3625-3631.
60. Choong, C.e.a., *Highly Stretchable Resistive Pressure Sensors Using a Conductive Elastomeric Composite on a Micropyramid Array* Adv. Mater., 2014. **26**: p. 3451–3458.
61. Kim, T.K., Kim, J. K., & Jeong, O. C. , *Measurement of nonlinear mechanical properties of PDMS elastomer.* Microelectronic Engineering, 2011. **88**(8): p. 1982-1985.
62. Cho, I.H., Zoh,K.D. , *Photocatalytic degradation of azo dye (Reactive Red 120) in TiO2/UV system: Optimization and modeling using a response surface methodology (RSM) based on the central composite design*. Dyes and Pigments 2007. **75**(533-543).
63. Rosa, P.A., Azevedo, A.M, Barros,M.R., *Application of central composite design to the optimisation of aqueous two-phase extraction of human antibodies.* Journal of Chromatography A, 2007. **1141**: p. 50-60.
64. Khataee, A.R., Fathinia, M. Aber,S. Zarei, M., *Optimization of photocatalytic treatment of dye solution on supported TiO2 nanoparticles by central composite design: Intermediates identification.* Journal of Hazardous Materials 2010. **181**: p. 886-897.
65. Wang, K.Z., C. Li,W. , *Comparison of Geographically Weighted Regression and Regression Kriging for Estimating the Spatial Distribution of Soil Organic Matter.* GIScience & Remote Sensing, 2012. **49**(6): p. 915-932.
66. Szweda, J.P., Z. , *Thermal Properties Improving Of The Electromotor Frame.* Journal of Solid Mechanics and Materials Engineering 2010. **4**(6).
67. Perng, Y.W., J. , *Optimization is ANSYS Workbench*.

68. Pan, L., et al., *An ultra-sensitive resistive pressure sensor based on hollow-sphere microstructure induced elasticity in conducting polymer film.* Nature communications, 2014. **5**: p. 3002.